_____
Unterschrift Betreuer

TU WIEN

TECHNISCHE
UNIVERSITÄT
WIEN
Vienna University of Technology

DIPLOMARBEIT

Ab-initio calculations for Thorium doped Calcium Fluoride (CaF$_2$)

ausgeführt am Institut für Angewandte Physik
der Technischen Universität Wien

unter der Anleitung von
Univ.Prof. Dipl.-Ing. Dr.techn. Peter Mohn

durch

Philipp Dessovic, Bsc.

Porzellangasse 52/14
1090 Wien, Österreich

30th May 2016

_____
Unterschrift Student

Abstract

The Thorium isotope 229Th exhibits the lowest groundstate doublet of all known nuclei (7,8(5) eV resp. 159nm). It was thus suggested to employ this excitation as an 'atomic clock'. Experimentally one uses a CaF_2 single crystal which becomes doped with Th. It is assumed that Th occupies a Ca site, however, due to the different valence (Th is 4+ and Ca is 2+) there must be 2 additional compensation charges present to maintain the insulating state. In the present Masters thesis ab-initio calculations were performed to simulate the experimental assumptions and to verify them. It was studied which lattice site are really occupied by Th and which type of compensation actually occurs. It was shown that the energetically most reasonable compensation is provided if 2 additional F ions are present, moreover also the crystallographic positions of these compensation charges were determined. Further studies concerned the simulation of various impurities which can occur during the crystal growth. It was shown that oxygen impurities lead to additional electronic states in the insulating gap, which would hinder optical exitations of the Th nucleus.

Results were published in '229 Thorium-doped calcium fluoride for nuclear laser spectroscopy' [20].

Kurzfassung

Das Thorium Isotop 229Th zeigt mit 7,8(5) eV entspr. 159nm das niedrigste Grundzustands- dublett aller bekannten Kerne. Es wurde daher vorgeschlagen diese Anregung als 'atomic clock' zu verwenden. Experimentell verwendet man einen CaF2 Einkristall, der mit Th dotiert wird. Dabei geht man davon aus, dass Th die Ca Positionen besetzt und dass, aufgrund der der Valenz 4+ (Ca hat 2+) noch zwei zusätzliche Kompensationsladungen vorhanden sein müssen um den isolierenden Zustand zu erhalten. Die Aufgabe der Diplomarbeit war es nun diese experimentelle Situation in einer ab-initio Rechnung zu überprüfen. Dabei wurde untersucht welche Gitterplätze Th tatsächlich einnimmt, wo die Kompensationsladungen sitzen und welche Art von Kompensation in Frage kommt. Es konnte gezeigt werden, dass die energetisch günstigste Variante der Einbau von 2 zusätzlichen Fluor Atomen ist, dabei wurden auch die energetisch günstigsten Gitterplätze für die F Atome bestimmt. Weitere Untersuchungen befassten sich mit der Simulation von diversen Verunreinigungen, die im Produktionsprozess auftreten können. Dabei konnte gezeigt werden, dass Verunreinigungen mit Sauerstoff zu zusätzlichen elektronischen Zuständen in der Mitte des isolierenden gaps führen, die eine optische Anregung des gewünschten Th Überganges verhindern würden.

Die Ergebnisse wurde publiziert in '229 Thorium-doped calcium fluoride for nuclear laser spectroscopy' [20].

Acknowledgements

Contents

1. Introduction

1.1. Motivation Atomic Clock

The goal of the project is building a more precise and complete new kind of atomic clock. There are many applications for an accurate atomic clock today. For example all satellite navigation systems (like GPS, GLONASS, GALLILEO) need atomic clocks in its satellites to localize a gps-receivers[98]. With more accurate atomic clocks, the precision could be increased further. Another possible application would be to check if any drifts of fundamental constants, like the fine structure constant can be measured [97, 22, 76]. Todays frequency standards have an relative uncertainty below 1×10^{-15}. The most accurate clocks today are accurate to -17$^{\text{th}}$. Building better clocks becomes increasingly difficult since external fields and motion shifts are a limiting factor beside the line width of the transitions[14]. Since all atomic clocks till today use ionic atoms held in place by some electro magnetic fields in an ionic trap or their flight in an electro magnetic path is analysed. Peik and Tamm suggested in 2003 that the ^{229}Th isotope could be used for building an nuclear atomic clock, since has the lowest known ground state doublet ($\approx 7.8(5)\,\text{eV}/159\,\text{nm}$ [7]) of all isotopes. The advantage in using the optical transitions of the atomic nucleus instead of similar transitions of the electronic shell is that the nucleus is shielded by the electrons from external fields.

There have been two kind of approaches suggested. The first was using an ionic trap to hold the Thorium isotope as was suggested by Campbell et al. from the Georgia Institute of Technology who estimate the precision of a Th^{3+} clock [13, 14]. They propose to cool the ^{229}Th^{3+} via sympathetic cooling with ^{232}Th in a linear rf trap.

The other approach is to dope a clear crystal with Thorium. There have been several possible host crystals which are transparent in the vacuum-ultra-violet (VUV) regime studied [26, 77]. The LiCaF crystal (LiCaAlF$_6$) hast been identified as a promising canditate by [77, 37]. The other extensively studied crystal is CaF$_2$[39, 40], which is evaluated by the group of Prof. Thorsten Schumm, Vienna University of Technology. He suggested this thesis to improve the understanding of the crystalline electronic properties of a thorium doped CaF$_2$ crystal. This thesis should determine the crystal structure of the doped crystal and whether it remains transparent in the VUV range.

1.2. Bandgap problem

A crystal is transparent if the bandgap is larger than the photon energy. The question is if the bandgap of Thorium doped CaF_2 remains larger than the $\approx$ 7.8(5) eV ($\approx$ 159 nm) necessary to excite the ^{229}Th.

There are several different definitions what a band-gap is in solid state. The quasi-particle gap (also called: fundamental or physical gap) is the difference between the ionization energy I and the electron affinity A. The ionization energy I is defined as $E_N - E_{N-1}$ and the electron affinity A as $E_N - E_{N+1}$. These energies can be measured experimentally. The optical gap is the energy necessary for excitation of electrons resulting in optical absorption. The most common definition is the difference between the highest occupied molecular orbit (HOMO) and the lowest unoccupied molecular orbit (LUMO). This is called the HOMO-LUMO gap (also: orbital-energy, single-particle or one-electron gap). Although in crystals the correct name would be HOCO (highest occupied crystal orbital) and LUCO (lowest unoccupied crystal orbital), the term HOMO-LUMO gap is more common. These gaps are not identical. Usually the HOMO-LUMO gap is below the quasi-particle gap and the quasi-particle gap is larger than the optical gap by the exciton shift.[19] 'Experimentally, the difference between optical and fundamental gap is very small in semiconductors but significant in insulators.'[11]

In DFT calculations the HOMO-LUMO gap of the non-interacting particles is an approximation of the HOMO-LUMO gap of the interacting electrons.

There are direct and indirect band gaps. The direct band gap is the (smallest) difference between conduction and valence band at the same point in k-space, while the indirect is just the difference between the highest energy of the conduction and the lowest energy of the valence band, not necessarily at the same k-vector. The reported band gap of pure calcium fluorite is about 12 eV (direct 12.1 eV/indirect 11.8 eV[80], 11.8 eV @268 K & 12.0 eV @15 K [96]).

2

2. Method

2.1. Density functional theory (DFT)

The electronic properties of doped CaF_2 were calculated by applying density functional theory (DFT). The implementation of the projector augmented-wave method (PAW) in the Vienna Ab initio Simulation Package (VASP) was used. Several papers on this topic can be recommended to the reader. A very short introduction of the basic ideas of density functional theory, using an analogue from statistical mechanics, is the paper 'Density functional theory: An introduction' [1]. Although it is only 11 pages long it gives an rough introduction on undergraduate level. A longer paper (44 pages) on DFT and different implementations is 'Theory and Practice of Density-Functional Theory' [10] by Blöchl. In this chapter the most important points of this paper are summarized. A more in-depth discussion of density functional theory can be found in the book *The ABC of DFT* [12] (200 pages).

2.1.1. DFT-Theory

Density functional theory is based on a paper by Hohenberg and Kohn[32]. It proves that a functional $H[n] = E_{kin}[n] + E_{pot}[n]$ exists, which only depends on the density $n(\vec{r})$ and is minimized by the groundstate density of the system. Kohn and Sham showed that a fictitious system of non interacting electrons with the same density can be used to solve the many body problem [43].

This sections closely follows the paper and notation [10] by P. E. Blöchl and summarizes the most important ideas of the density functional theory.

For N particles the Schrödinger equation in 3N dimension needs to be solved. Even for a small number of atoms, with a couple of electrons each, the wave function would be a gigantic amount of data. The most important force in any solid is the electrostatic interaction between all electrons and nuclei, which is not negligible. Nevertheless this problem of one wave function in 3N dimensions can be mapped on N non-interacting wave functions in 3 dimension with the help of density functional theory. While the exact mapping is too complicated for usage, some simple and accurate approximations exists.

The electronic structure can be described using the N-particle Hamiltonian $\hat{H}$

in the Schrödinger equation applied to the all N-electron wave function $|\Psi\rangle$.

$$\hat{H} = \sum_{j=1}^{N} \left(\frac{-\hbar^2}{2m_e} \vec{\nabla}_j^2 + v_{ext}(\vec{r}_j) \right) + \frac{1}{2} \sum_{i \neq j}^{N} \frac{e^2}{4\pi\epsilon_0 |\vec{r}_i - \vec{r}_j|} \tag{2.1}$$

The discrete spin σ can be included in the calculation and is combined with the continuous space coordinate $\vec{r}$ to $\vec{x} := (\vec{r}, \sigma)$. In this notation the 4 dimensional integral $\int d^4x$ denotes $\sum_\sigma \int d^3r$. The ground state energy is defined by $E = \langle\Psi|\hat{H}|\Psi\rangle$.

$$E = \int d^4x_1 \cdots \int d^4x_N \ \Psi^*(\vec{x}_1, \ldots, \vec{x}_N) \hat{H} \Psi(\vec{x}_1, \ldots, \vec{x}_N) \tag{2.2}$$

This equation consist of only two types of integrals and can be expressed as

$$E = \int d^4x' \int d^4x \ \delta(\vec{x'} - \vec{x}) \left(\frac{-\hbar^2}{2m_e} \vec{\nabla}^2 + v_{ext}(\vec{r}) \right) \rho^{(1)}(\vec{x}, \vec{x'})$$
$$+ \frac{1}{2} \int d^3r \int d^3r' \ \frac{e^2 n^{(2)}(\vec{r}, \vec{r'})}{4\pi\epsilon_0 |\vec{r} - \vec{r'}|} \tag{2.3}$$

using $\rho^{(1)}(\vec{x}, \vec{x'})$ and $n^{(2)}(\vec{r}, \vec{r'})$.

The one-particle reduced density matrix $\rho^{(1)}\left(\vec{x}, \vec{x'}\right)$ depends on two arguments of the same particle. It can be used to calculate one particle operators (e.g. $E_{\text{kin}}, V_{\text{ext}}$).

$$\rho^{(1)}(\vec{x}, \vec{x'}) := N \int d^4x_2 \ldots \int d^4x_N \ \Psi(\vec{x}, \vec{x}_2, \ldots, \vec{x}_N) \Psi^*(\vec{x'}, \vec{x}_2, \ldots, \vec{x}_N) \tag{2.4}$$

The orthogonal eigenstates $\varphi_n(\vec{r})$ of $\rho^{(1)}$ are called natural orbitals and their eigenvalues $\bar{f}_n$ are their occupations.

$$\rho^{(1)}(\vec{x}, \vec{x'}) = \sum_n \bar{f}_n \varphi_n(\vec{x}) \varphi_n^*(\vec{x'}) \tag{2.5}$$

The two particle density $n^{(2)}\left(\vec{r}, \vec{r'}\right)$ depends on the positions of two different electrons. It is a measure of the interaction between two electrons.

$$n^{(2)}(\vec{r}, \vec{r'}) := N(N-1) \sum_{\sigma, \sigma'} \int d^4x_3 \ldots \int d^4x_N \ |\Psi(\vec{x}, \vec{x'}, \vec{x}_3, \ldots, \vec{x}_N)|^2 \tag{2.6}$$

For non interacting electrons $n^{(2)}$ can be approximated by

$$n^{(2)}(\vec{r}, \vec{r'}) = n^{(1)}(\vec{r}) \left[n^{(1)}(\vec{r'}) + h(\vec{r}, \vec{r'}) \right]. \tag{2.7}$$

$$h(\vec{r}, \vec{r'}) \ \ldots \ \text{hole function}$$

In this approximation the coulomb interaction can be separated into the Hartree energy

$$E_H := \frac{1}{2} \int d^3r \int d^3r' \, \frac{e^2 n^{(1)}(\vec{r}) n^{(1)}(\vec{r'})}{4\pi\epsilon_0 |\vec{r} - \vec{r'}|} \tag{2.8}$$

and the potential energy of exchange and correlation

$$U_{xc} := \int d^3r \, n^{(1)}(\vec{r}) \frac{1}{2} \int d^3r' \, \frac{e^2 \, h(\vec{r}, \vec{r'})}{4\pi\epsilon_0 |\vec{r} - \vec{r'}|} \; . \tag{2.9}$$

Using the exact densities, respectively the natural orbitals $\varphi_n(\vec{r})$ of $\rho^{(1)}$, the expression for the energy 2.3 can be simplified to

$$E = \sum_n \bar{f}_n \int d^4x \, \varphi_n^*(\vec{x}) \frac{-\hbar^2}{2m} \vec{\nabla}^2 \varphi_n(\vec{x}) + \int d^3r \, v_{ext}(\vec{r}) n^{(1)}(\vec{r})$$
$$+ \frac{1}{2} \int d^3r \int d^3r' \, \frac{e^2 n^{(2)}(\vec{r}, \vec{r'})}{4\pi\epsilon_0 |\vec{r} - \vec{r'}|} \; . \tag{2.10}$$

Nevertheless the reduced density matrix ($\rho^{(1)}$) is still needed to compute the natural orbitals ($\varphi_n(\vec{r})$).

The kinetic energy can be approximated by the kinetic energy functional $T_s[n^{(1)}]$ of non-interacting electrons with the same density as the real interacting system.

$$T_s[n^{(1)}] = \min_{\{f_n \in [0,1], |\psi_n\rangle\}} \left\{ \sum_n f_n \int d^4x \, \psi_n^*(\vec{x}) \frac{-\hbar^2 \vec{\nabla}^2}{2m} \psi_n(\vec{x}) \right.$$
$$+ \int d^3r \, v_{eff}(\vec{r}) \left(\left[\sum_n f_n \sum_\sigma \psi_n^*(\vec{x}) \psi_n(\vec{x}) \right] - n^{(1)}(\vec{r}) \right)$$
$$\left. - \sum_{n,m} \Lambda_{m,n} \left(\langle \psi_n | \psi_m \rangle - \delta_{n,m} \right) \right\} \tag{2.11}$$

$\psi_n(\vec{x})$ ... Kohn-Sham orbital (natural orbital of non interacting electrons)

The interaction increases both the potential and the kinetic energy. The total exchange and correlation energy (E_{xc})is the potential exchange and correlation energy (U_{xc})plus the difference between the interacting kinetic Energy (E_{kin}) and non interacting kinetic Energy (T_s).

$$E_{xc} = U_{xc} + \sum_n \bar{f}_n \int d^4x \, \varphi_n^*(\vec{x}) \frac{-\hbar^2}{2m} \vec{\nabla}^2 \varphi_n(\vec{x}) - T_s[n^{(1)}] \; . \tag{2.12}$$

Note that E_{xc} uses natural orbitals ($\varphi_n(\vec{x})$) and their occupation ($\bar{f}_n$) of interacting electrons, while T_s is defined in terms of non-interacting electrons ($\psi_n(\vec{x}), f_n$).

The total energy is defined:

$$E = \min_{|\Phi\rangle,\{|\psi_n\rangle,f_n\in[0,1]\}} \left\{ \sum_n f_n \int d^4x\ \psi_n^*(\vec{x}) \frac{-\hbar^2}{2m} \vec{\nabla}^2 \psi_n(\vec{x}) \right. \tag{2.13}$$

$$+ \int d^3r\ v_{eff}(\vec{r}) \left(\left[\sum_n f_n \sum_\sigma \psi_n^*(\vec{x}) \psi_n(\vec{x}) \right] - n(\vec{r}) \right) + \int d^3r\ v_{ext}(\vec{r}) n^{(1)}(\vec{r})$$

$$\left. + \frac{1}{2} \int d^3r \int d^3r'\ \frac{e^2 n^{(1)}(\vec{r}) n^{(1)}(\vec{r'})}{4\pi\epsilon_0 |\vec{r}-\vec{r'}|} + E_{xc} - \sum_{n,m} \Lambda_{m,n} \left(\langle \psi_n | \psi_m \rangle - \delta_{n,m} \right) \right\}$$

It can be shown that E_{xc} can be defined only depending on the one particle density ($n^{(1)}(\vec{r})$) [10, ,p.10]

The total energy can be minimized with the respect to the Kohn-Sham wave functions ($\psi_n(\vec{x})$), their occupations (f_n) and the one particle density ($n^{(1)}(\vec{r})$), resulting in the following equations:

$$\left[\frac{-\hbar^2}{2m_e} \vec{\nabla}^2 + v_{eff}(\vec{r}) - \epsilon_n \right] \psi_n(\vec{x}) = 0 \qquad \text{with} \qquad \int d^4x\ \psi_m(\vec{x}) \psi_n(\vec{x}) = \delta_{m,n}$$

$$\epsilon_n := \Lambda'_{n,n} \qquad \ldots \qquad \Lambda' \text{ is } \Lambda \text{ diagonalized}$$

$$v_{eff}(\vec{r}) = v_{ext}(\vec{r}) + \int d^3r'\ \frac{e^2 n^{(1)}(\vec{r'})}{4\pi\epsilon_0 |\vec{r}-\vec{r'}|} + \frac{\delta E_{xc}[n^{(1)}]}{\delta n^{(1)}(\vec{r})} \tag{2.14}$$

$$\text{using} \qquad n^{(1)}(\vec{r}) = \sum_n f_n \sum_\sigma \psi_n^*(\vec{x}) \psi_n(\vec{x})$$

The first equation resembles a Schrödinger equation of non-interacting electrons and is called Kohn-Sham equation[43]. The equations (2.14) are a set of coupled equations, which can be solved in a self consistency cycle. With the resulting electron density the total energy can be computed.

While the Kohn-Sham orbitals ($\psi_n(\vec{x})$) and their occupations used to calculate the energy resemble the ground state density in principle exactly, they are not identical with the real many-body wave function of interacting electrons. Only the ground state properties that can be extracted from the density are known to be exact.

There is little theoretical backing that other non-ground state properties, like the band gap, calculated with Kohn-Sham orbitals are correct. Since the band gap is effectively the difference between two eigenvalues it is in principle because strictly speaking the individuell eigenvalues have no physical relevance. While the sum over the occupied eigenvalues yields the right contribution to the ground state energy, the individuel eigenvalue has no physical meaning. However it is

found that the occupied eigenvalues yield a reasonable describtion of the electronic structure, which of course depends on the applied approximation of Exchange and Correlation. Concerning the band gap it is known that standard LDA grossly underestimates the gap, a problem that is improved by the application of hybrid functionals.

2.1.2. Density functionals

The density functional theory (DFT), that was presented in the last subsection 2.1.1, is theoretically exact, but the exchange and correlation Energy functional ($E_{xc}[n^{(1)}]$) is unknown. The $E_{xc}[n^{(1)}]$ functional has been approximated using several techniques and the parameters of the functionals have been fitted to sets of benchmark systems or computed using theoretical models and simulations.

LDA

In the local density approximation (LDA) the functional only depends on the local value of the density $n^{(1)}$. The E_{xc} is approximated by that of an uniform electron gas and a constant background charge[19]. Although in a real molecule or solid the density various a lot, it works surprisingly well. One cause for that is that the E_{xc} obeys sum rules so that it depends only on the spherical average of the exchange and correlation hole ($h(\vec{r})$). The calculations usually show a strong over-binding [10]. "LDA calculations are known for dramatic underestimates of the width of the band gaps."[103] If the calculation includes the spin, it is usually known as local spin density approximation (LSDA).

The calculated bandgap of pure CaF_2 using LDA is $7.461\,\text{eV}$.

GGA (e.g. PBE)

Improving the results using the next term of the Taylor expansion of the local density, namely the gradient, fails because the sum rules were violated. Becke suggested a dimensionless reduced gradient $g = \frac{\nabla n}{n^{\frac{4}{3}}}$. This generalised gradient is largest not near the nucleus but at the tail of the wave function. Using this in an enhancement factor the over-binding can be reduced. "Density functional theory with LSDA or GGA functionals includes self-exchange and self-correlation, both of which are unphysical. As a consequence such functionals tend to predict too small a HOMO-LUMO gap in molecules or too small a band gap in solids."[19, p.10759]

The most widely used functional by Perdew, Burke and Ernzerhof (PBE)[65] is

$$E_{xc}^{\text{PBE}} = \int d^3r \quad n\varepsilon_x^{\text{unif}}(n)\, F_x \left(\frac{|\nabla n|}{2k_f n}, \dots \right) \tag{2.15}$$

The bandgap of pure CaF_2 using PBE is 7.115 eV.

Hybrid Functionals (e.g. HSE)

Since band gaps are underestimated by DFT and overestimated by Hartree Fock calculations (direct 20.77 eV [17] / indirect 20.43 eV [85]), some kind of interpolation improves the result. This is the basic idea behind hybrid functionals. The DFT-exchange energy is partly replaced by the exact (Hartree Fock) exchange E_x^{HF}. The exact exchange doesn't include the self-exchange error and reduces the corresponding error[19].

$$E_x^{\mathrm{HF}} = -\frac{1}{2} \sum_{m,n} \bar{f}_m \bar{f}_n \int d^4x \int d^4x' \frac{e^2 \psi_m^*(\vec{x}) \psi_n(\vec{x}) \psi_n^*(\vec{x'}) \psi_m(\vec{x'})}{4\pi\epsilon_0 |\vec{r} - \vec{r'}|} \qquad (2.16)$$

Perdew suggested for example to use $\frac{3}{4} E_X^{GGA}$ and $\frac{1}{4} E_x^{HF}$. It can be theoretically justified that one quarter is the best fraction of exact exchange for GGA-based Hybrid functionals.[66] "In the hybrid of the local spin-density approximation (LSDA), as much as 50% of Hartree-Fock exchange is needed to obtain acceptable thermochemistry."[100] In solids the exchange is quickly screened and cancels with the correlation energy. This is already taken into account in LDA. Cutting of the long range part of E_x^{HF} improve the results further and reduces the computational effort. The Heyd-Scuseria-Ernzerhof (HSE) functional[31, 28, 30, 48] applied in this work uses this approach. The used functional variant is called HSE06 [48] and includes an corrected parameter of the original HSE03 functional [28, 30, 31]. Both functionals yield relatively similar results. In this paper with HSE always the HSE06 variant is meant. Some cited paper used the original HSE03 version, which is always mentioned in the context and only used as a general benchmark for screened hybrid functionals. For the range separation the error function is used.

$$\frac{1}{r} = \underbrace{\frac{\mathrm{erfc}(\omega r)}{r}}_{\text{short range (SR)}} + \underbrace{\frac{\mathrm{erf}(\omega r)}{r}}_{\text{long range (LR)}} \qquad (2.17)$$

The exchange functional using $a = \frac{1}{4}$ is

$$E_{xc}^{\mathrm{HSE}} = a E_x^{\mathrm{HF,SR}}(\omega) + (1-a) E_x^{\mathrm{PBE,SR}}(\omega) + E_x^{\mathrm{PBE,LR}}(\omega) + E_c^{\mathrm{PBE}}. \qquad (2.18)$$

The HSE binding energies and band gaps are much more accurate than the ones calculated with GGA. "For large-gap systems the HSE03 functional still seriously underestimates the bandgaps, whereas for metals the bandgap seems to be slightly overestimated."[62] "Only for large gap insulators, hybrid functionals do not yield

satisfactory results, essentially because one quarter of the exact exchange is insufficient to recover the correct band gap."[1][81] The calculation of the exact exchange energy (E_X^{HF}) is computationally demanding and takes 2-4 times longer than the GGA calculation.[29][2]

The bandgap of pure CaF_2 using HSE06 is $9.079\,\text{eV}$

A very popular hybrid functional is B3LYP[3][92, 27, 82], whose parameters have been fitted to a set of simple molecules and it doesn't cut off the E_X^{HF}. However it was showen that this functional fails for all kinds of metals [61]. "On the other hand, for large gap systems, with well localized electrons, the agreement with experiment ... is reasonable." [61] Another paper claims that the B3PW91 and the similar B3LYP describes pure calcium fluoride the best [85]. "The hybrid B3PW functional has been proved to yield remarkably accurate electronic and geometrical structures for CaF2 and BaF2 crystals ..."[86] The indirect bandgap of pure calcium fluoride has been claimed to be $10.68\,\text{eV}$ (B3PW) and $10.57\,\text{eV}$ (B3BLYP).

$$
\begin{aligned}
E_{xc}^{\text{B3LYP}} =& a_0 E_x^{\text{exact}} + (1 - a_0) E_x^{\text{LDA}} + a_x \Delta E_x^{\text{B88}} + \\
& + (1 - a_c) E_c^{\text{VWN}} + a_c E_c^{\text{LYP}}
\end{aligned}
\quad [82] \tag{2.19}
$$

The bandgap of the undopped CaF_2 using B3LYP is $9.15\,\text{eV}$ which is slightly higher than the HSE06 calculation. The overall results are almost the same as the HSE calculations for all calculated variants.

Used functionals

Since the exact exchange and correlation energy functional (E_{xc}) is completely unknown and some approximations in the calculation are applied, choosing the "right" functional is difficult. The quantitative and qualitative error of each functional varies depending on the material and the physical properties of interest (lattice constant, bandgap, ...) [19]. Functionals usually include parameters which are either set according to theory or empirically fitted to a set of benchmark calculations (e.g. B3LYP). It might be tempting to test many functionals against or fit the parameters to experimental data. Although this would improve the error of one calculated physical property of one material, it might worsen the results of other properties or other similar materials. It is generally recommended to choose

---

[1]This citation refers to HSE06 and HSEsol which is based on PBEsol[68, 67] instead of PBE. HSEsol[81] and PBEsol are specifically modified to describe solids. The HSEsol yields improved results on lattice constants and atomization energies and comparable bandgaps compared with HSE06

[2]This is based on an evaluation of 21 solids (metals, semiconductors, insulators) with HSE03, but the computational effort doesn't change with the newer version HSE06

[3]Becke88 exchange 3-parameter Lee-Yang-Parr-correlation

one functional with a good performance for similar materials and in general. This functional should be used through all analysis. Only results obtained with the same functional should be compared with each other.

Initially the idea was to use PBE (GGA) as a good pure DFT functional for testing the setup and computationally demanding structure optimisations.

The hybrid HSE functional (based on PBE and E_x^{HF}) would then be used to compute the physical properties as accurately as possible.

The overall error is probably so large because of the huge bandgap of CaF_2 [62]. The B3LYP (direct/indirect) CaF_2 bandgap (10.85 eV/ 10.6 eV in the paper [85] is 1 eV closer to the experimental value than our HSE results. For that reason the calculations have been repeated with an experimental implementation of B3LYP in VASP. B3PW91 the best functional in the paper is not (at least officially) supported by VASP, but B3LYP gave relative similar results in [85]. The bandgap doesn't improve very much (9.15 eV). The B3LYP internal parameters are fitted to simple molecules and not solids. The B3LYP implementation in VASP is only experimentally and one should stick with the initially chosen functional. Therefore only the HSE06 hybrid results are included in the final discussion. The HSEsol[81] functional would be another reasonable choice but was not officially supported by VASP at the beginning of this study. It would be expected that the error in the lattice constant is significantly reduced. The errors of the ground state energies would also be reduced, but the bandgap of large gap system is still about as accurate as HSE06.

In general the hybrid functionals tend to calculate the band-gap accurately for small to medium gap insulators and predict to small band-gaps for large gap insulators. This is no real concern to us, since we only need to estimate if the optical gap of doped $Th:CaF_2$ is larger than 7.8(5) eV. Since the prediction of the bandgap are usually at least 10 percent too small for large gap insulators, the computed bandgaps are probably a reliable lower boundary for the optical gap.

2.1.3. Projector Augmented Wave (PAW)

DFT is theoretically exact, except of the unknown exchange and correlation energy E_{xc}. While DFT is a huge simplification of the computational problem, its implementation is still very complicated and some additional approximation are needed. One difficulty is the representation of the electron wave functions. In the core regions the wave function has many nodes and large amplitudes but is very stiff and doesn't depend much on the chemical environment. Outside the core region the wave function has no nodes and is influenced by the bonding. In the core region some radial wave function with a large basis set is needed to represent the wave function while in the overlapping bonding region a plane wave expansion with a smaller basis set would be better. Several strategies have been developed

to efficiently represent the wave function.

The muffin-tin approximation uses two kind of representations. In spheres around each core spherical symmetric wave functions and between the spheres plane waves are used. The junction between them has to be continuous. Various methods use this approach like the augmented plane wave (APW) method and the linear muffin-tin orbital (LMTO) method.

Another approximation is the pseudopotential method. Since the core electrons are not affected by chemical bonds, only valence electrons are important and included in the computation in an effective potential. The potential is modified to include the core repulsion and that the valence wave functions are node-less. Outside the cutoff radius the potential and the wave functions are identical with the real ones. If the wave functions have the same norm than the original ones, the potential is called norm conserving pseudopotential. If that is not the case ultra soft pseudo potentials are used and augmentation charges must be added. Because of the less rapid oscillations and the smoother waves, pseudo potential wave functions can be represented by plane waves using a small basis set. The pseudopotentials are usually precomputed and taken from a database.

The projector augmented wave method (PAW) was developed by Blöchl [9]. It uses combination of the previous mentioned ideas. The true wave functions are mapped onto auxiliary wave functions (equivalent to the pseudo wave functions) that are constructed numerically convenient. The advantage is the known transformation operator. It contains the difference between the local true wave function and the local auxiliary wave function in the core region. Expectation values can be evaluated either using the transformed operator and the auxiliary wave functions or the reconstructed true wave functions. Similar the total energy can be evaluated. Because of the energy and potential independent basis set forces can be calculated using the Car-Parrinello method[16].

The frozen core approximation is used. The core electrons are shielded by valence electrons and are not influenced by chemical binding. So the wave function in a core region within the augmentation sphere can be treated constant.

Blöchl claims that his method since the all electron wave function can be reconstructed, gives access to the full charge and spin density. This is necessary for computing the hyperfine parameters. The comparison with experiments is often the only possibility to determine the exact atomic structure[10].

2.2. VASP

We employ the *Vienna ab initio simulation package* (VASP 5.2 / 5.3.4) method as devised by Kresse and Furthmüller [46]. Since for semiconductors and insulators there are well known deficiencies of the local spin density approximation (LSDA) or

the spin-polarized generalized gradient approximation (SGGA) in determining the proper gap size [49, 3, 21] and the position of the impurity states[101] we perform our calculations using the hybrid Hartree-Fock density functionals in the HSE06 version.[31, 30] To reduce the computation time we relax the cell size and the ionic positions within a PBE [65] calculation. After convergence we keep these relaxed coordinates and change to the HSE functional. The geometries were relaxed until all force components were less than $0.01\,\mathrm{eV/\AA}$. All results are obtained use the projector augmented plane wave method[9, 47] by explicitly treating 12 valence states for Th ($6s^2$, $6p^6$, $7s^2$, $6d^2$), 8 valence states for Ca ($3p^6$, $4s^2$), 7 valence states for F ($2s^2$, $2p^5$), 6 valence states for O ($2s^2$, $2p^4$) and 7 valence states for Na ($2p^6$, $3s^1$) respectively. The PAW-potentials supplied with the VASP program were used[47]. In order to avoid Pulay stress and related problems, plane waves up to a cutoff energy of $500\,\mathrm{eV}$ were included in the basis set. The Brillouin zone integration was performed over a $2\times2\times2$ Γ-centered Monkhorst-Pack k-mesh with a Gaussian broadening of $0.02\,\mathrm{eV}$. The total energy was converged to $1\times10^{-6}\,\mathrm{eV}$.

2.3. VSC-2

All calculations were performed on the Vienna Scientific Cluster 2 (VSC-2)[18] consisting of 1.314 nodes with two AMD Opteron 6132 HE 8-core Processors. Most calculations have been performed using 64 or 128 cores (8/16 nodes). The VASP program was compiled using the ELPA (Eigenvalue soLvers for Petaflop Applications)[2, 53].

2.4. Used programs

The visualization of all crystal structures was done using VESTA 3 [58][4]. The density of states was read using ASE (atomic simulation environment python modul)[4] and the DOS-plots were created using the matplotlib python library [35] by a python script. The Bibliography was organized using Jabref [36].

---

[4] http://jp-minerals.org/vesta/en/

3. Calcium Fluoride Host Crystal

This chapter describes calcium fluoride and why it was chosen as a hostcrystal. The first sections give an overview of the properties and structure of CaF_2. In the next section the most common defects and impurities are described. Finally the general doping mechanisms and the special properties of thorium are explained. This chapter except the last section (3.5) follows the chapter 2 of the thesis by Huisinga [34].

3.1. CaF$_2$ properties

CaF_2 is an ionic crystal, with divalent calcium cations (Ca^{2+}) and monovalent fluoride anions (F^-). It has fluorite structure, which is a simple cubic lattice of F^- ions with an additional Ca^{2+} ion in the center of every other cube. The melting point has been reported at about $1696\,K$ [44]. It is important to know that the specific heat has a broad peak at $1420\,K$. This is a sign of the partial melting of the anion sublattice. At high temperatures the F^-ions start hopping in the Ca-lattice[99]. CaF_2 is a large gap isolator with a bandgap of about $12\,eV$ ($11.8\,eV$ @268 K, $12.0\,eV$ @15 K [96] / direct $12.1\,eV$, indirect $11.8\,eV$ [80]).

It occurs in nature in the fluorite (or fluorspar) mineral. Fluorescence is caused by common rare earth impurities in fluorite mineral and was named after it [93]. It is used for example for optical lenses, as flux in metallurgy and to produce fluorine and hydrogen fluoride. Pure calcium fluoride is transparent from the infra-red to the vacuum ultra violet (vuv) wavelengths. "Calcium fluoride is used for optics in the whole range of the spectrum, but is irreplaceable at the extreme edges."[78] Using very pure calcium fluoride crystals with scavenger additions the short wavelength cutoff is about $125\,nm$ [83]. 'However the most demanding application for CaF_2 is DUV optical micro-lithography, where CaF_2 is a key lens material.'[78] A lot of research has been done for optical lithography used in chip production and it might become even more important in the future. Today the standard for optical lithography are ArF excimer lasers with a wavelength of $193\,nm$, there was some intense research to replace this with $157\,nm$-technology, which production use was postponed till today. The resolution of the ArF laser process was increased with immersion lithography and double/quad-pattering. [78] Recently Samsung has announced finally to start $7\,nm$ process using DUV lithography in
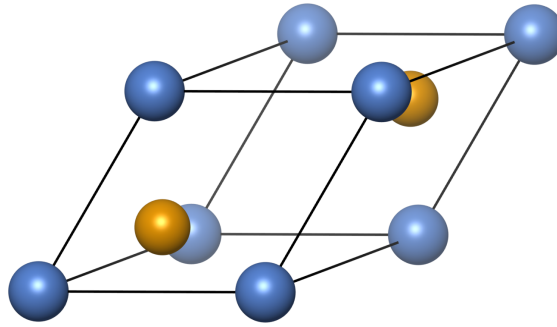
Figure 3.1.: Structure of calcium fluoride showing the decorated primitive fcc unit cell. The atoms are shown calcium in blue, fluoride in orange.(for the legend see Figure A.1)

2017. For DUV application CaF_2 is the exclusive lens material.

As a consequence the defects and excitations in the uv-range (especially 193 nm have been studied by various authors. While the Th nuclear excitation at 7.8(5) eV ($\approx$ 163 nm) is at a lower wavelength, the studies of the ultraviolet and vacuum ultraviolet range are still very useful. The thesis [78] by Rix describes laser induced colour centres after long (several months), high intensity ($1\,J/m^2$) 193 nm laser radiation. The Th excitation has lower wavelength (163 nm), which increases the energy of the photons. This induces colour centres and defects even after short radiation, if the intensity is large enough.

3.2. CaF$_2$ structure

CaF_2 is the prototype of an fluorite crystal structure. The fluorite structure in general has two kinds of realizations $X^{2+}F_2^{-}$ (e.g. CaF_2, SrF_2, BaF_2, CdF_2, HgF_2 and PbF_2) and $X^{4+}O^{2+}$ (e.g. ThO_2, UO_2). Also the so called anti fluorite structure $A_2^{+}B^{2-}$ with anion and cation exchanged exists (e.g. Li_2O, Li_2S, Na_2O, Na_2S, K_2O, K_2S, Rb_2O and Rb_2S). Fluorite is isometric. It has the Pearson symbol cF12 and the space group Fm3m, No. 225. The structure is a decorated fcc (face-centred-cubic) calcium lattice with additional fluorine ions. The lattice is fairly simple with a primitive unit cell consisting of only 3 ions. Visualising and understanding the crystal structure and its symmetry is essential. Several different unit cells and super cells will be used for the calculations and explanations. The experimental lattice constant is reported as 5.4630 Å[102, 85] and 5.4631(4) Å [91].

In Figure 3.1 the decorated primitive fcc unit cell is shown. This unit cell consist of 3 ions (1 Ca^{2+}, 2 F^-). Only the parts of the ions inside the cell (black lines) are counted. Since the primitive unit cell is the smallest possible unit cell it was used in all the calculations. For doped variants or comparison with them super
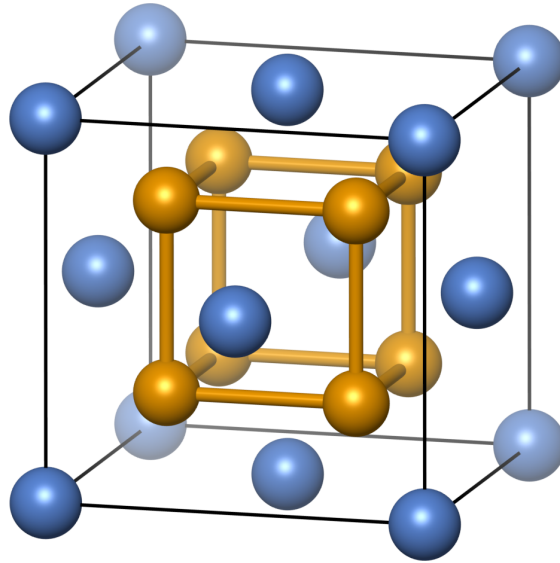
Figure 3.2.: Structure of calcium fluoride showing the decorated conventional fcc unit cell.

cells consisting of 3x3x3 primitive unit cells (27 formula units/81 atoms) are used in all calculations (see Figure 3.5).

In Figure 3.2 the decorated conventional fcc unit cell is shown. This unit cell consist of 6 ions (2 Ca^{2+}, 4 F^-). This picture is used to describe the fluorite structure and the manipulation of the cell during the doping an the charge compensation mechanism. A comparison between primitive and conventional unit cell is shown in Figure 3.3.

In Figure 3.4 the decorated conventional fcc unit cell with an additional layer of fluorine is shown. In this figure it is visible that the fluorite structure is a simple cubic lattice of F^- ions with an additional Ca^{2+} ion in the center of every other cube. This is probably the simplest description of the lattice type. Mind that this figure Figure 3.4 is not showing a periodic unit cell, but an arbitrary part of the crystal. The empty half of the F^- cubes contains hollow sites. These sites are important for defects and diffusion processes.
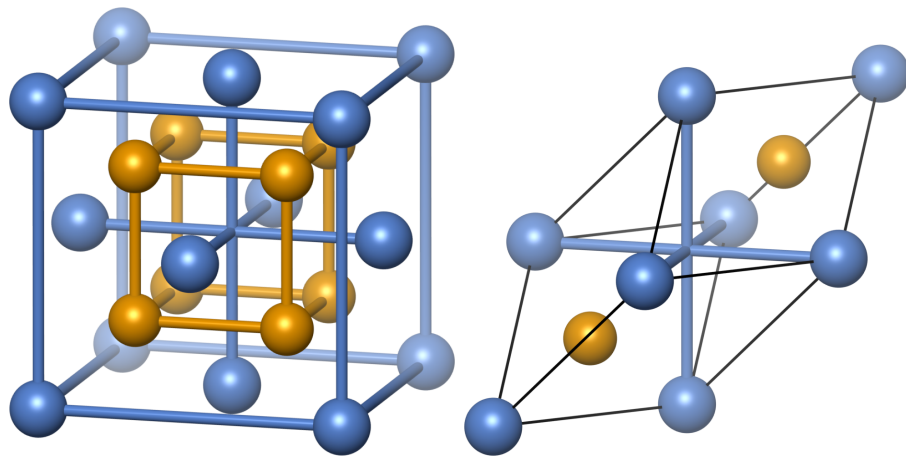
Figure 3.3.: Structure of calcium fluoride showing the decorated conventional fcc unit cell in comparison with the decorated primitive fcc unit cell. The bonds of the Ca and F sublattice are shown. The blue cross in the centre connects the same calcium ions in both cases, this helps to see which part of the conventional unit cell is part of the primitive unit cell.
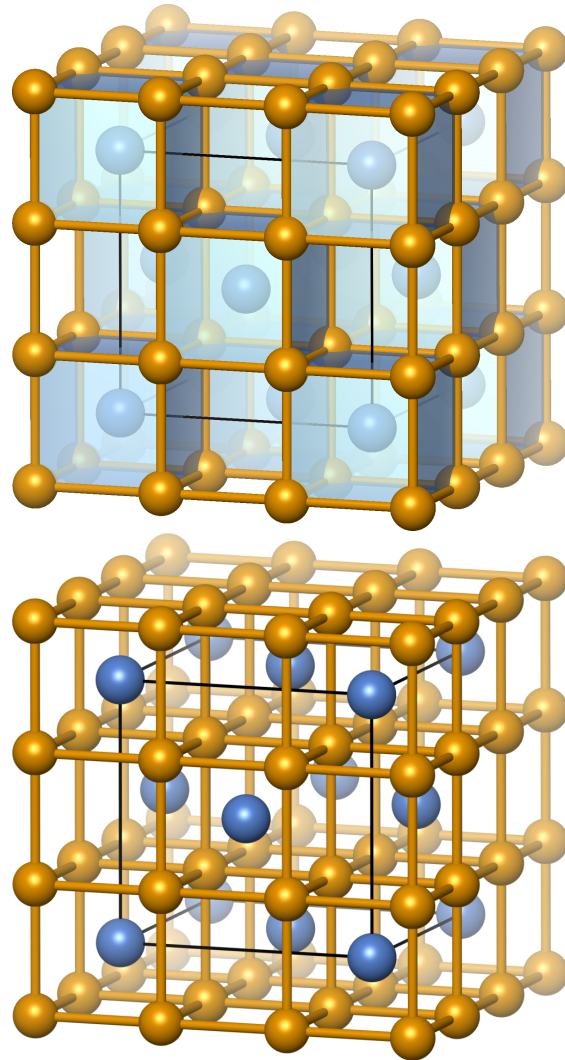
Figure 3.4.: Structure of calcium fluoride showing the decorated conventional fcc unit cell with an additional layer of fluorine ions. Fluorite has a simple cubic lattice of F^- ions with an additional Ca^{2+} ion in the center of every second cube.

3.3. CaF$_2$ surface

The surface of calcium fluoride has not been investigated at all. Nevertheless it might be an important component of laser damage. The surface treatment has a large influence on the ablation and damage behaviour after nanosecond single shot UV-laser (248 nm/5 eV) radiation. Polished surfaces have ablation thresholds between 20 J cm^{-1} and 40 J cm^{-1}. Cleaved surfaces have no well defined ablation threshold. On cleaved terraces no damage occurs, while cleavage steps are easily damaged [75, 87].

3.4. CaF$_2$ defects, colorcenters and impurities

This subsections is based also on chapter 3 of thesis [78]. A brief overview of various common defect and impurities is given. These colorcenters provide an inside about defect formation and reaction to impurities in general. Additionally some of these defects can be created or possible excited by strong ultraviolet and vacuum ultraviolet (laser) radiation. These defects can significantly reduce the transmission coefficient in visible and ultraviolet regime. The defects are only briefly described and no in depth literature review has been performed, since the aim of this thesis is on studying impurity bands of thorium doped calcium fluoride. Nevertheless this overview was important to perform the calculation and might be useful for other parts of the project.

CaF$_2$ is an ionic crystal consisting of charged cations (Ca$_2^+$) and anions (F$^-$). If there are any vacancies, interstitials or substitutes ions this could lead to a charged crystal. Usually the formation of some additional charge compensation defects is energetically more likely. Of course there could be some negative charged and positive defects apart.

3.4.1. F-center

Is a fluorine vacancy, filled by an localized electron. A half filled defect band shows up in the band structure. The defect level lies 6.75 eV above the top of the valence band [85]. This explains the optical absorption at 3.28 eV [78] as an excitation of the electron in the defect band to the valence band. The name F-center derives from the German word for colour-center (German: Farb-Zentrum). The formation energy of the F-center can be estimated by the following equation.

$$\Delta E_{\text{F}} = E_{\text{F-center}} + E_{\text{fluorine}} - E_{\text{perfect}} \tag{3.1}$$

Depending whether for E_{fluorine} the energy of a single fluorine atom or half of an F$_2$ molecule is used the formation energy is estimated to 7.87 eV [85] or more recently

to 1.35 eV [50]. This shows that the formation energy of an defect depends on the calculation method. Since a single F-atom is not observed in nature, the second approach is more realistic.

3.4.2. M-center

M-centres consist of two neighbouring F-centers. The energy needed for the lattice distortion by an F-center is reduced by another nearest neighbour F-center by about 0.43 eV [78]. The preferred relative position of the F-centers is the 100 direction [50]. The band structure is similar to the F-center but has a double occupied defect band. The absorption bands have been reported at 2.4 eV and 3.4 eV [78].

3.4.3. R-center

Three neighbouring F-centers are called R-centers [34].

3.4.4. Ca-Colloids

More F-centers result in larger regions free of F-ions. These regions are stable because the lattice constant of the Ca sublattice (5.46 Å) is only 2.2% smaller than that of pure Ca (fcc, 5.59 Å [8]). The binding energy has been estimated as 0.586 eV per F-center [78].

3.4.5. V_k-center

It is also called self trapped hole. The V_k-center is an localized hole. The lattice is distorted and an negative F_2^--dimer along 100 direction is formed. The F-ions are slightly displaced towards each other. The absorption band is 3.87 eV. This defect is not stable at room temperature [78].

3.4.6. H-center

H-center is an F-interstitial. Several different distortions have been proposed. Commonly an F_2^--dimer along 111 direction has been reported [78]. DFT calculations (GGA) show an F_4^{3-} complex with a large lattice distortion [50]. An optical absorption is observed at 4.0 eV. The formation energy has been calculated to be 6.82 eV [50] (using $\Delta E_H = -\Delta E_F - \Delta E_{F\text{-}H}$). In this calculation half of an F_2 molecule was used.

3.4.7. I-center

An ionized H-center is also called I-center. It consists of an negative fluoride ion at an interstitial site. It is found as a charge compensation for threevalent rare earth ions. As an intrinsic defect it can be either an ionized H-center or if a thermal excited anion moves to an interstitial place (see Frenkel defect subsection 3.4.9).[34]

3.4.8. Anion vacancy

It can be either created during the formation of a Frenkel defect (see subsection 3.4.9) or it is a charge compensating defect for a monovalent alkaline ion dopant.[34]

3.4.9. (Anti-)Frenkel defect

A Frenkel defect (or Frenkel pair) is usually a combination of a vacancy and an interstitial of cations, while the anion sublattice remains unaffected. If instead of the smaller cations the anion form interstitial and vacancy pairs, these are called anti Frenkel pairs. In calcium fluoride only anti Frenkel pairs of anions occur [79]. The formation energy depends on the distance between the hole and the interstitial.

The formation energy has been calculated using the difference between two separated (infinite distance) F- and H-centers and a perfect crystal.

$$\Delta E_{\text{F-H}} = 2E_{\text{Ca}_{32}\text{F}_{64}} - E_{\text{Ca}_{33}\text{F}_{63}} - E_{\text{Ca}_{33}\text{F}_{65}} \tag{3.2}$$

The formation energy $\Delta E_{\text{F-H}}$ has been reported as $-8.17\,\text{eV}$ [50] and $-7.52\,\text{eV}$ [78]. Although both calculations use the same super cell and equation, the difference is still $0.65\,\text{eV}$.

Frenkel exciton

Frenkel defects should not be mixed up with Frenkel excitons. An exciton is a bound state of an electron hole pair and doesn't change the crystal lattice. A Frenkel exciton is a strong bound pair which can even localize at an single atom. It is basically an excited atom, but it can move from one atom to another and consequently through the whole crystal [42].

3.4.10. Self trapped exciton (STE)

An self trapped exciton is a nearest neighbour F-H pair. It can be created by VUV radiation and

"The self-trapped exciton (STE) in CaF_2 is formed by exciting an electron into the conduction band, thereby creating an electron-hole pair, which can localize by lattice distortion forming an STE. ... The structure is of special interest, because it is the initial defect structure formed in the lattice under DUV irradiation and is as such a precursor for stable F-H pairs, ... The recombination of the STE can occur via an optical forbidden transition showing fluorescence at 278 nm [4.5 eV], ..."[78]

3.4.11. Oxygen

Oxygen is a very common impurity in calcium fluoride. Thermodynamic calculation shows that hydrolyses with moisture is more favourable than oxidation [87]. The divalent oxygen ions substitute for the monovalent fluorine anions with similar ionic radius (Table 3.1). "To restore charge neutrality, this defect is accompanied by a fluorine vacancy." [88] This defect is called $O^{2-} V_a$. The dipole of the oxygen-vacancy center can be used to measure the oxygen concentration. The dipole is orientated in [100] direction. An neighbouring F^- anion needs 0.47 eV to jump to the empty place and the dipole changes its direction to [110] [87]. Absorption-bands at $185\,nm(6.7\,eV)$[59, 72], $146\,nm(8.5\,eV)$[72] and $135\,nm(9.2\,eV)$ [87] have been reported. At higher concentration defect aggregation occurs. Oxygen aggregates have an absorption peak at 6.8 eV at high and 6.25 eV, 7.2 eV and 8.8 eV at low oxygen concentration [73]. The oxygen-vacancy dipoles dissociate under radiation with ultraviolet light pulses with $148\,nm(8.4\,eV)$ wavelength [73]. Slow luminescence (several millisecond) of the excited states enables higher excitations to be populated by subsequent laser pulses. This can cause the oxygen-vacancy dipole to dissociate to F_{2H}^+-centres. Fast repeated VUV-laser-pulses can dissociate oxygen-vacancy centres and reduce luminescence [88]. An O^-ion substitute for a fluorine has an absorption band of about 7 eV [59]. In summary oxygen impurities have several absorption bands in the VUV-region, but not necessarily exactly at $7.8(5)\,eV$. Oxygen impurities should therefore be avoided.

3.4.12. Hydrogen

The hydrogen atom can either sit on fluorine sites (H_s^- centers) or on interstitial sites (H_i^0 centers). It has been computed that the substitute H_s^- center introduces a slightly attractive displacement the neighbours. The calculated optical absorption 8.17 eV [86] from the H_s^- groundstate band to conduction band (CB) is in some agreement to the experimentally value 7.65 eV [5]. In case of the hydrogen interstitial (H_i^0 center) the calculated band gap is 9.15 eV(spin up) respectively 7.44 eV(spin down) [86]. No experimental data for the H_i^0 case have been found.

Ion	Ca	Th	Ce	U	U	Na	F	O
Charge	2	4	3	4	6	1	-1	-2
Coord.No.	VIII	VIII	VIII	VIII	VIII	VIII	IV	IV
Radius[Å]	1.26	1.19	1.283	1.14	1	1.32	1.17	1.24
	0.0%	-5.6%	1.8%	-9.5%	-20.6%	4.8%	0.0%	6.0%

Table 3.1.: Ionic radii of take from [84]. The values are the effective crystal ionic radii, which are based on $r_{ion}(O^{2-}) = 126\,\text{pm}$ (coord.no. VI). Ions are not like hard spheres and their approximate radii depend on the coordination number in the crystal. The size relative to the cation(Ca)/anion(F) is given in th last row.

There are reported absorption bands for hydrogen impurities at e.g. $7.65\,\text{eV}$ [5], which is relatively close to the Th nuclear excitation at $7.8(5)\,\text{eV}$.

3.4.13. Lead (Pb)

Lead (Pb) is important since PbF_2 is usually used as an oxygen scavenger. Pb doped CaF_2 has an absorption line at $7.6\,\text{eV}$. The article [63] explains the technique used for growing Pb:CaF_2 and states that the standard PbF_2 scavenger process doesn't leave any Pb impurities and Pb needs to be added in a separate step. So using PbF_2 as a scavenger is no problem.

3.4.14. Summary

The subsections 3.4.1 till 3.4.10 describe intrinsic defects, which can be created by strong laser radiation. Afterwards some common impurities were described. Sodium is another possible impurity which is described later as a (co-)dopant in subsection 3.5.2. Generally there are many defects and impurities, which have absorption bands in the VUV-region or are created / excited by VUV-radiation. In general all kinds of impurities should be avoided. Therefore oxygen and sodium were included in some of our calculations to simulate some impurities. The creation of laser induced impurities was not studied in the thesis, but many studies can be found in the literature. The probability of such impurities highly depends on the exact energy, intensity and duration of the laser radiation.

3.5. Doping in CaF_2

Since calcium fluoride is used as an optical material in a wide range of wavelength including vacuum ultra violet, impurities modifying the optical qualities have been

Impurity	Pb^+	Ce^{3+} Type II (int.)	Pr^{3+}
Absorption (nm)	154, 164 and 204	180, 200, ...	150 - 200
Absorption (eV)	8.1, 7.6, 6.1	6.9 , 6.2	8.3 - 6.2

Table 3.2.: All studied impurities in CaF_2 with absorption bands below $200\,\mathrm{nm}$ mentioned in [89].

studied extensively. Nevertheless neither experimental nor theoretical studies of thorium doped calcium fluoride have been found, only briefly mentioned the similarity with U^{3+} [15]. Although many other rare earth (RE) metals were studied almost all of them have a different oxidation number. Most of them like cerium and all lanthanides are trivalent ions. A review article over rare earth impurities for deep ultra violet applications is [89]. Only Pb^+, Ce^{3+} type II (int.) and Pr^{3+} have reported absorption bands below $200\,\mathrm{nm}$ (see Table 3.2). Although the review is about deep ultraviolet applications, it is not known if all studied papers measured in the region of $200\,\mathrm{nm}$ to $150\,\mathrm{nm}$. The ionic radii of common dopants and impurities are given in Table 3.1 for the coordination number of the cation/anion position in fluorite. The dominant charge compensation method depends on the condition during the crystal growth. If there are any other impurities present (O, Na, H) or any excess fluoride (e.g. using ReF_2 for doping).

3.5.1. Cerium (Ce^{3+})

Cerium is a trivalent lanthanide, directly above Th in the periodic table. Calcium fluoride doped with cerium or other trivalent rare earth ions (RE) are used as scintillators. Therefore the absorption, excitation and luminescence spectra have been studied extensively. The trivalent Ce ion substitutes for an divalent Ca cation. The Ce ion has one unbound electron which requires some charge compensating mechanism. Several have been proposed and measured in literature. The proposed charge compensations are fluorine interstitials on various sites, a calcium vacancy, an oxygen substitute on an fluorine site and sodium (Na) co-doping.

F_i^- **(100) C_{4v}:** An F interstitial at a nearest neighbour (100) empty site, creating a center with tetragonal C_{4v} symmetry. (All charge-compensator coordinates are given in the crystallographic (hkl) notation, in units of half of the lattice constant ($\frac{1}{2}a_0$). The absorption line at $313.17\,\mathrm{nm}$ is due the $4f \rightarrow 5d$ transition of Ce^{3+} at the C_{4v} site [60]. In a more recent paper absorption lines ($4f \rightarrow 5d$) at about $307\,\mathrm{nm}$ (e_g) and $200(10)\,\mathrm{nm}$ (t_{2g}) have been reported [56].

F_i^- **(111) C_{3v}:** An F interstitial at next nearest neighbour (111) empty site, creating a center with trigonal C_{3v} symmetry. The absorption line at $311.8\,\mathrm{nm}$

is due the $4f \rightarrow 5d$ transition of Ce^{3+} at the C_{3v} site [52].

Ca_{vac}^{2+} (200)/(110): The possibility of a calcium vacancy has been mentioned in literature, but no related experimental data has been found.[1] A possible explanation is that a calcium vacancy changes the local charge by $2e$ but only $1e$ is needed to be compensated for trivalent Ce substituted for divalent Ca.

O_s^{2-} ($\frac{1}{2}\frac{1}{2}\frac{1}{2}$) C_{3v}: If there are any oxygen impurities, oxygen likely substitutes for a nearest neighbour fluorine.

Na_s^{1+} (200)/(110): If calcium fluoride is co-doped with sodium (Na) or any other monovalent ion (H^-, D^-, Li^-), it substitutes for Ca^{2+}. Since the nearest calcium sites are further away than fluorine interstitials, the cubic symmetry will remain in nearest neighbour approximation. A detailed description will be given in the next subsection 3.5.2.

Cubic site O_h: If there is no local charge compensation the impurity site remains in cubic symmetry O_h and the unbound electron would occupy an empty state in the conduction band and the crystal would be metallic. This is not observed experimentally and some sort of remote charge compensation is expected. If the hot melt is cooled rapidly, remotely compensated O_h sites are predominant. The absorption line of Ce^{3+} O_h sites was identified at 309.23 nm. While measuring a laser excitation spectra of $Ce^{3+}:Na^+:CaF_2$ a spectral hole at the O_h excitation band was observed. It is assumed that when charge compensated sites were selectively excited, they were photoionized and the free electrons were trapped at uncompensated O_h Ce^{3+} sites, reducing them to Ce^{2+} sites. [60]

The predominant charge compensation of doped calcium fluoride (without codoping) is F_i^- interstitial (100) with tetragonal C_{4v} symmetry [104]. The crystal field of the fluorine interstitials has been computed by Manthey [52]. The F_i^- (111) C_{3v} site is not stable at room temperature. After 1 h of irradiation with a 308 nm laser at 80 K the predominant charge compensation changes to F_i^- (111) C_{3v}. Irradiation at room temperature produces Ce^{2+} and the crystal turns reddish-brown. After heating above 100 °C the crystal becomes clear again [33].

The charge compensation and the absorption bands of $Ce:CaF_2$ depend on crystal preparation [55] and can change after intense radiation.

---

[1]Also the possiblity of Ca vacancy in the undoped CaF_2 has been mentioned in [15].

3.5.2. Sodium (Na$^+$)

Sodium used to be a common impurity in CaF_2 . Several papers mentioning co-doping NaF as a charge compensation[70, 71]. One studies the excitation spectra of calcium fluoride doped with light lanthanides (Ce^{3+}, Pr^{3+}, Nd^{3+}, Sm^{3+}, Eu^{3+}) [70]. There are some emission lines around $164\,nm$ measured. The Na^- ions alter the cation (Ca) sub lattice, while usually F-interstitials are observed as charge compensation. The distances between RE^{3+} and Na^- on the cation sub lattice is larger than the distance to nearest neighbour F-interstitial. Using Na as a charge compensation the symmetry of RE-site remains cubic in nearest neighbour approximation. This minimizes the electric field gradient on the RE site compared to F-interstitials.

Co-doped Ce_3^+:Na^+:CaF_2 has been investigated. A summary of many possible Na-Ce pairs is given in [60]. The ratio between the different charge compensation mechanisms depends on the cooling rate of the melt. While after slow cooling solely F_i^- (100) C_{4v} sites are observed, after rapid cooling only a couple of Na^+ sites seem to be occupied. The Na compensated absorption lines are centred about the remotely compensated O_h line. "Presumably this will hold true for many other trivalent rare-earth sites, creating inhomogeneous broadening at will." [60] Radiation of the co-doped crystal produces Ce^{2+} at $80\,K$ and blue colour at room temperature. The blue coloured crystal has an emission line of an $F_{2A}{}^+$ center (two F-centers adjacent to Na)[33].

Using this technique for thorium doped calcium fluoride would have the advantage of cubic symmetry, but since two charge compensations would be necessary, several angles between 2 Na-ions or Na-substitutes and F-interstitials are possible. This will broaden the Th-excitation. Excess Na would need charge compensations too and could be a possible center for defect creation, another impurity band and possible complications. In sodium (Na) doped calcium fluoride two types of charge compensations have been suggested. It has been reported that Na substitute for Ca is more likely to be compensated by a F vacancy than a Na interstitial [38]. Na stabilized defects (F-center, M-center), especially increased laser induced defects have been described [78, p.32]. No detailed analysis of this method has been performed.

3.5.3. Uranium (U^{2+}, U^{3+}, U^{4+}, U^{5+}, U^{6+})

Uranium has reported oxidation states of 3+,4+,5+ and most common 6+. It also occurs in uranium doped calcium fluoride in several different valence states. CaF_2:U^{3+} has been studied for laser applications [25] and CaF_2:U^{4+} as a passive Q-switch for near infra red lasers[23]. Although CaF_2:U has been studied for more than 50 years, the oxidation states and charge compensation mechanisms

still remains unclear [94]. The absorption spectra depend on the valence state, the charge compensation mechanism, the site symmetry and the atmosphere during crystal growing [94]. The reported valence states are 2+ [24], 4+, 4.3+,6+ [94], 5+ [51] and mixed valence states. There are several proposed charge compensation mechanisms for CaF_2:U.

For the trivalent U^{3+} case a substitution of nearest neighbour F^--ion $\left(\frac{1}{2}\frac{1}{2}\frac{1}{2}\right)$ by an O_s^{2-}-ion C_{3v}, F_i^--ion in the nearest interstitial site (100) C_{3v} [15] and F_i^--ion in the next nearest interstitial site (111) C_{4v} like for RE^{3+} are possible.

As a charge compensation for tetravalent U^{4+} non local (cubic sites O_h) or partly local charge compensation have been suggested. An example would be substitution of the nearest neighbour F^--ion $\left(\frac{1}{2}\frac{1}{2}\frac{1}{2}\right)$ by an O_s^{2-}-ion C_{3v} and some remote O_s^{2-}-ion substitute on an fluorine site [54]. Another paper suggest that two nearest neighbour F^--ions $\left(\frac{1}{2}\frac{1}{2}\frac{1}{2}\right)/\left(\frac{\bar{1}}{2}\frac{\bar{1}}{2}\frac{\bar{1}}{2}\right)$ at opposite corners are substituted by two O_s^{2-}-ions C_{3v}[95]. The configuration is similar to the stable compound UO_2.[95] A recent study suggests charge compensation with either two F_i^--ions in the nearest interstitial sites (100) C_{3v} or two F_i^--ions in the next nearest interstitial site (111) C_{2v} [23].

To compensate the charge of U^{5+} [51] proposes that six of the eight nearest neighbour fluorines are substituted by O^{2-} and the other two n.n fluorine sites will be empty.

The most recent publications [94, 23] conclude that the previous reports are inconsistent and neither the valence state nor the exact charge compensation mechanisms has been identified. The occurring valence states and charge compensations highly depend on crystal preparation. The availability of excess fluorine or oxygen as a charge compensator depends on the usage of UO_2 or UF_2 as a dopant, the amount of PbF_2 as an oxygen scavenger and the atmosphere. The assignment of valence state and charge compensation is complicated, since various different states coexist. Thus the assignment of the measured absorption and electric paramagnetic resonance spectra is ambiguous [74].

It has been reported [24] that the color of CaF_2:U depends on the valence state of uranium. Calcium fluorite doped with U^{4+} (yellow) shall be reduced by strong ultraviolet irradiation to a mixture with U^{3+} (brownish) and finally to a U^{2+} (greenish). During heating to $373\,K$ reconversion to U^{4+} happens. It has also been suggested that yellow samples contain U^{4+} with oxygen as charge compensator and green samples U^{4+} are compensated by F^--ions [74].

While the assigned valence states are still debated, some sort of change of the valence state and/or the charge compensation has to be the reason for the colour change.

26

3.6. Thorium

Thorium ($_{90}$T) it is late element in the actinides series named after the nordic god Thor. There exists seven natural isotopes of thorium and 30 known radioisotopes. All of them are radioactive and unstable. Allmost all natural thorium is ^{232}Th, since it has the longest half-life of 1.405×10^{10} years. Which is even slightly longer than the estimated age of the universe. On earth it is 32th most common element. [45]

The nuclear clock will use ^{229}Th. It is not relevant for the DFT calculation which isotope will be used. The half-life of ^{229}Th is (7932 ± 55) yr [41]. It is a member of the neptunium decay series. Since practically all naturally precursors including neptunium are already decayed it is very scarce. Usually ^{233}U is created by uranium activation and α-decays into ^{229}Th, which α-decays into ^{225}Ra itself. The acquisition of ^{229}Th is very difficult.[26] The energy of the ground state doublet was indirectly measured to be about $7.8(5)$ eV ($\approx$ 159 nm)[7, 6]. It was not possible to directly measure the doublet. This is the lowest excitation energy of all known isotopes in the NuDat (Nuclear Structure and Decay Data) Database [90]. The second lowest excitation energy $76.5(4)$ eV has ^{235}U. All other isotopes have excitations energies above 1 keV [90].

3.6.1. Charge compensation for a Th ion

Thorium has a high electroposivtivity (1.3 Pauling). Usually it has an oxidation number of $+4$ and probably sits on an calcium site (oxidation nr. $+2$). So there are two unbound electrons in thorium which will be bound by some charge compensation defects. Below is a list of possible charge compensation mechanism which bound one or two electrons. Table 3.3 gives an overview how many electron charges (e) are compensated by various mechanisms. If only one electron charge is compensated by the mechanism, a second one-electron charge compensation is needed. Any one-electron charge compensations can be combined at any angle. Which combination of the charge compensation mechanisms really happens, depends on the concentrations of the elements in the melt and the energy level of the different configurations.

Possible charge compensations are:

1. F$^-$ interstitial $\langle 001 \rangle^2$ ($-1\,e$)

2. F$^-$ interstitial $\langle 111 \rangle$ ($-1\,e$)

---

[2]All position vectors are denoted in multiples of the side length of a fluorine cube ($\frac{1}{2}$ lattice constant a) relative to the thorium impurity. The angle brackets $\langle 001 \rangle$ denote all crystallographic equivalent positions to the coordinate vector [001] (e.g.[010], [100], [00$\bar{1}$] = [00 − 1], . . .).

	F	O	O	Ca	Na	$(e\text{-})$	(none)
Type	interstitial	interstitial	substitute	vacancy	substitute	hole	-
Δq	$1\,e$	$2\,e$	$1\,e$	$1\,e$	$1\,e$	$1\,e$	$0\,e$

Table 3.3.: The suggested charge compensation mechanisms. Unphysical variants are marked red.

3. F^- interstitial further away e.g.$\langle 030 \rangle$ $(-1\,e)$

4. O^{2-} substitute $\langle \frac{1}{2}\frac{1}{2}\frac{1}{2} \rangle$ for F^- in O-atmosphere $(-1\,e)$

5. O^{2-} interstitial $\langle 001 \rangle$ in O-atmosphere $(-2\,e)$

6. Ca vacancy $\langle 110 \rangle (-2\,e)$

7. Na^+ substitute $\langle 110 \rangle$ for Ca^{2+} (not all possible variants were calculated, requires co-doping Na) $(-1\,e)$

8. Charged crystal 1/2 hole(s) $e^+ (-1\,e/-2\,e)$ (for comparison only)

9. no charge compensation (none) (for comparison only)

The last two points 'no charge compensation' and 'charged crystal' are not expected to happen. They are just included for comparison and to show the importance of the charge compensation. Without charge compensation the crystal would become a metal, which is not experimentally observed. The charged crystal (artificial hole) could be interpreted as a distant charge compensation. These two variants are marked red in the tables and are not discussed in detail.

The sodium substitute Na^+ requires co-doping and would probably introduce many other defects (see subsection 3.5.2 for details). The theoretical advantage would be approximately cubic symmetry at the Th site and almost no electric field gradient. This reduces the hyperfine splitting and improves the precision of the Th-clock.

No.	Charge Compensation		angle
00	undoped CaF2		
01	e^+	e^+	
02	none	none	
03	O^{2-} substitute $\{\frac{1}{2}\,\frac{1}{2}\,\frac{1}{2}\}$	e^+	
04	O^{2-} substitute $\{\frac{1}{2}\,\frac{1}{2}\,\frac{1}{2}\}$	none	
05	O^{2-} substitute $\{\frac{1}{2}\,\frac{1}{2}\,\frac{1}{2}\}$	O^{2-} substitute $\{-\frac{1}{2}\,-\frac{1}{2}\,-\frac{1}{2}\}$	180°
06	O^{2-} substitute $\{\frac{1}{2}\,\frac{1}{2}\,\frac{1}{2}\}$	O^{2-} substitute $\{-\frac{1}{2}\,\frac{1}{2}\,-\frac{1}{2}\}$	109.5°
07	O^{2-} substitute $\{\frac{1}{2}\,\frac{1}{2}\,\frac{1}{2}\}$	O^{2-} substitute $\{\frac{1}{2}\,\frac{1}{2}\,-\frac{1}{2}\}$	70.5°
08	O^{2-} substitute $\{\frac{1}{2}\,\frac{1}{2}\,\frac{1}{2}\}$	F^- interstitial $\{-1\,0\,0\}$	125°
09	O^{2-} substitute $\{\frac{1}{2}\,\frac{1}{2}\,\frac{1}{2}\}$	F^- interstitial $\{1\,0\,0\}$	55°
10	O^{2-} substitute $\{\frac{1}{2}\,\frac{1}{2}\,\frac{1}{2}\}$	F^- interstitial $\{1\,1\,1\}$	0°
11	O^{2-} substitute $\{\frac{1}{2}\,\frac{1}{2}\,\frac{1}{2}\}$	F^- interstitial $\{-1\,-1\,-1\}$	180°
12	O^{2-} substitute $\{\frac{1}{2}\,\frac{1}{2}\,\frac{1}{2}\}$	F^- interstitial $\{-1\,1\,-1\}$	109.5°
13	O^{2-} substitute $\{\frac{1}{2}\,\frac{1}{2}\,\frac{1}{2}\}$	F^- interstitial $\{1\,1\,-1\}$	70.5°
14	O^{2-} substitute $\{\frac{1}{2}\,\frac{1}{2}\,\frac{1}{2}\}$	F^- interstitial $\{0\,0\,3\}$	-[3]
15	O^{2-} interstitial $\{1\,0\,0\}$		
16	F^- interstitial $\{1\,0\,0\}$	e^+	
17	F^- interstitial $\{1\,1\,1\}$	e^+	
18	F^- interstitial $\{0\,0\,3\}$	e^+	
19	F^- interstitial $\{1\,0\,0\}$	none	
20	F^- interstitial $\{1\,1\,1\}$	none	
21	F^- interstitial $\{0\,0\,3\}$	none	
22	F^- interstitial $\{1\,0\,0\}$	F^- interstitial $\{-1\,0\,0\}$	180°
23	F^- interstitial $\{1\,0\,0\}$	F^- interstitial $\{0\,1\,0\}$	90°
24	F^- interstitial $\{1\,0\,0\}$	F^- interstitial $\{1\,1\,1\}$	55°
25	F^- interstitial $\{1\,0\,0\}$	F^- interstitial $\{-1\,-1\,-1\}$	125°
26	F^- interstitial $\{1\,0\,0\}$	F^- interstitial $\{0\,0\,3\}$	-[3]
27	F^- interstitial $\{1\,1\,1\}$	F^- interstitial $\{-1\,-1\,-1\}$	180°
28	F^- interstitial $\{1\,1\,1\}$	F^- interstitial $\{-1\,1\,-1\}$	109.5°
29	F^- interstitial $\{1\,1\,1\}$	F^- interstitial $\{1\,1\,-1\}$	70.5°
30	F^- interstitial $\{1\,1\,1\}$	F^- interstitial $\{0\,0\,3\}$	-[3]
31	Ca^{2+} vacancy $\{1\,1\,0\}$		
32	Na^+ substitute $\{1\,1\,0\}$	Na^+ substitute $\{0\,-1\,-1\}$	120°
33	Na^+ substitute $\{1\,1\,0\}$	Na^+ substitute $\{1\,0\,1\}$	60°
34	Na^+ substitute $\{1\,1\,0\}$	Na^+ substitute $\{1\,-1\,0\}$	90°
35	Na^+ substitute $\{1\,1\,0\}$	Na^+ substitute $\{-1\,-1\,0\}$	180°

Table 3.4.: Description of all possible combinations of charge compensations. The position relative to the doped Th and the angle between the charge compensation I, thorium and charge compensation II are described in the columns. The number in the first column was arbitrary chosen (#e) and used to label the the configurations throughout the thesis.

---

[3] Since the F^- interstitial at $\{003\}$ is in the center of the supercell between the thorium substitute(s) at each corner, no angle is distinguished see Figure 3.5.
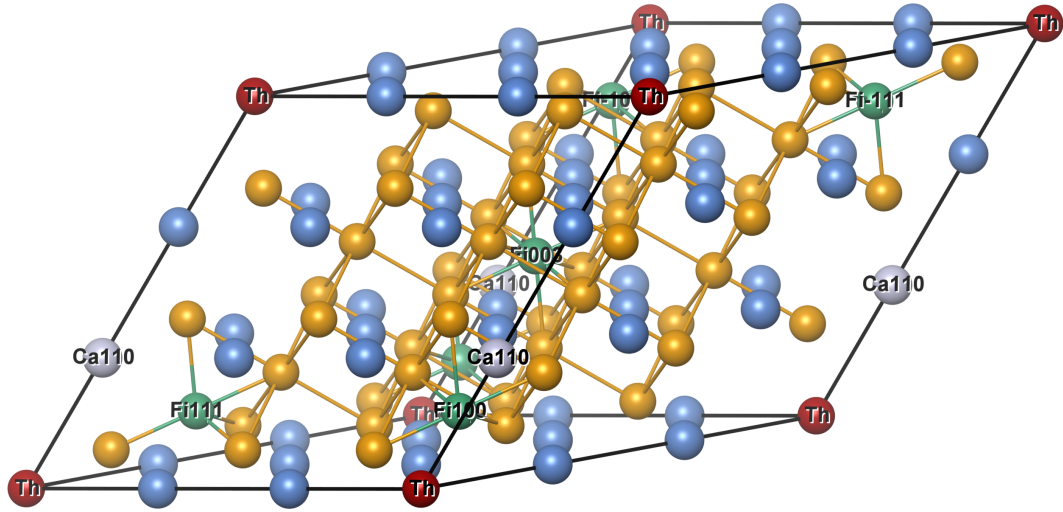
Figure 3.5.: This is the 3x3x3 primitive cell used in the calculations with the most relevant charge compensations (F interstitials, Ca vacancies). For the legend see Figure A.1

An overview of all studied charge compensation is given in Table 3.4. The last row indicates that further combinations with Na^+ (e.g. F_i^-, O_s^{2-}) are possible. The sodium Na^+ charge compensation has not been studied completely. Only Na^+-Na^+ combinations have been calculated to prove that the electric field gradient can be reduced by Na co-doping.

The arbitrary chosen numbers in the first column (0-35) are used to label the variants in this thesis. The order of the charge compensations was chosen by the elements and the total number of electrons in the supercell. The order is completely arbitrary.

The red marked variants (charged crystal 1 hole $-1\,e$ and no charge compensation) were only computed out of curiosity and are unphysical. These variants are not discussed in detail. Nevertheless their density of states are included in Appendix A.
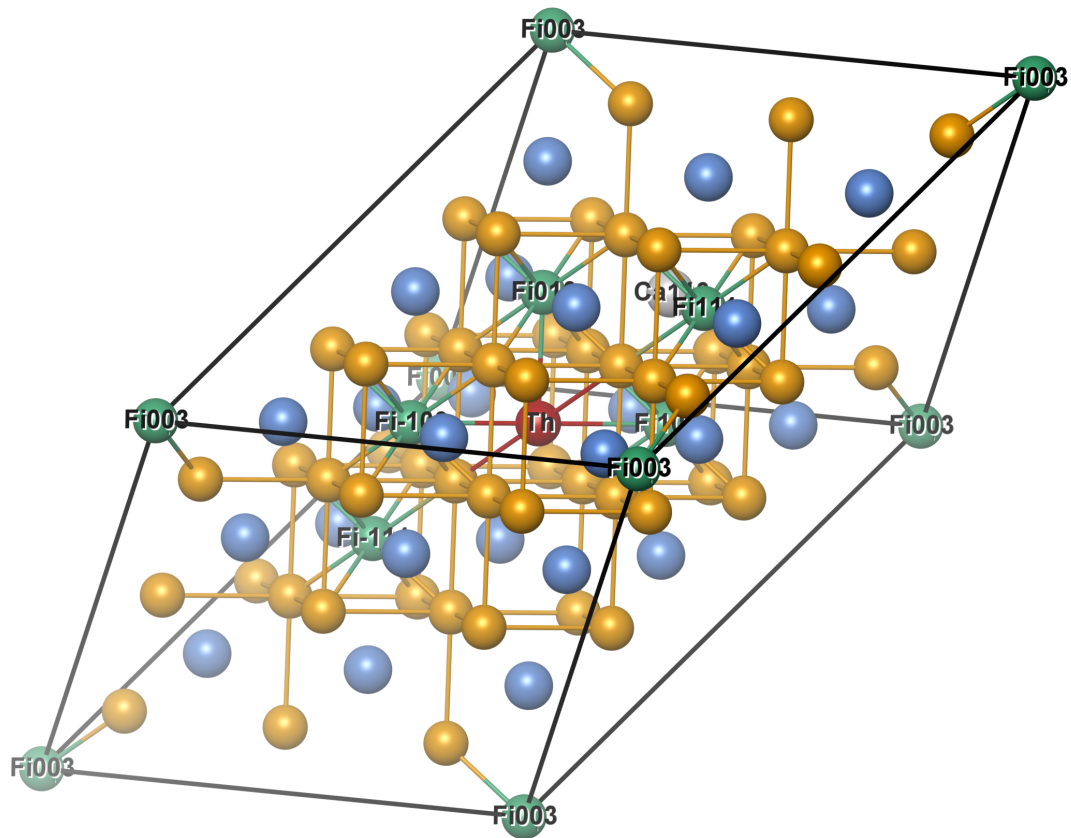
Figure 3.6.: This is a 3x3x3 primitive cell with the most relevant charge compensations (F interstitials, all possibilities) and the thorium ion shown in the centre.

4. Calculation

The calculation used a supercell containing $3 \times 3 \times 3$ primitive unit cells (81 ions undoped) with various doping variants (see Table 3.4, Figure 3.5). It will be in future refered to as the supercell or 3^3-primitive unit cells. It is a huge supercell and the computationally pretty demanding. This large cell size was chosen to study also cases were the charge compensation is not the nearest neighbour. Adding one Th atom in this supercell instead a Ca is an effective impurity concentration of 3.7% per Ca (about 10% by total weight). This supercell (81 ions undoped) was preferred over a $2 \times 2 \times 2$ conventional unit cell (96 ions) because it is smaller and computes faster.

4.1. Convergence Tests

To determine the best parameters for the calculations some convergence tests were done. For these tests the primitive unit cell or the supercell ($3 \times 3 \times 3$ primitive unit cells) were used. To save computational time for the convergence calculations the undoped crystal was used. We expect faster convergence for the undoped crystal compared to the doped variants because of the lower symmetry and in some cases unphysical geometries. Therefore very conservative settings were used. All convergence tests were done using the PBE-functional (section 2.1.2).

4.1.1. Energy cutoff

The 'ENCUT' parameter of VASP sets the cutoff energy [eV] of the plane wave expansion. As a default the largest 'ENMAX' value of all chemical elements is used. The 'ENMAX' is defined for all used pseudopotentials in the respective POTCAR files. For the used PBE pseudopotentials the maximum parameter was $400\,\text{eV}$ (see Table 4.1).

The testing was done using the primitive unit cell, since the cutoff is independent of the cell size. The test was repeated using the final k-point mesh and lattice parameter from the next tests. The final result can be seen in Figure 4.1. For these runs 16 cores (equals 1 node) was used. For consistency the energy cutoff was fixed to $500\,\text{eV}$ for all our later calculations. This is 1.33 times the maximum ENMAX and should be even sufficient for the relaxations.
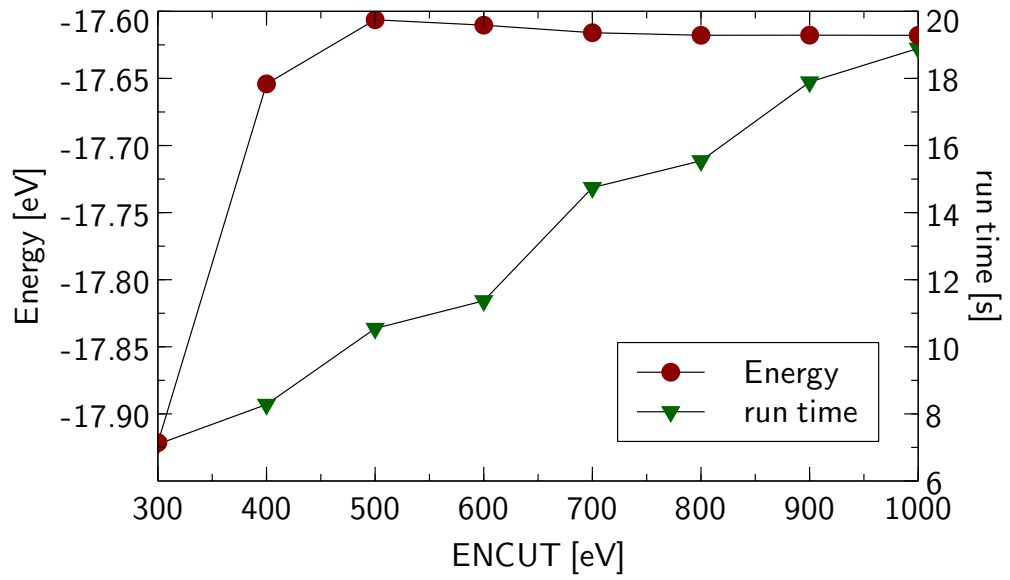
Figure 4.1.: Convergence test of the energy cutoff, calculated using a gamma centered k-point mesh $11 \times 11 \times 11$.

	Ca	F	Th	O	Na	used
ENMAX	119.6 eV	400 eV	247.5 eV	400 eV	259.6 eV	500 eV

Table 4.1.: ENMAX parameter of the used pseudopotentials[47].

4.1.2. k-points

The calculations are performed in reciprocal space on a k-point grid. The k-point mesh is generated using the Monkhorst-Pack scheme. The mesh can be shifted so that the Γ-point is always included in the mesh. Since only the k-points in the irreducible Brillouin zone are calculated, the calculation is sensitive to the chosen k-grid. Usually gamma centred meshes perform better for lower symmetry cases and less k-points need to be computed. The difference is only noticeable if there is an even subdivision.

The convergence of the primitive unit cell was only tested to validate the result of the energy cutoff. The results can be seen in Figure 4.2 using different Γ-centred meshes. A $11 \times 11 \times 11$-k-mesh was used for calculations with the primitive unit cell.

For the doped calculations the supercell (3^3-primitive unit cells) was used. The convergence was tested using a regular Monkhorst-Pack scheme. For these calculations 64 cores (4 nodes) were used. The runs with a large even subdivision (N=14,16) failed because of low virtual memory. The energy for this large supercell already converges at a subdivision of 4 k-points in each direction. It was expected that a larger supercell in real space would need less k-points in reciprocal space. It can be seen that the runtime of even subdivision is much larger. This is because the k-grid is not Γ-centred. A second test with a Γ-centred mesh was performing much better (see comparison Figure 4.3). Excellent convergence was achieved with more than $4 \times 4 \times 4$-k-points. Nevertheless because hybrid calculations are computationally extremely demanding, the HSE calculation could only be done on a $2 \times 2 \times 2$-k-mesh. Note that the relative error of the groundstate energy (supercell) was still only about 8×10^{-6} using 2^3k-points (compared to 7×10^{-8} with 4^3k-points). The energy difference of the most probably charge compensation mechanisms (2 F interstitials 90° or 180°) is with 0.4 eV larger than the absolute error of 0.004 eV by two orders of magnitude.

4.1.3. Lattice constant

The lattice constant (a) of DFT-calculations is not necessarily the same as the experimental value ($a = 5.4630\,\text{Å}$ [102, 85]). The cell size was relaxed until the force was less than $0.01\,\text{eV}\,\text{Å}^{-1}$. The ion positions were relaxed in a later step for all charge compensation variants. The PBE functional was used. The energy cutoff of the plane wave expansion was 500 eV to avoid Pulay stress. The Brillouin-Zone integration was performed on a $9 \times 9 \times 9$-Γ-centred k-mesh using the tetrahedron method. The error of the total energy was less than $1 \times 10^{-5}\,\text{eV}$. This calculation was started using 1.01 times the experimental value.

The relaxed lattice constant is only 0.66% larger than the experimental value,
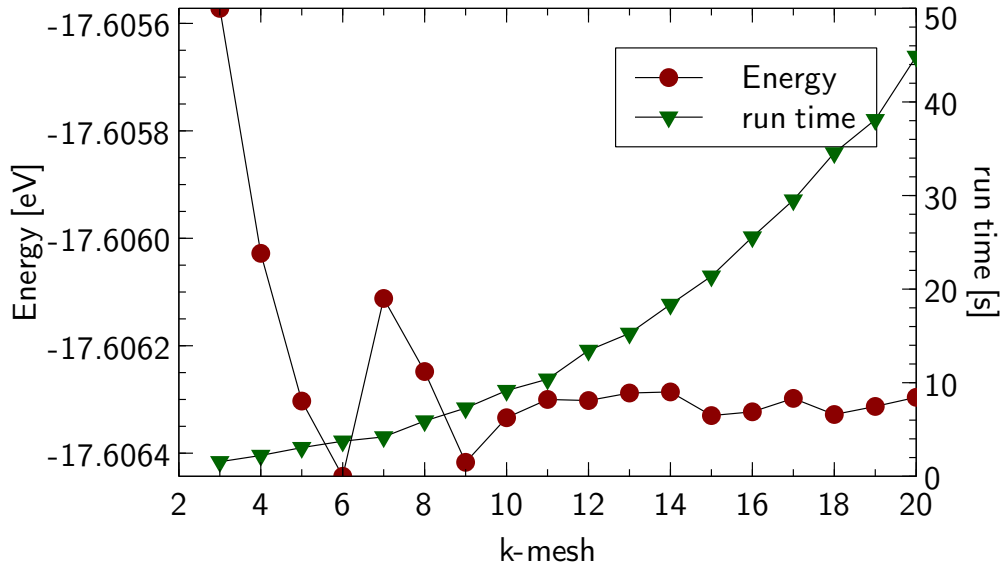
Figure 4.2.: The convergence of the total energy with increasing density of the k-mesh and the runtime for the primitive unit cell. The calculation used 16 cores.
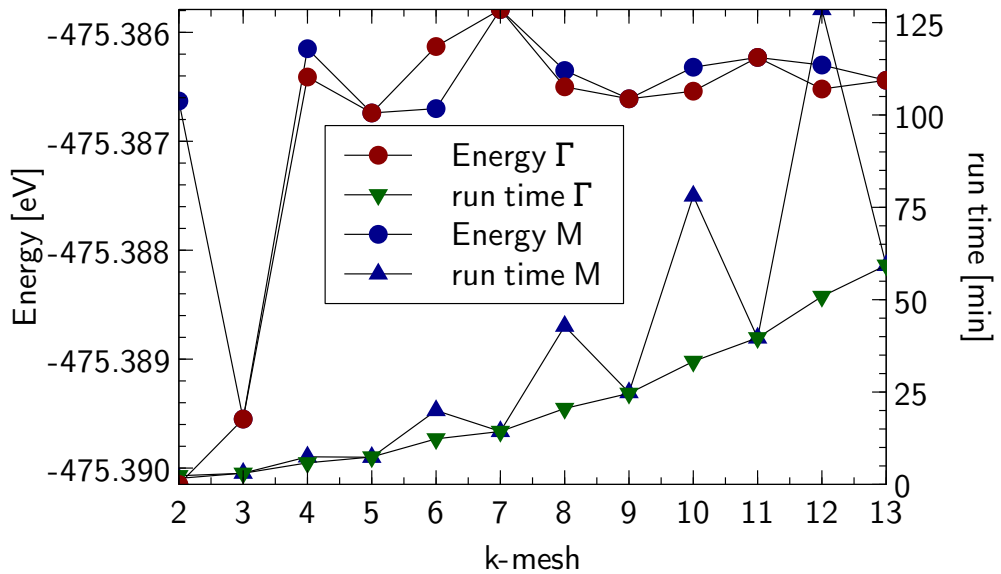
Figure 4.3.: The convergence of the total energy with increasing density of the k-mesh and the runtime for the primitive unit cell. The standard Monkhorst mesh is compared to a Γ-centred mesh. The calculation used 64 cores.

which gives confidence in the accuracy of the method. This result was rounded to 0.7% and used during all the calculations ($1.007 \times a$).

Because of the large supercell a more exact relaxation with the hybrid HSE functional was not possible to do.

4.2. Setup

Several calculations were done for each charge compensation variant in Table 3.4. For each structure the ion positions were relaxed. Then a standard PBE calculation (using 3^3-k-point mesh) and a PBE calculation with a sparse 2^3-k-point mesh were done. The converged wavefunctions in the WAVECAR file of the sparse k-mesh calculation were then used as a starting point for the following hybrid HSE calculation. The sparser k-point mesh and the pre-converged wavefunctions were used to speed up the HSE calculations. The exact settings for all the calculations are given in the following subsections.

This calculation were automated using the two scripts given in the appendix section B.1. The root directory contained all the different structures in the POSCAR files (e.g. 'POSCAR_23_F100_F010.vasp') and a subdirectory 'nstd_HSE' with the configuration files of all calculations and. The script 'create_subf_spin.sh' (Listing B.1) created a subdirectory for every structure and copied the necessary configuration files from 'nstd_HSE'. The POTCAR file contained the pseudowave functions of the atoms in the used order (Ca, F, Th and O). If the structure contained sodium a different POTCAR file was automatically copied (containing Ca, F, Th and Na). For each structure the script 'start.sh' (Listing B.2) was called. This script changed the settings and started the calculation in the respective subdirectories. The right number of electrons was set according to Table A.1, the name of the calculation was given and those calculations which are required before the actual calculation can be started were set. Using this system the calculations for all of the 36 variants could be started by a single command. If some changes were necessary similar scripts were used to rerun some calculations or add an additional calculation for all variants. To support readers studying a similar wide range of configurations all the scripts are included in section B.1.

4.2.1. Relaxation

Since the volume was already relaxed together with the convergence tests for pure CaF_2, in this next relaxation the cell shape and volume was kept constant and only the ion positions were relaxed. The calculations used a minimum of 6 electronic self consistent steps until the energy was converged to 1×10^{-2} eV. The ions were relaxed until the force was less than $0.05 \, \mathrm{V \, \mathring{A}^{-1}}$ in a maximum of 10 ionic

steps using a conjugate-gradient algorithm. The calculation used a dense 3^3-k-point mesh and the PBE functional (GGA section 2.1.2). Gaussian smearing with $\sigma = 0.01\,\text{eV}$ was used and to avoid wrap around errors PREC= Accurate flag was used. These calculations were performed on 16 cores and the runtime was between $17\,\text{min}$ to $248\,\text{min}$. The large difference of the runtimes reflects the vast range of configurations included the perfect pure CaF_2 crystal and some configurations with several interstitials. It was challenging to find a setup which fitted all the configurations. For all following calculations the relaxed positions were used.

4.2.2. PBE

Next an accurate standard GGA-calculation with the PBE functional section 2.1.2 was done. This calculation was used to compare the PBE results in energy, bandgap and density of states with the hybrid HSE calculations. The same basic settings as for the relaxations were used and the density of states and electric field gradient were computed additionally. For the computations 64 cores were used. The run time was between $7\,\text{min}$ to $24\,\text{min}$.

4.2.3. pre-HSE

The calculation with the PBE function were repeated on a sparser 2^3 k-point mesh and the converged wave function was used as a starting point for the following HSE calculation. This calculation 48 cores were used and the run time was between $9\,\text{min}$ to $22\,\text{min}$.

4.2.4. HSE

The advanced hybrid HSE functional was expected to produce the most accurate results. Unfortunately the hartree fock part is computationally very demanding and some settings needed to be reduced. It was only possible to use a sparser 2^3 k-point mesh and Gaussian smearing with $\sigma = 0.02\,\text{eV}$. The parameter PREC-FOCK= Fast was set. This means that the FFT-grid just encloses the cutoff sphere determined by ENCUT. The energy, bandgap, electronic density of states (DOS) and the electric field gradient (EFG) were computed. For these calculations 128 cores were used. The run time was between $11\,\text{h}$ to $24\,\text{h}$.

Listing 4.1: The INCAR file used for the HSE calculations.

```
1  SYSTEM =   Hg_23_F100_F010
2  ISPIN =2
3  LORBIT = 11
4  ISTART =1
5  ICHARG =1
6  ENCUT =500    # poscar max Encut = 400
7  LHFCALC = .TRUE. ; HFSCREEN = 0.2
8  ALGO = All   ; TIME = 0.5
9  PRECFOCK= F #fast    (coarse grid for HF, soft augmentation charge
      )
10 ISMEAR = 0
11 SIGMA = 0.02
12 NEDOS = 2001
13 # NELECT = 594
14 NBANDS = 384
15
16 # LREAL = Auto
17
18 LEFG = .TRUE.
19 LELF = .TRUE.
```

5. Results

The ground state energy, electronic density of states, bandgap and the electric field gradient of all the configurations were calculated using the PBE and HSE method. A comparison of the two calculations is given in Table 5.1, Figure 5.1, Figure 5.2 and Figure 5.14.

The ground state energies can only be compared between configurations with the same stoichiometry. Therefore only differences of the ground state energies relative to the lowest energy within the same stoichiometry are given. The configurations were sorted by stoichiometry and energy. If only one calculation within a stoichiometry was done, the energy cannot be used to determine the probability compared to the other stoichiometries. If the crystal does not contain any impurities only either two F interstitials or a Ca vacancy would be possible charge compensations. The ground state energies are given in Table 5.1 and Figure 5.1.

The bandgaps are given in Table 5.1 for the PBE and the HSE calculations. The full electronic density of states are plotted in the appendix section A.1. The most interesting cases are discussed in the following subsections.

The splitting of the energy states caused by the electric field gradient could be used to experimentally verify which charge compensation is present in $Th:CaF_2$. The results are discussed in section 5.5.

The data of the calculations using charged crystals or no sufficient charge compensation are given in Table 5.2 and discussed in section 5.6 at the end of this chapter.

Number	Charge Compensation	angle	Energy [eV] PBE	Energy [eV] HSE	Bandgap [eV] PBE	Bandgap [eV] HSE	HSE EFG V_{zz} [V/Å²]	η
00	undoped CaF2		0	0	7.115	9.0786	0.018	0.107
23	F^-_{int} {1 0 0} F^-_{int} {0 1 0}	90°	0	0	5.9516	8.5935	222.967	0.478
22	F^-_{int} {1 0 0} F^-_{int} {-1 0 0}	180°	0.3823	0.4201	5.4163	8.0672	-296.659	0
25	F^-_{int} {1 0 0} F^-_{int} {-1-1-1}	125°	0.5243	0.5222	5.404	7.9965	-265.499	0.199
24	F^-_{int} {1 0 0} F^-_{int} {1 1 1}	55°	0.667	0.65	5.3507	7.933	-236.256	0.178
26	F^-_{int} {1 0 0} F^-_{int} {0 0 3}	-	0.6892	0.7113	5.2311	7.8064	-272.684	0
27	F^-_{int} {1 1 1} F^-_{int} {-1-1-1}	180°	1.1992	1.2381	5.3091	7.8265	-69.314	0
30	F^-_{int} {1 1 1} F^-_{int} {0 0 3}	-	1.3416	1.3177	5.2122	7.7484	-36.42	0
28	F^-_{int} {1 1 1} F^-_{int} {1 1-1}		1.4898	1.4839	5.1087	7.6042	-67.163	0.795
29	F^-_{int} {1 1 1} F^-_{int} {1 1-1}		1.4866	1.5254	4.9909	7.4787	-21.15	0.149
31	Ca^{2+}_{vac} {1 1 0}		0	0	5.7421	8.3332	68.3	0.827
15	O^{2-}_{int} {1 0 0}		0	0	4.6252	6.2473	-10.387	0.002
05	O^{2-}_{sub} {$\frac{1}{2}\frac{1}{2}\frac{1}{2}$} O^{2-}_{int} {$-\frac{1}{2}-\frac{1}{2}-\frac{1}{2}$}	180°	0.1698	0.202	4.7498	6.185	-15.454	0
07	O^{2-}_{sub} {$\frac{1}{2}\frac{1}{2}\frac{1}{2}$} O^{2-}_{sub} {$\frac{1}{2}\frac{1}{2}-\frac{1}{2}$}		0.0254	0.0173	5.1767	6.702	-16.845	0.451
06	O^{2-}_{sub} {$\frac{1}{2}\frac{1}{2}\frac{1}{2}$} O^{2-}_{sub} {$-\frac{1}{2}-\frac{1}{2}-\frac{1}{2}$}		0	0	5.1517	6.6783	-18.412	0.016
09	O^{2-}_{sub} {$\frac{1}{2}\frac{1}{2}\frac{1}{2}$} F^-_{int} {1 0 0}	55°	0	0	5.277	7.0699	31.783	0.37
08	O^{2-}_{sub} {$\frac{1}{2}\frac{1}{2}\frac{1}{2}$} F^-_{int} {-1 0 0}	125°	0.0229	0.0409	5.3869	7.2237	-15.302	0.286
11	O^{2-}_{sub} {$\frac{1}{2}\frac{1}{2}\frac{1}{2}$} F^-_{int} {-1-1-1}	180°	0.2725	0.3134	5.5729	7.4465	-24.016	0
10	O^{2-}_{sub} {$\frac{1}{2}\frac{1}{2}\frac{1}{2}$} F^-_{int} {1 1 1}		0.3811	0.394	5.2473	7.0933	-33.851	0
12	O^{2-}_{sub} {$\frac{1}{2}\frac{1}{2}\frac{1}{2}$} F^-_{int} {1 1 1}		0.347	0.3948	5.6416	7.4455	-24.584	0.027
14	O^{2-}_{sub} {1 1 1} F^-_{int} {0 0 3}	-	0.3842	0.4337	5.5763	7.4858	-23.59	0
13	O^{2-}_{sub} {$\frac{1}{2}\frac{1}{2}\frac{1}{2}$} F^-_{int} {1 1-1}		0.4802	0.5017	5.5456	7.3925	-24.752	0.037
32	Na^+_{sub} {1 1 0} Na^+_{sub} {0-1-1}	120°	0	0	5.9998	8.6087	3.797	0.312
34	Na^+_{sub} {1 1 0} Na^+_{sub} {1-1 0}	90°	-0.0256	0.0233	6.0613	8.65	4.132	0.392
33	Na^+_{sub} {1 1 0} Na^+_{sub} {1 0 1}	60°	0.0935	0.1067	5.8376	8.4308	2.063	0.87
35	Na^+_{sub} {1 1 0} Na^+_{sub} {-1-1 0}	180°	0.1653	0.1496	5.7842	8.3977	4.132	0.98

Table 5.1.
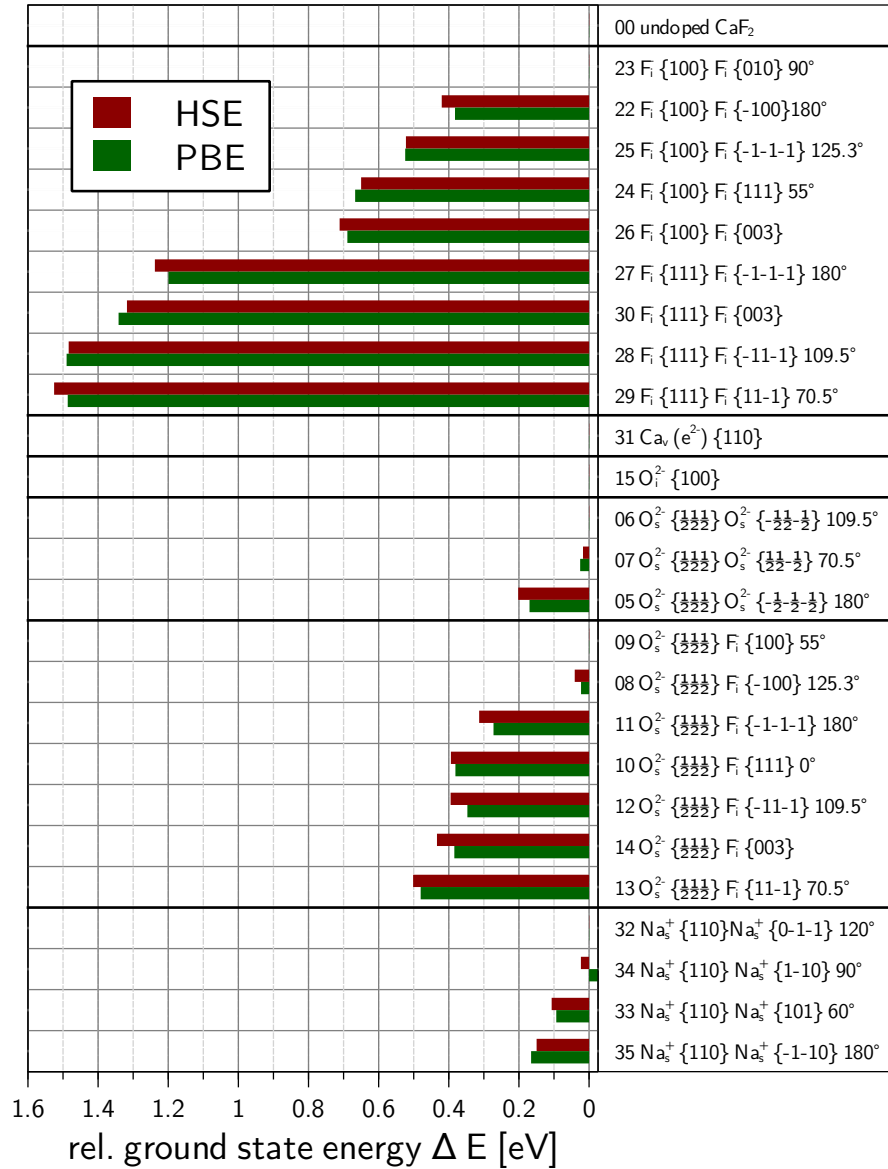
Figure 5.1.: The ground state energies relative to the lowest energy with the same stoichiometry and sorted by relevance. The groups with the same stoichiometry are separated by black lines. Red is the more accurate HSE calculation, blue the PBE calculation.
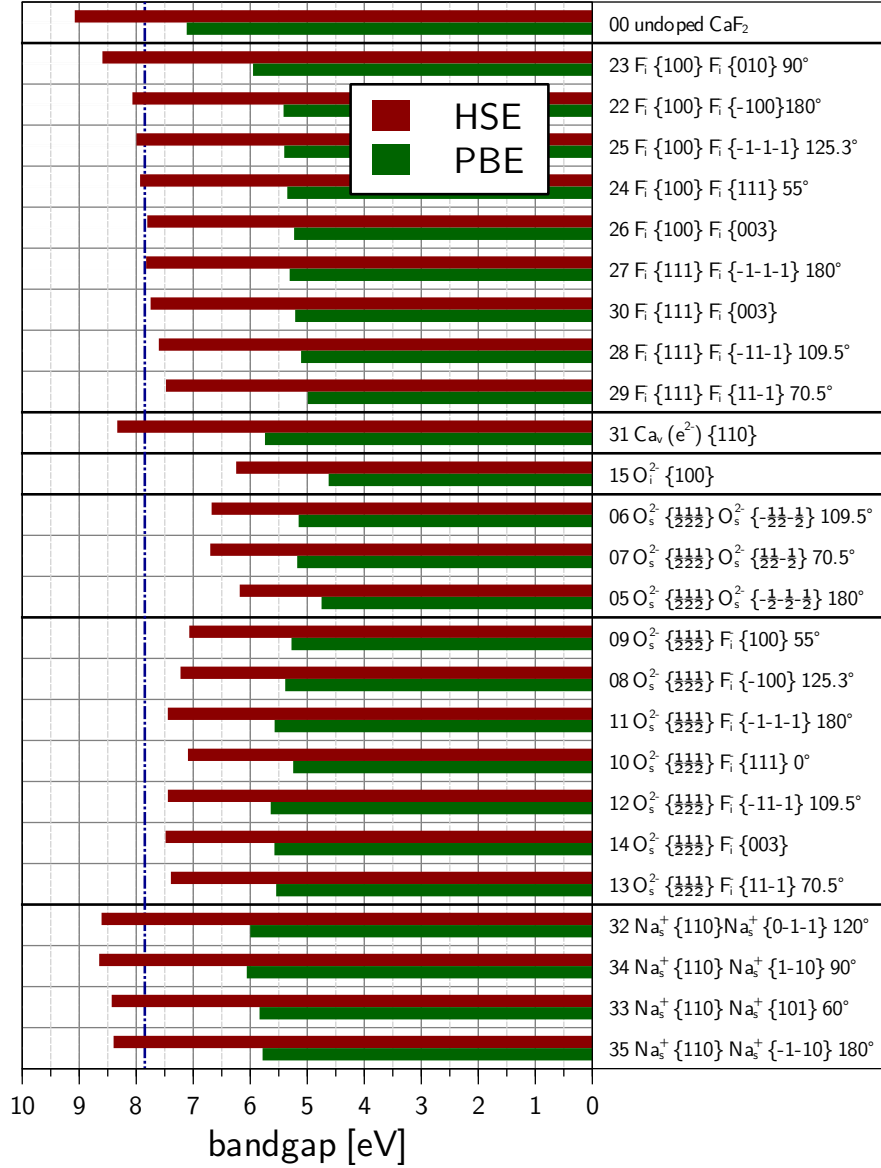
Figure 5.2.: The bandgap of the most relevant charge compensations in the same order and grouped by stoichiometry as in Figure 5.1. Red is the more accurate HSE calculation, blue the PBE calculation. The Th excitation energy of 7.8(5) eV is marked by the blue line (dash dot).

5.1. Two F interstitials 90°

The energetically most favourable charge compensation without any impurities or co-doping is the 90°two F interstitials (F{1 0 0}, F{0 1 0}) case (see Figure 5.3). It is very interesting that the 90°case has a lower ground state energy than the 180°variant (compare Figure 5.3). If the ionic crystal would be roughly approximated by numerous charged spheres, the 180°variant would be electrostatically favourable. Since the undisturbed lattice is in average neutral, only the extra charge of the Th and the two F interstitials would be taken into account. This is too simplified approach, which fails. The complex electrostatic interactions between the electrons and the nuclei need to be taken into account. If the extra charge and ions are compared to common molecules the result is not so surprising.

The 90°configuration lowers the symmetry of the crystal and leads to energy gains by Jahn Teller type mechanism. While the electrostatic energy is almost the same for the 180°and 90°configuration the J-T effect makes the 90°interstitials more favourable.

The density of states is shown in Figure 5.4. The states of the additional F ions are found at the bottom of the gap while the emptied Th_4^+ states are located at the top of the gap. This leaves a gap of at leas $8.59\,eV$ sufficiently large for the desired exitation of $7.8(5)\,eV$. It should be noted that for these large gap insulators even HSE slightly underestimates the true gap size so that the real gap will probably be even larger.

Replacing one calcium ion by a thorium and introducing compensation charges causes a relaxation of the ionic positions inside the lattice. The forces acting on the respective ions are shown in Figure 5.5. We find that Th and the two F compensation charges move together while the adjacent F ions of F sublattice move away from the compensation charges. These fetaures can also be seen in the electronic charge density Figure 5.6 5.7 where the formation of the $Th(F_{int})_2$ complex is clearly visible.
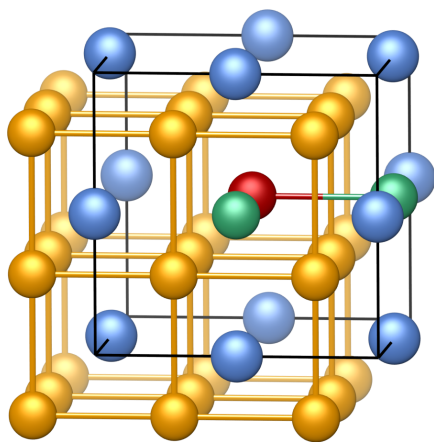
(a) F 90°: The structure of the most prob-able charge compensation with two F interstitials at 90° is shown.
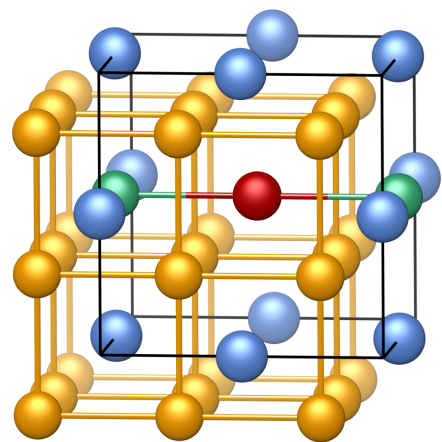
(b) F 180°: Is the picture of the F interstitials at 180° which was the expected result.

Figure 5.3.: Comparison of two possible charge compensations.
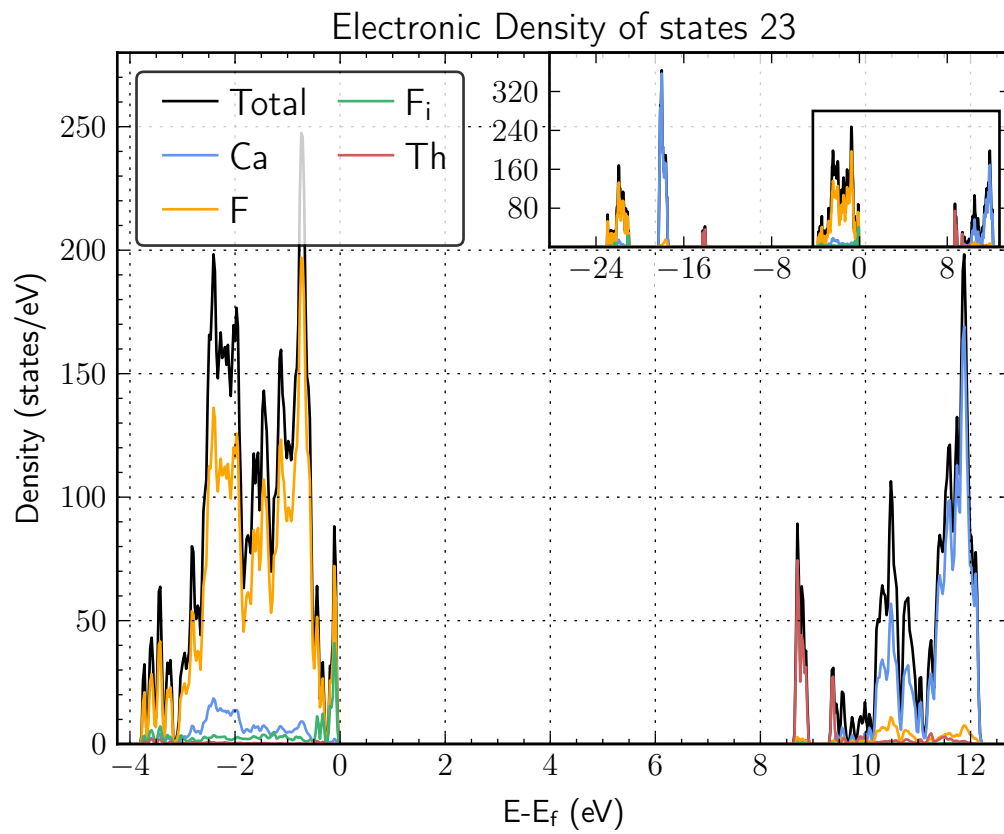
Figure 5.4.: The electronic density of states of the most probable charge compensation with two F interstitials at 90°.
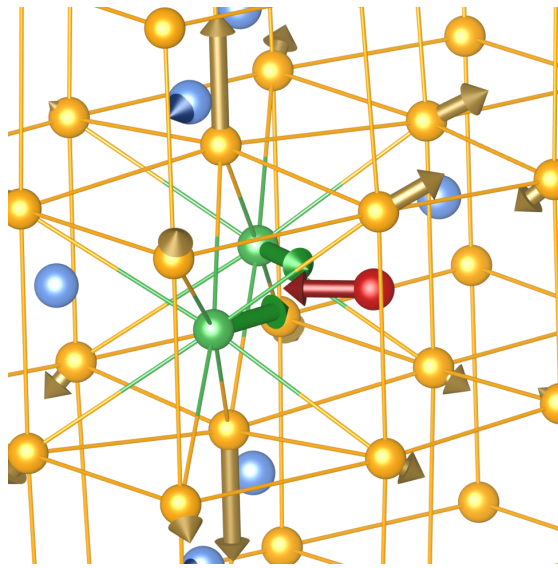
Figure 5.5.: Schematic view of the forces acting on the atoms in Th-doped CaF_2 in the 90°F interstitial charge-compensated case: Th (red), F(yellow), F_i^- charge compensation (green), Ca (blue). The arrows point in the direction of deformation and the length of the arrow is proportional to the force. The relaxations are of the order of 5-10% of the bond length.
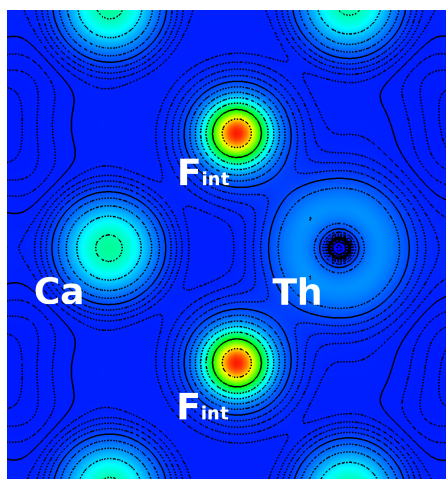
Figure 5.6.: Calculated charge density for the 90°F-interstitials in the (110) plane, intersecting Th and the two compensation charges. The Thorium substitute and the two fluor interstitials 90 degrees are clearly visible
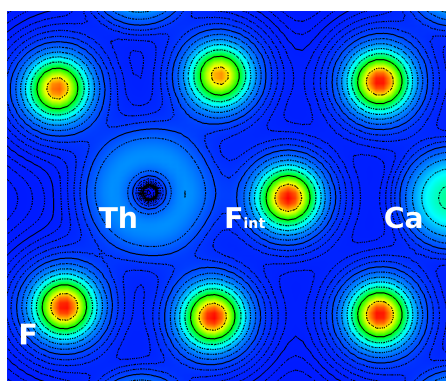
Figure 5.7.: Charge Density of calculation 23 (2 F interstitials 90 degrees) Cubic F lattice visible. Charge density for a plane intersecting Th and one of the compensation charges $(01\bar{1})$ (normal to the plane in Figure 5.6)

5.2. Calcium vaccancy

In the Th doped crystal a Ca vacancy is another possible charge compensation. Since the Th is in the center of the conventional unit cell shown in Figure 5.8 all nearest Ca atoms are symmetrically equivalent. Therefore only one calculation had to be computed. In Figure 5.9 the electronic density of states is shown. The empty Th states sit on the top of the gap and reduce the gap size to $8.33\,\text{eV}$. This is almost the same size than in the two F interstitial case and larger than the Th excitation.

Energetically we cannot discriminate between the present case and the case with two additional F ions, however, experimentally it seems that the formation of an additional Ca vacancy is less probable.
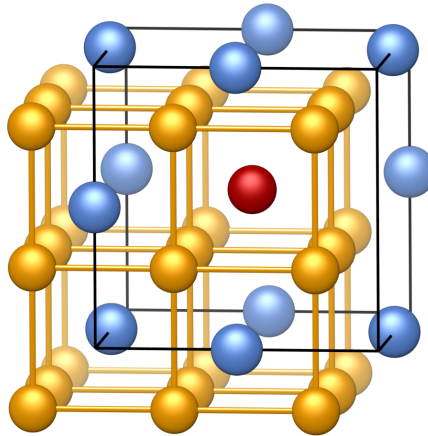
Figure 5.8.: The structure of CaF_2 doped with Th_{sub}^{4+} and Ca_{vac}^{2+} {1 1 0}.
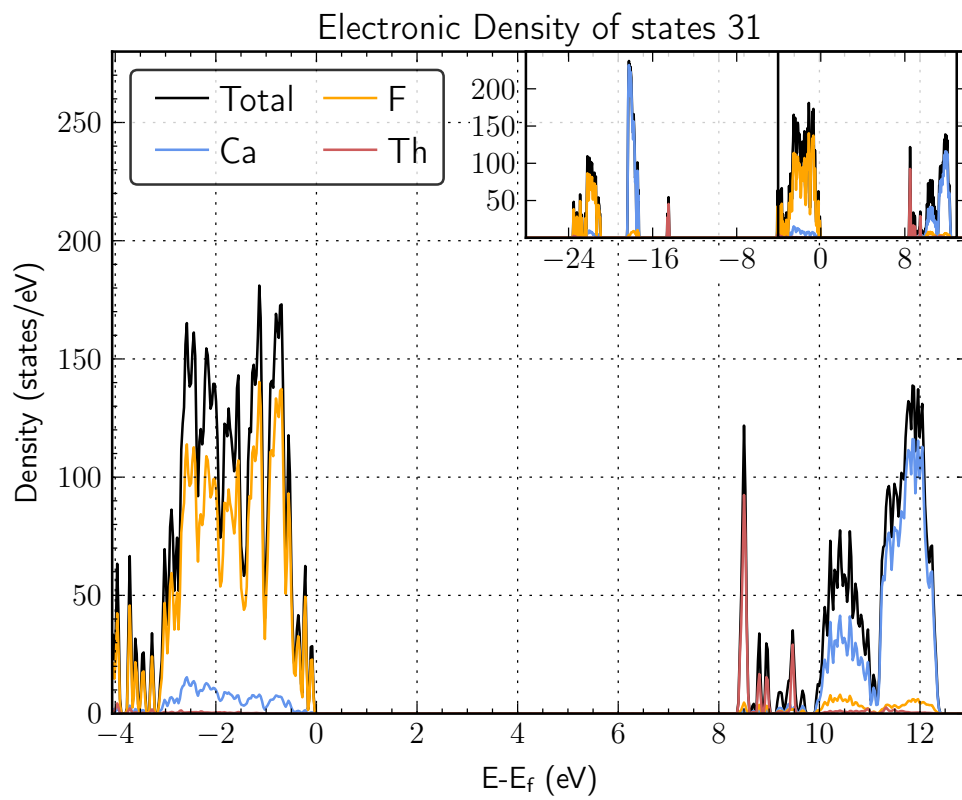
Figure 5.9.: The electronic density of states of a Calcium vacancy.

5.3. Oxygen

There are several possible charge compensations including oxygen. The cases studied here can be found in Table 5.1 and are: oxygen on an interstitial position (case 15), 2 oxygen replacing 2 F ions (cases 5,6,7), 1 oxygen plus 1 fluorine at an interstitial position (cases 8-14). All these cases have in common that the oxygen states ly inside the insulating gap and thus lead to a considerable reduction of the gap, an effect which is unfavourable for the present application. Completely independent of possible energetical considerations our results suggests that the presents of oxygen either as a substitute or as an interstitial must be avoided. As an example we show the density of states an oxygen interstitial {100} Figure 5.11 where the oxygen states near the middle of the gap are clearly visible. The actual gap size is now reduced to 6.25 eV
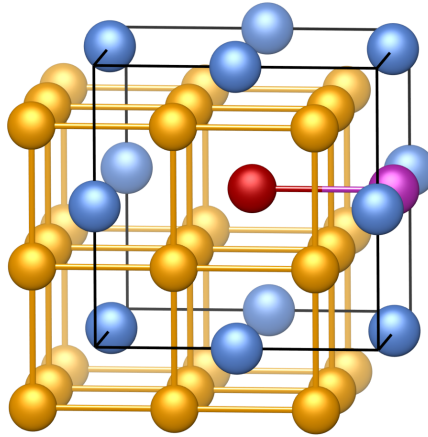
Figure 5.10.: The structure with an oxygen interstitial.
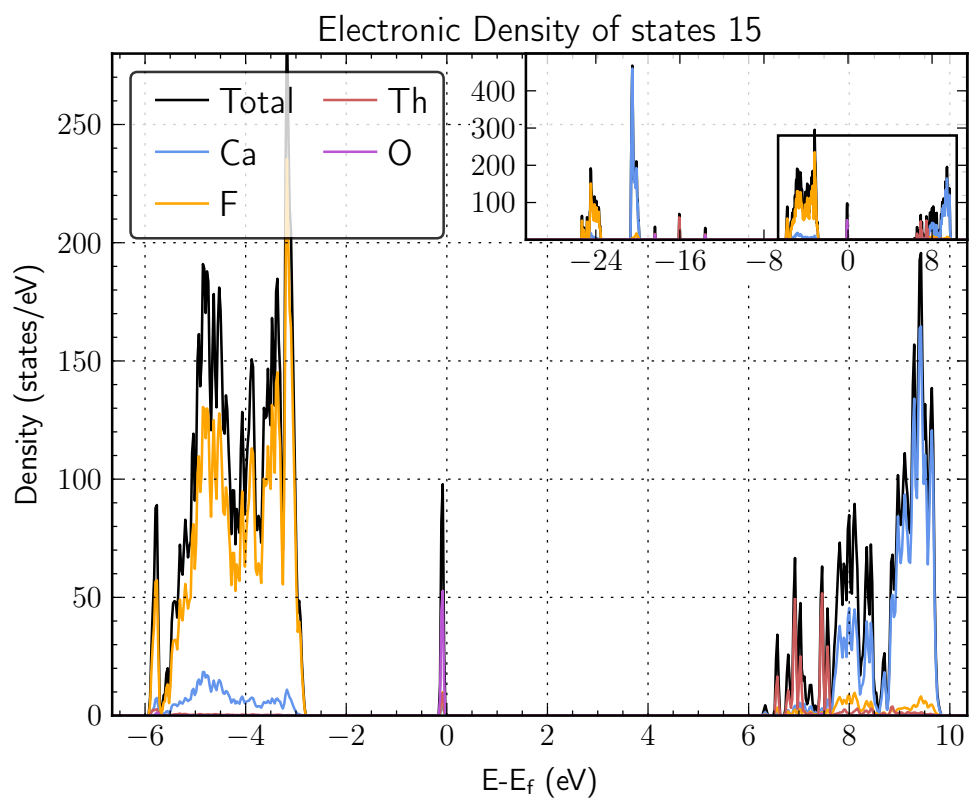
Figure 5.11.: The electronic density of states of oxygen substitute.

5.4. Sodium

Sodium is a common constituent in CaF_2 so that several paper study co-doping with NaF [70, 71]. It has been reported that a Na substitute is more likely to be compensated by a F vacancy than a Na interstitial [38]. It also has to be considered that Na as an electro positive element unlikely replaces an highly electronegative element like F which makes Na on interstitial positions more likely. A more detailed discussion is given in subsection 3.5.2. The case discussed here is two Na ions substituting for two Ca Figure 5.12. Out of the four variants calculated cases 32-35 in Table 5.1 the arrangement of Na at an angle of 120°is the energetically most favourable. However, all 4 cases retain a bandgap larger than 8.4 eV comparable to the F case discussed before. The respective density of states is given in Figure 5.13. Since Na is in a completely ionised Na^+ state the unoccupied 3s state sits far above the gap inside the Ca manifold.
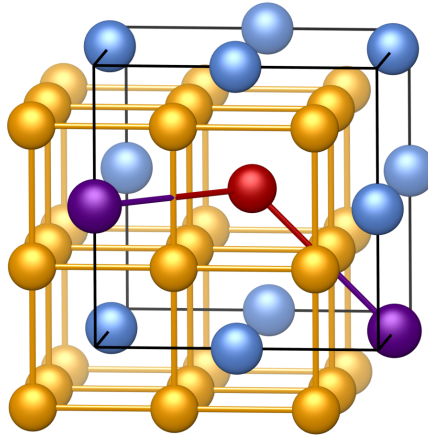
Figure 5.12.: The structure with an sodium substitute on an calcium site.
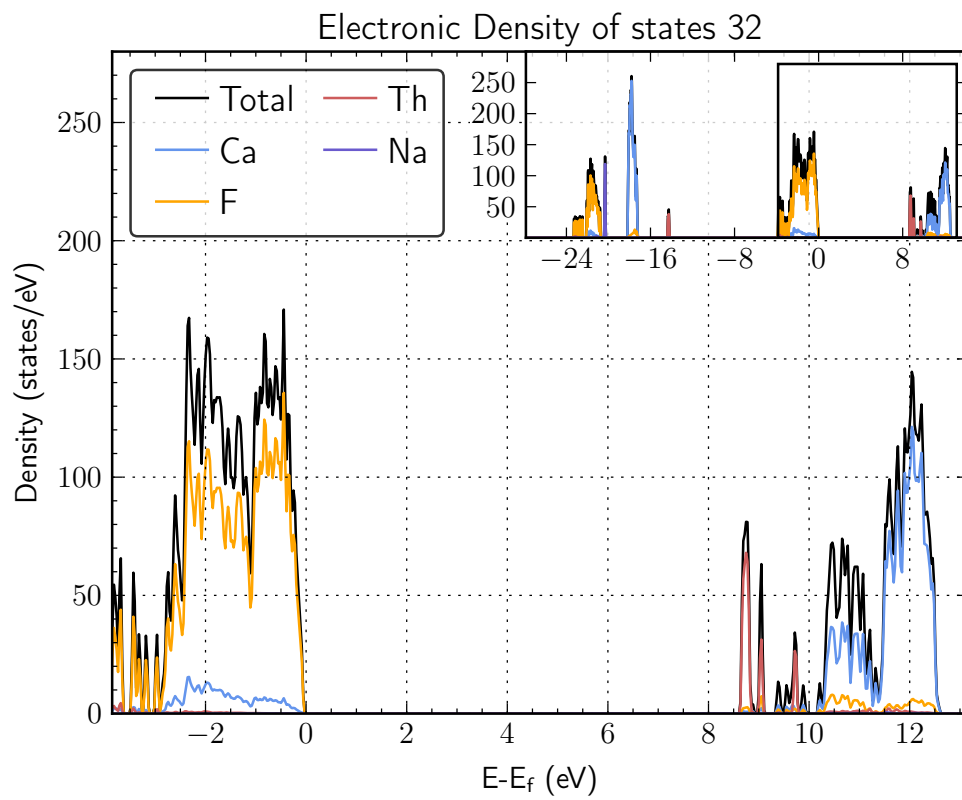
Figure 5.13.: The electronic density of states of sodium substitute.

5.5. Electric field gradient (EFG)

A splitting of the nuclear energy levels is introduced by the interaction of the nuclear quadrupole moment Q and the gradient of the electric charge distribution (EFG). This can help to identify the exact environment of the Thorium isotope [20]. The electric field gradient is computed by VASP using the method of Petrilli et al. [69]. The electric field gradient V_{ij} is a traceless symmetric tensor which can be diagonalized [57]. The axis of of the tensor is usually chosen that $|V_{zz}| > |V_{xx}| > |V_{yy}|$. Only V_{zz} and the asymmetry parameter η are required to describe the system.

$$\eta = \frac{|V_{xx} - V_{yy}|}{|V_{zz}|} \tag{5.1}$$

The energy splitting is

$$E_Q = \frac{eQV_{zz}[3m_I^2 - I(I+1)](1 + \eta^2/3)^{\frac{1}{2}}}{4I(2I-1)} \tag{5.2}$$

where I is the nuclear spin and m_I is the respective magnetic quantum number.

The calculated valus of V_{zz} and η are given in Table 5.1 and shown in Figure 5.14. It can be seen that the charge compensation with two F interstitials in the nearest neighbour site $\langle 001 \rangle$ (empty F-cube) has a much larger EFG V_{zz} independent of the angle between the interstitials (max. $297\,\mathrm{V\,\AA}^{-2}$). The field gradient for F-interstitials in the next nearest neighbour site $\langle 111 \rangle$ is already much lower (max. $69\,\mathrm{V\,\AA}^{-2}$) and of similar size as for the Ca vacancy. All charge compensations with oxygen impurities a have a further reduced EFG ($34\,\mathrm{V\,\AA}^{-2}$ to $10\,\mathrm{V\,\AA}^{-2}$). As expected the lowest EFG is found using Na co-doping ($4.1\,\mathrm{V\,\AA}^{-2}$). This is because the Na substitutes sit on next nearest neighbour Ca sites $\langle 110 \rangle$ and the symmetry of the nearest neighbours remains approximately cubic. Note that only combinations of Na substitutes were computed with the expected smallest EFG and not all other possible combinations with e.g. F^- interstitials or O^{2-} substitutes.

Although oxygen impurities and even more sodium co-doping would reduce the electric field gradient, many different additional combinations of charge compensations would be possible. This would complicate the identification of the most dominant energy splitting and yield numerous close energy states. In this sense it will be recommended to avoid any impurities and co-doping.
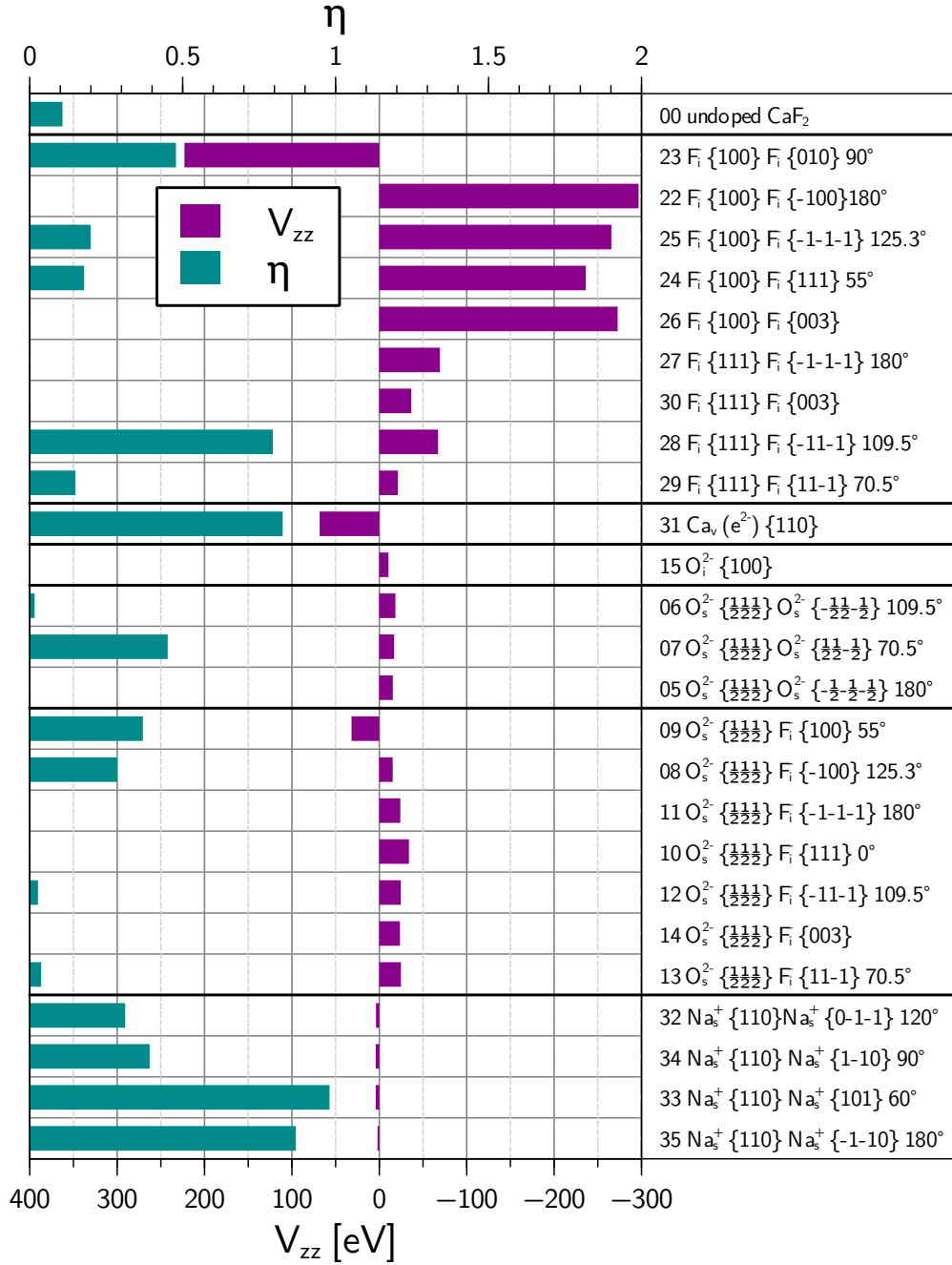
Figure 5.14.: The electric field gradient of the most relevant charge compensations in the same order and grouped by stoichiometry as in Figure 5.1. Magenta is V_{zz}, the largest component of the diagionalized EFG-Tensor. In Cyan is the asymmetry parameter η.

5.6. No charge compensation and charged crystal

Because of the large amount of calculated cases, only the most realistic variants were included in the previous discussion. Nevertheless the partial density of state plots of all variants are included in Appendix A and the missing data of Table 5.1 are now given in Table 5.2. It can be seen there that if one or two charge compensations are missing the material becomes metallic (PBE) or an insulator (HSE) with a small bandgap (less than $1\,\mathrm{eV}$). In both cases the doped crystal would not remain transparent in the UV-region. This is not what happened in the experiments. This prooves that some charge compensation mechanism is active in the doped crystal. The calculated cases without (sufficient) charge compensation can be ignored.

In the case of a charged crystal (2 holes e^{2+}) (or an further away charge compensation), the band gap is only slightly reduced $8.93\,\mathrm{eV}$. In the combination of one charge compensation (e.g. F $\langle 001\rangle$) and a single charged crystal (e^{+}) the bandgap is slightly larger than the in the case of two charge compensations. A further away charge compensation would not change the bandgap very much.

No.	Charge Compen.		Energy [eV]		Bandgap [eV]		HSE EFG	
			PBE	HSE	PBE	HSE	$V_{zz}[\mathrm{V/\mathring{A}}^2]$	η
01	e^{+}	e^{+}	-13.0768	-14.8826	6.3268	8.9343	-0.013	0.622
02	none	none	-0.4345	-2.3028	0	0.8254	0.011	0.936
03	$\mathrm{O}^{2-}_{\mathrm{sub}}\ \{\frac{1}{2}\frac{1}{2}\frac{1}{2}\}$	e^{+}	-11.7263	-13.7269	5.6863	7.3905	-24.691	0
04	$\mathrm{O}^{2-}_{\mathrm{sub}}\ \{\frac{1}{2}\frac{1}{2}\frac{1}{2}\}$	none	-5.2557	-6.8895	0	0.1578	-26.726	0
16	$\mathrm{F}^{-}_{\mathrm{int}}\ \{100\}$	e^{+}	-14.7544	-20.0745	6.0567	8.7418	-228.33	0
17	$\mathrm{F}^{-}_{\mathrm{int}}\ \{111\}$	e^{+}	-14.0076	-19.3488	5.2108	7.7356	-34.348	0
18	$\mathrm{F}^{-}_{\mathrm{int}}\ \{003\}$	e^{+}	-13.9893	-19.2975	5.0942	7.625	0.003	0.617
19	$\mathrm{F}^{-}_{\mathrm{int}}\ \{100\}$	none	-8.4247	-13.5724	0.1444	0.8782	-296.051	0
20	$\mathrm{F}^{-}_{\mathrm{int}}\ \{111\}$	none	-7.8148	-13.0207	0	0.8535	-30.185	0.001
21	$\mathrm{F}^{-}_{\mathrm{int}}\ \{003\}$	none	-7.696	-12.8485	0	0.5394	-0.113	0.647

Table 5.2.: Results of the calculations with no charge compensations and charged crystal.

6. Conclusion and suggestions for further work

Several different configurations of Th doped CaF_2 were studied. The most likely configuration are the case with two F interstitials is the 90°and the Ca vacancy.

A bandgap larger than 7.8(5) eV is necessary for Th:CaF_2 to remain transparent. The bandgap is known to be underestimated by density functional theory. Even post DFT hybrid functionals like HSE underestimate the bandgap for large gap insulators. Our computed bandgaps of pure CaF_2 are lower than the experimental data. It is expected that the impurity bands within the gap are also shifted to lower energies. The computed values are a reliable lowest boundary for the real gap. The lowest energy configurations with 2 F interstitials are above 7.8(5) eV and the rest is only slightly lower (min bandgap 7.48 eV). The bandgap of the Ca vacancy is eV Oxygen impurities have impurity bands in the middle of the gap and lower band gaps (6.25 eV, 6.68 eV, 7.07 eV) and should be avoided. The studied Na impurities have an even larger bandgap than without any co-doping and are therefore not problematic. As a general trend we observe that electro positive elements like Na do not influence the bandgap since their empty states are positioned above the upper band edge. For strongly electro negative elements like F the opposite trend is found, namely their occupied states sit at the bottom of the gap. Problematic are only elements with intermediate electro negativity like oxygen which form new states inside the gap. From these considerations we also conclude that elements like S, N, C will be unfavourable for charge compensation in the present application. Sodium on the other hand as shown in experiment has a tendency to stabilize colour-centers which could also jeopardize the application as an atomic clock.

The splitting of the nuclear energy levels caused by the electric field gradient could be used to experimentally verify which charge compensation is present in Th:CaF_2.

In general the results are in good agreement with the atomistic modelling calculations of Robert A. Jackson using the GULP code (see Ref. [20]).

A. Data

On the following pages the relaxed crystall structure of all charge compensations is shown. Although in the calculation a supercell (3^3 primitive unit cells) was used, for simplicity the conventional unit cell is used. Below the unit cell is the partial density of states of the charge compensation.
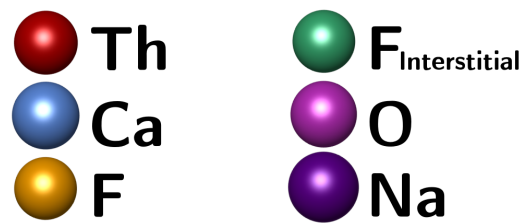
Figure A.1.: This is the colour scheme for all kind of ions in the thesis and the following structures.

A.1. Structures and DOS

0. undoped CaF$_2$
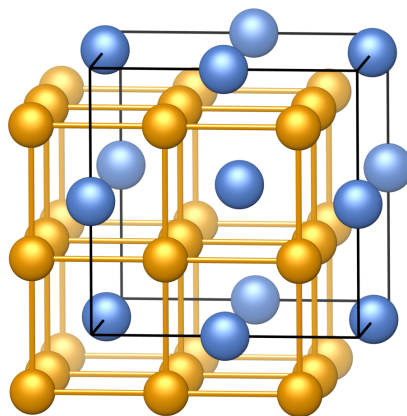
The structure of undoped CaF$_2$.
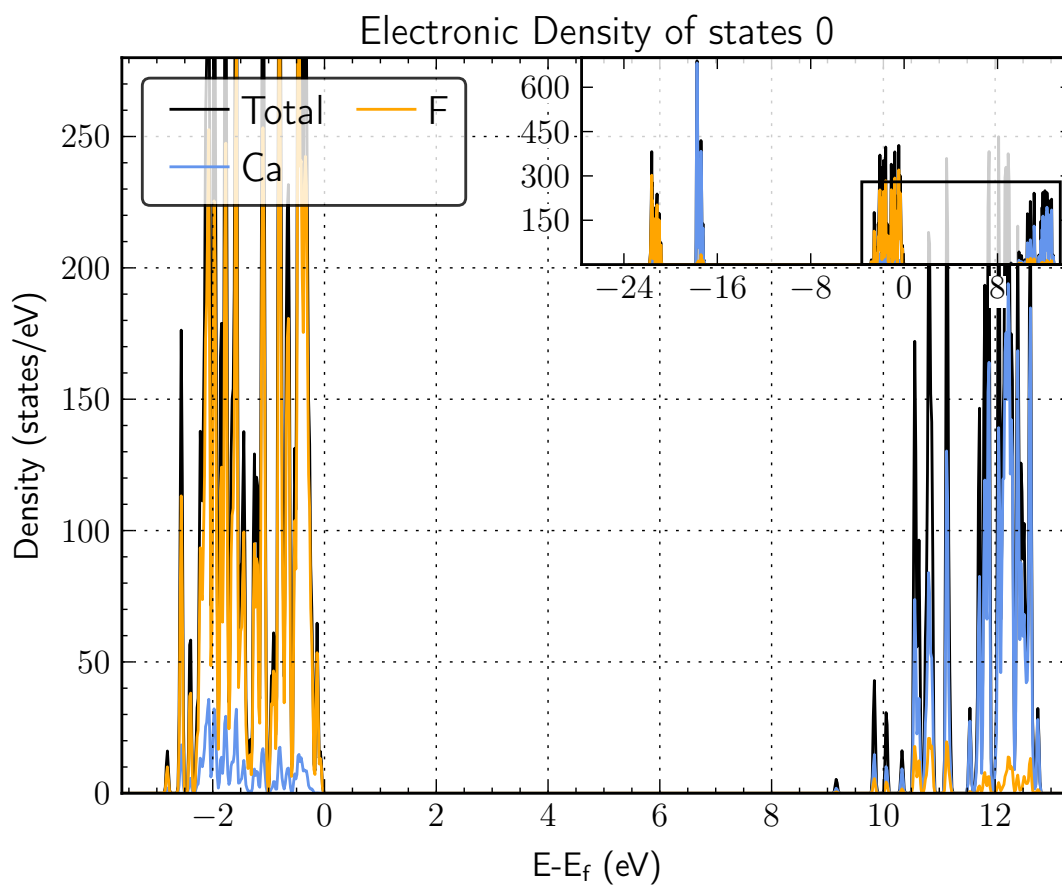
1. Th_{sub}^{4+} & 2 holes (2x e^+)
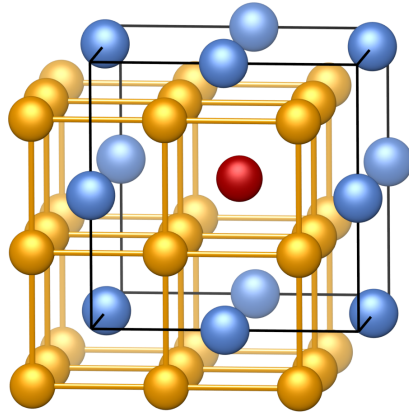
The structure of CaF_2 doped with Th_{sub}^{4+} and 2 holes (2x e^+).
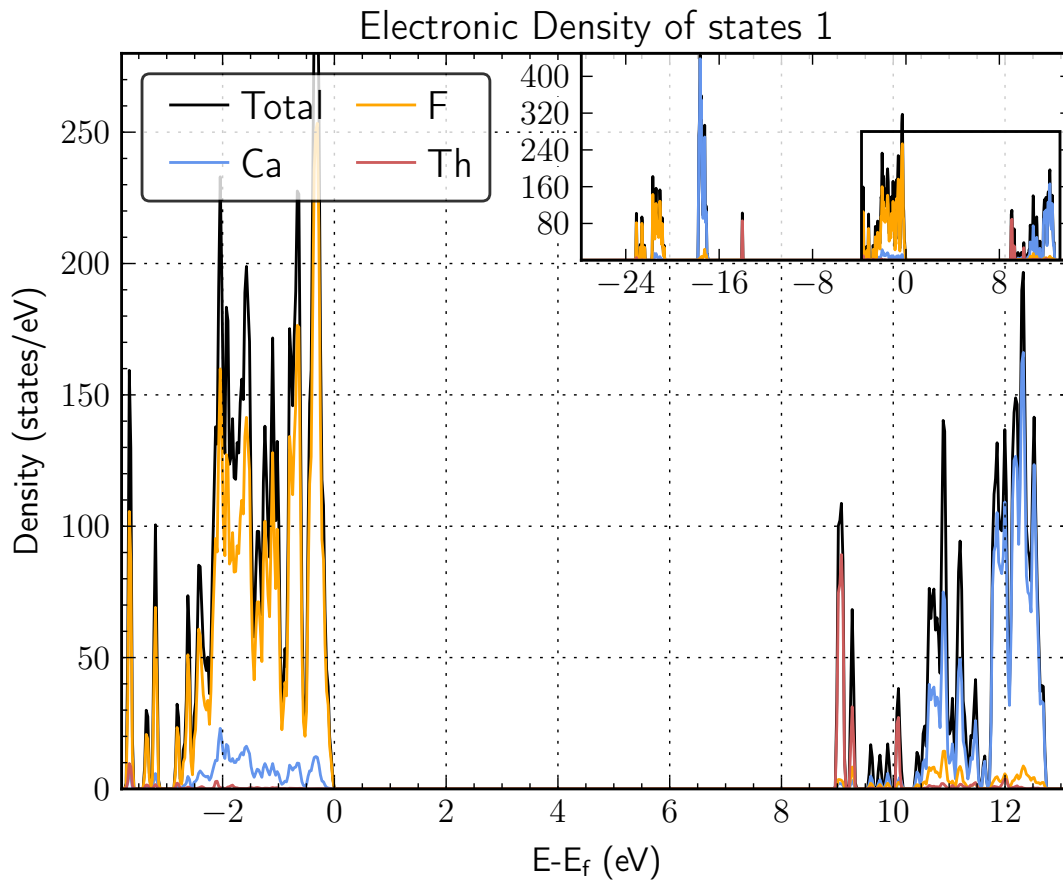
2. Th$_{sub}^{4+}$ & 2x no charge compensation
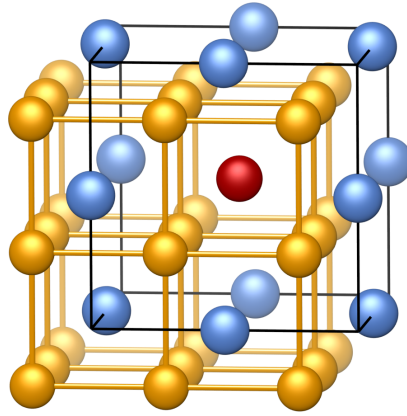
The structure of CaF_2 doped with Th$_{sub}^{4+}$ and 2x no charge compensation.
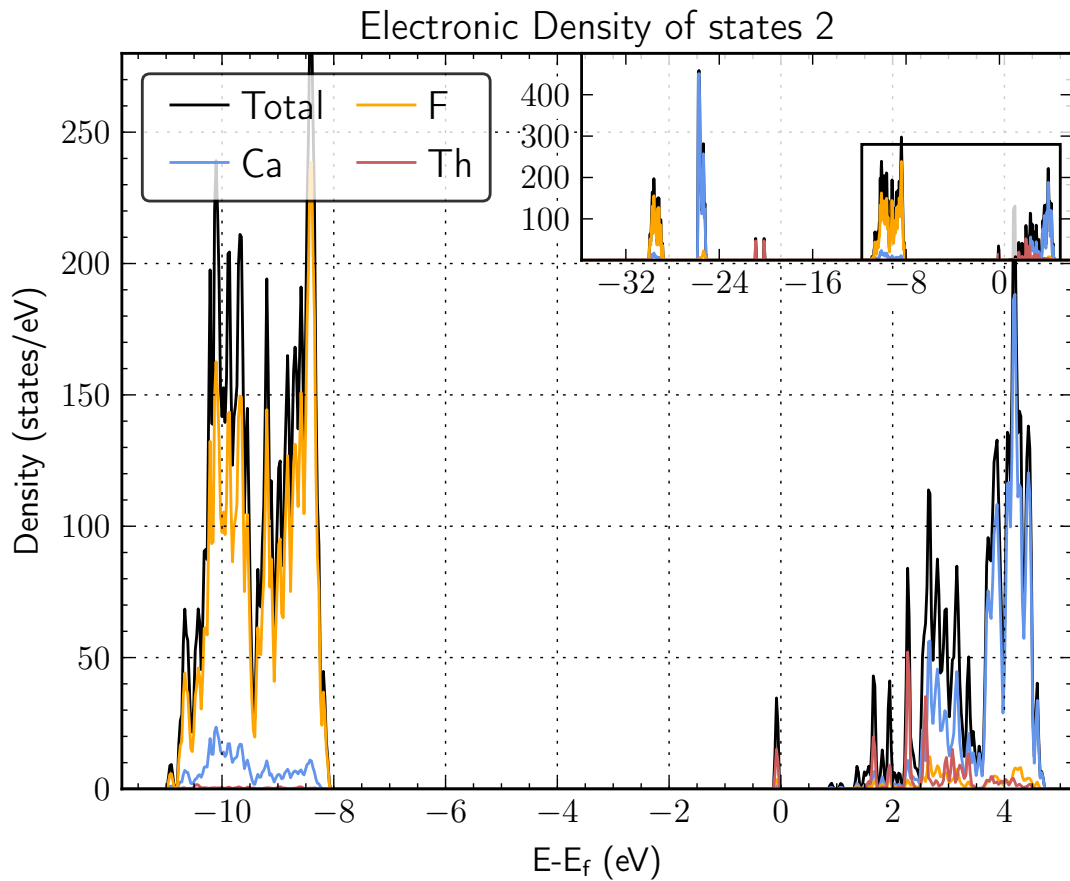
3. Th^{4+}_{sub} & O^{2-}_{sub} $\left\{ \frac{1}{2} \ \frac{1}{2} \ \frac{1}{2} \right\}$ & hole (e^+)
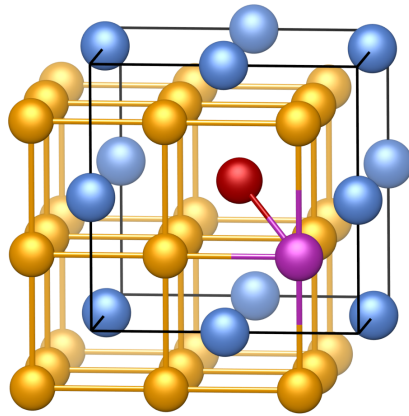
The structure of CaF_2 doped with Th^{4+}_{sub} and O^{2-}_{sub} $\{\frac{1}{2} \ \frac{1}{2} \ \frac{1}{2}\}$ and hole (e^+).
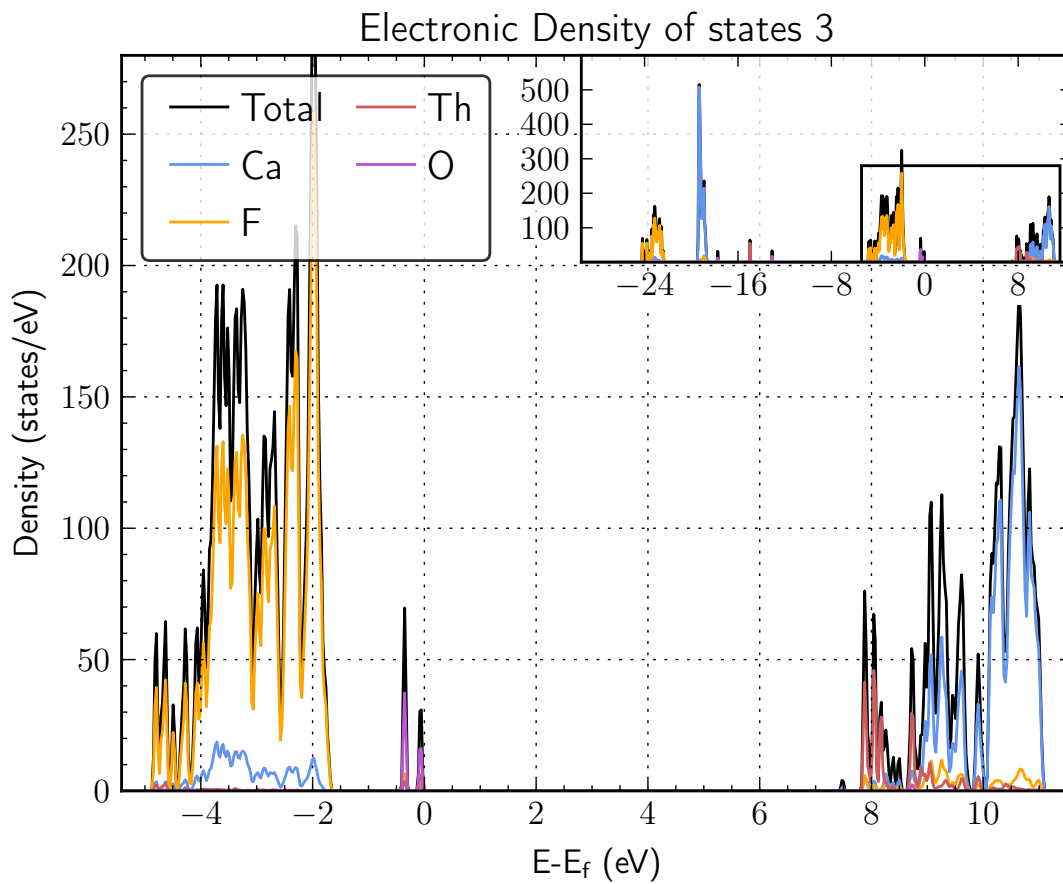
4. Th$_{\text{sub}}^{4+}$ & O$_{\text{sub}}^{2-}$ $\left\{\frac{1}{2}\ \frac{1}{2}\ \frac{1}{2}\right\}$ & 1x no charge compensation
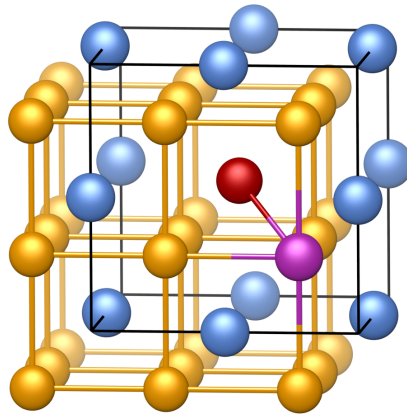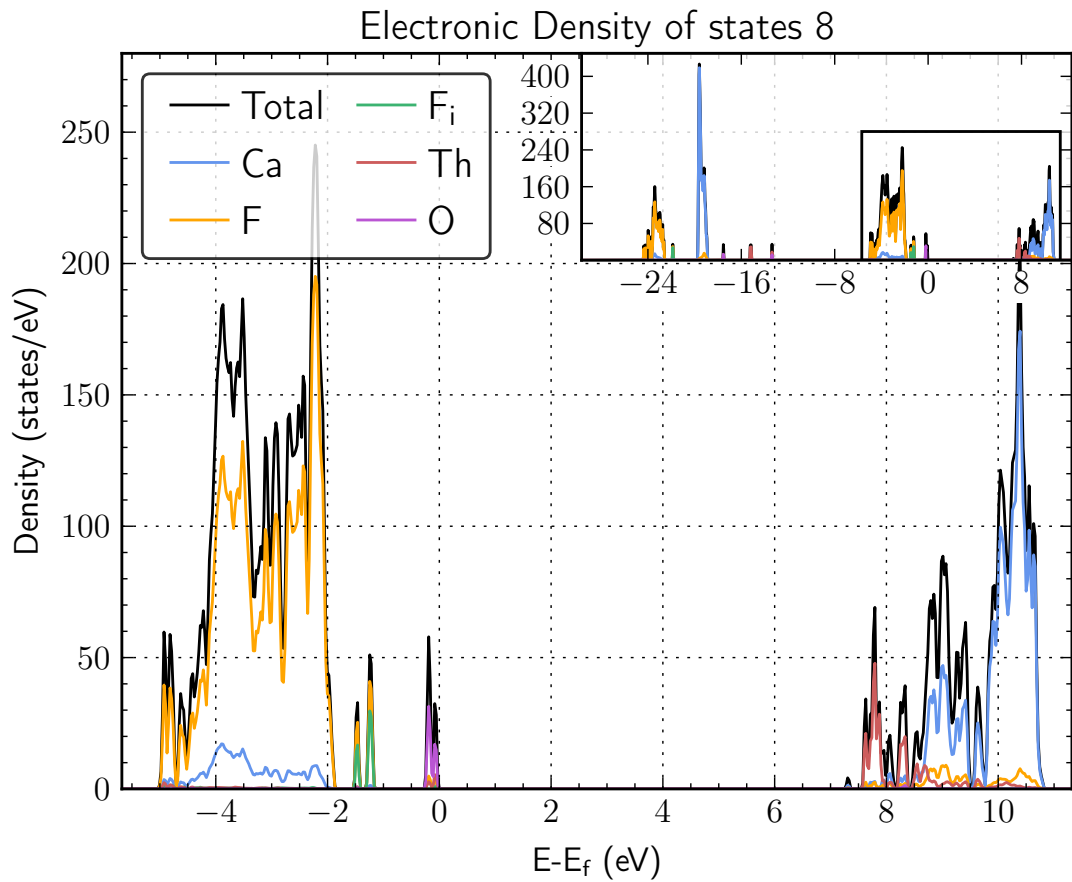

The structure of CaF$_2$ doped with Th$_{\text{sub}}^{4+}$ and O$_{\text{sub}}^{2-}$ $\{\frac{1}{2}\ \frac{1}{2}\ \frac{1}{2}\}$ and 1x no charge compensation.

5. Th^{4+}_{sub} & O^{2-}_{sub} $\left\{\frac{1}{2} \ \frac{1}{2} \ \frac{1}{2}\right\}$ & O^{2-}_{sub} $\left\{-\frac{1}{2}-\frac{1}{2}-\frac{1}{2}\right\}$ at 180°
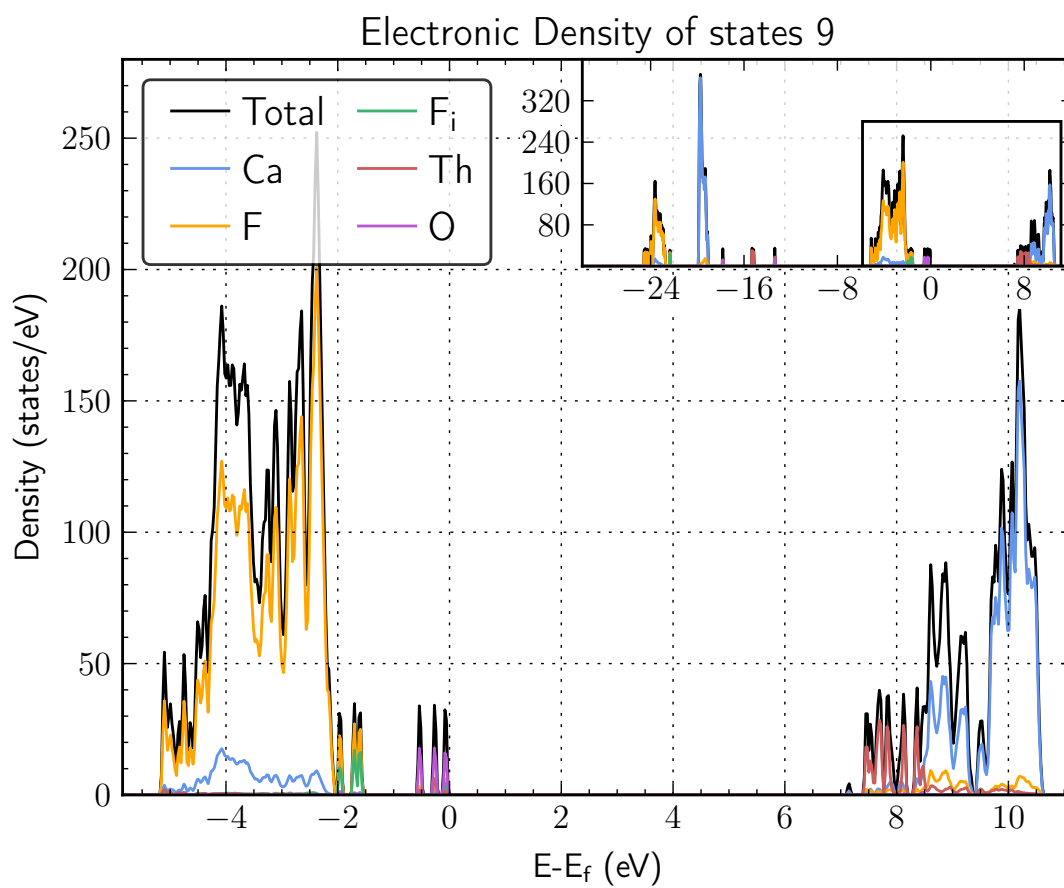

The structure of CaF_2 doped with Th^{4+}_{sub} and O^{2-}_{sub} $\left\{\frac{1}{2} \ \frac{1}{2} \ \frac{1}{2}\right\}$ and O^{2-}_{sub} $\left\{-\frac{1}{2}-\frac{1}{2}-\frac{1}{2}\right\}$ at 180°.

6. Th^{4+}_{sub} & O^{2-}_{sub} $\{\frac{1}{2} \frac{1}{2} \frac{1}{2}\}$ & O^{2-}_{sub} $\{-\frac{1}{2} \frac{1}{2}-\frac{1}{2}\}$ at 109.5°

The structure of CaF_2 doped with Th^{4+}_{sub} and O^{2-}_{sub} $\{\frac{1}{2} \frac{1}{2} \frac{1}{2}\}$ and O^{2-}_{sub} $\{-\frac{1}{2} \frac{1}{2}-\frac{1}{2}\}$ at 109.5°.
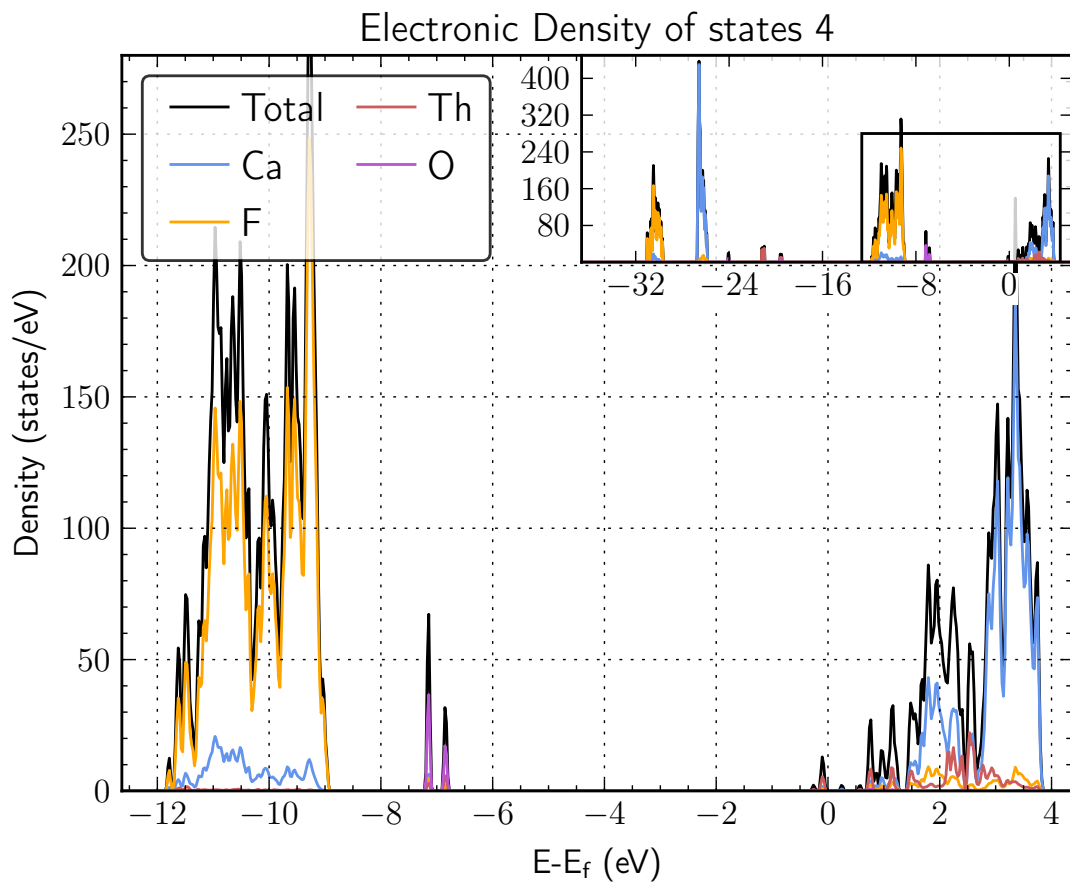
7. Th_{sub}^{4+} & O_{sub}^{2-} $\left\{\frac{1}{2} \ \frac{1}{2} \ \frac{1}{2}\right\}$ & O_{sub}^{2-} $\left\{\frac{1}{2} \ \frac{1}{2} \ \text{-}\frac{1}{2}\right\}$ at 70.5°
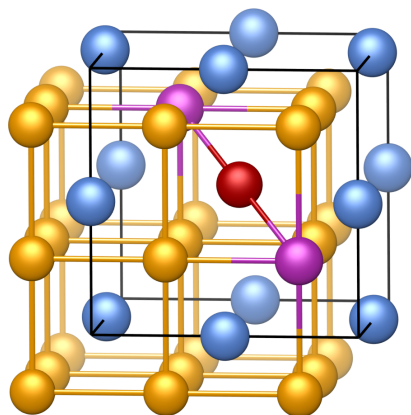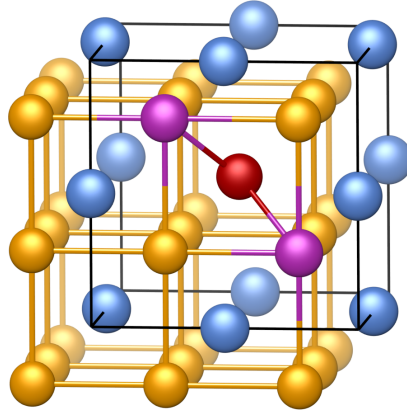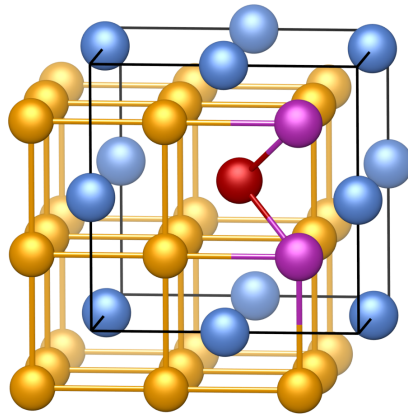
The structure of CaF_2 doped with Th_{sub}^{4+} and O_{sub}^{2-} $\{\frac{1}{2} \ \frac{1}{2} \ \frac{1}{2}\}$ and O_{sub}^{2-} $\{\frac{1}{2} \ \frac{1}{2} \text{-}\frac{1}{2}\}$ at 70.5°.

Electronic Density of states 7
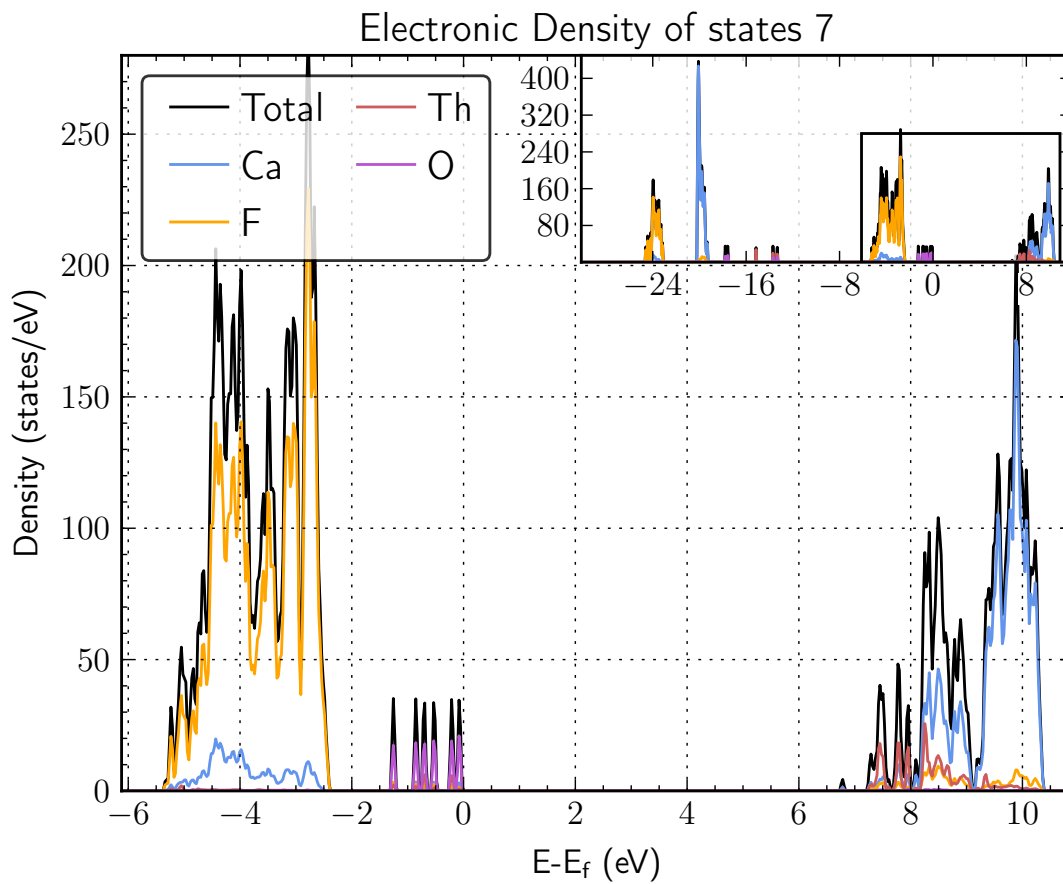
8. Th^{4+}_{sub} & O^{2-}_{sub} $\left\{\frac{1}{2} \ \frac{1}{2} \ \frac{1}{2}\right\}$ & F^-_{int} $\{-1 \ 0 \ 0\}$ at $125°$
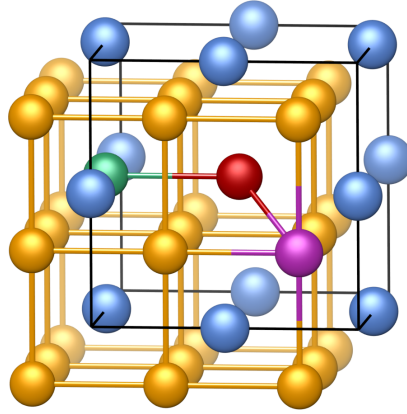
The structure of CaF_2 doped with Th^{4+}_{sub} and O^{2-}_{sub} $\left\{\frac{1}{2} \ \frac{1}{2} \ \frac{1}{2}\right\}$ and F^-_{int} $\{-1 \ 0 \ 0\}$ at $125°$.

9. Th_{sub}^{4+} & O_{sub}^{2-} $\left\{\frac{1}{2} \frac{1}{2} \frac{1}{2}\right\}$ & F_{int}^{-} $\left\{1\ 0\ 0\right\}$ at 55°
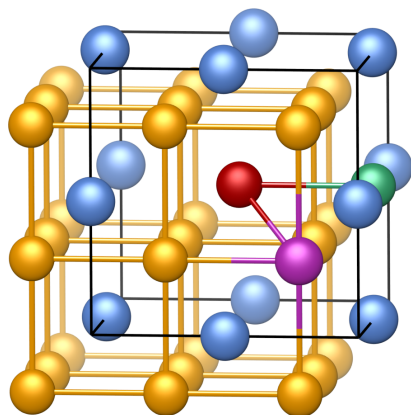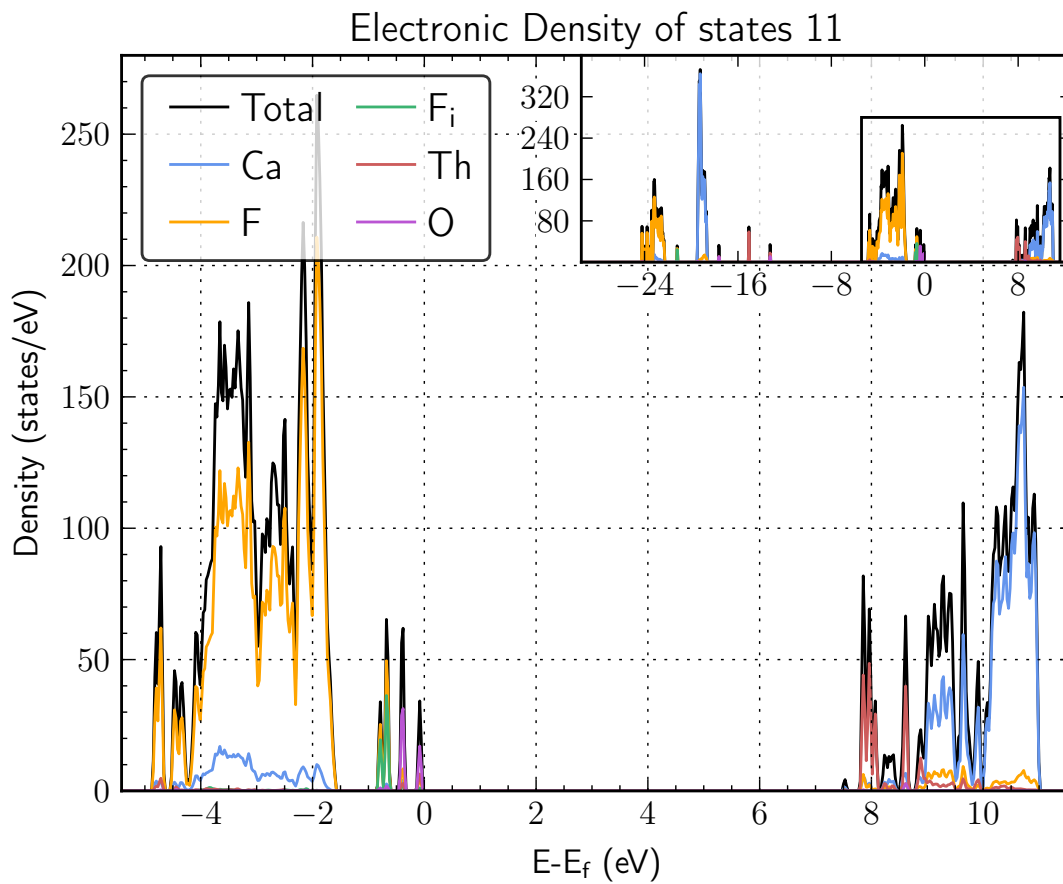

The structure of CaF_2 doped with Th_{sub}^{4+} and O_{sub}^{2-} $\left\{\frac{1}{2} \frac{1}{2} \frac{1}{2}\right\}$ and F_{int}^{-} $\{1\ 0\ 0\}$ at 55°.

10. Th_{sub}^{4+} & O_{sub}^{2-} $\left\{\frac{1}{2}\ \frac{1}{2}\ \frac{1}{2}\right\}$ & F_{int}^{-} $\{1\ 1\ 1\}$ at $0°$
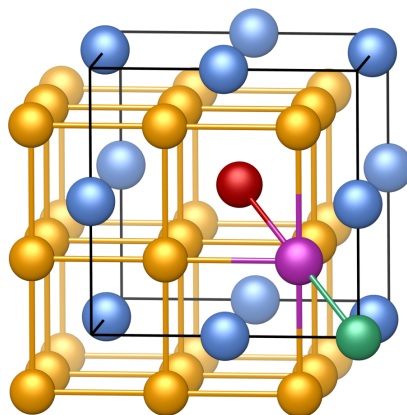
The structure of CaF_2 doped with Th_{sub}^{4+} and O_{sub}^{2-} $\left\{\frac{1}{2}\ \frac{1}{2}\ \frac{1}{2}\right\}$ and F_{int}^{-} $\{1\ 1\ 1\}$ at $0°$.
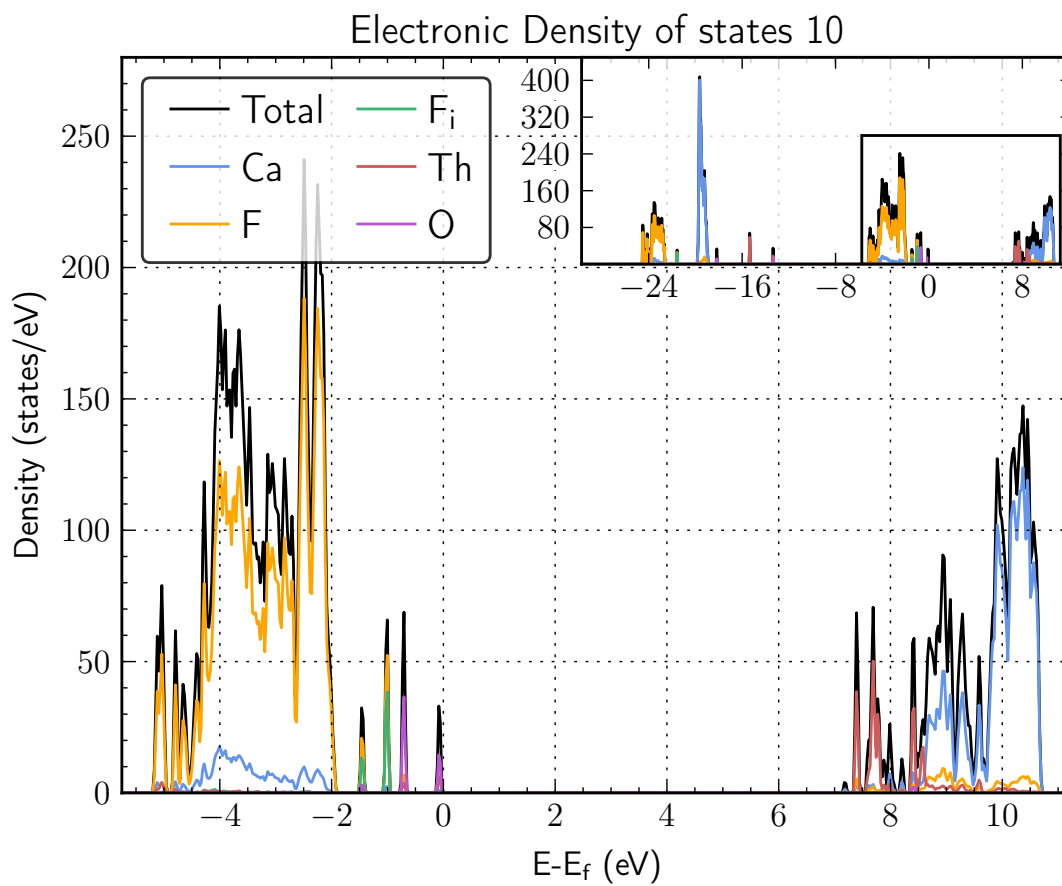
11. Th_{sub}^{4+} & O_{sub}^{2-} $\left\{\frac{1}{2}\ \frac{1}{2}\ \frac{1}{2}\right\}$ & F_{int}^{-} $\{$-1-1-1$\}$ at 180°
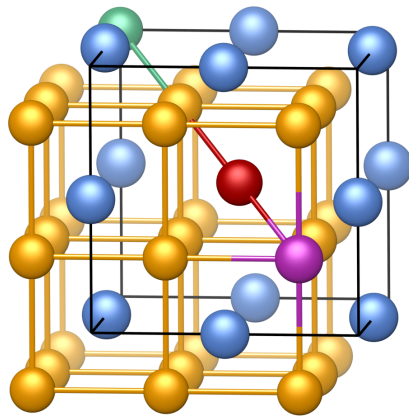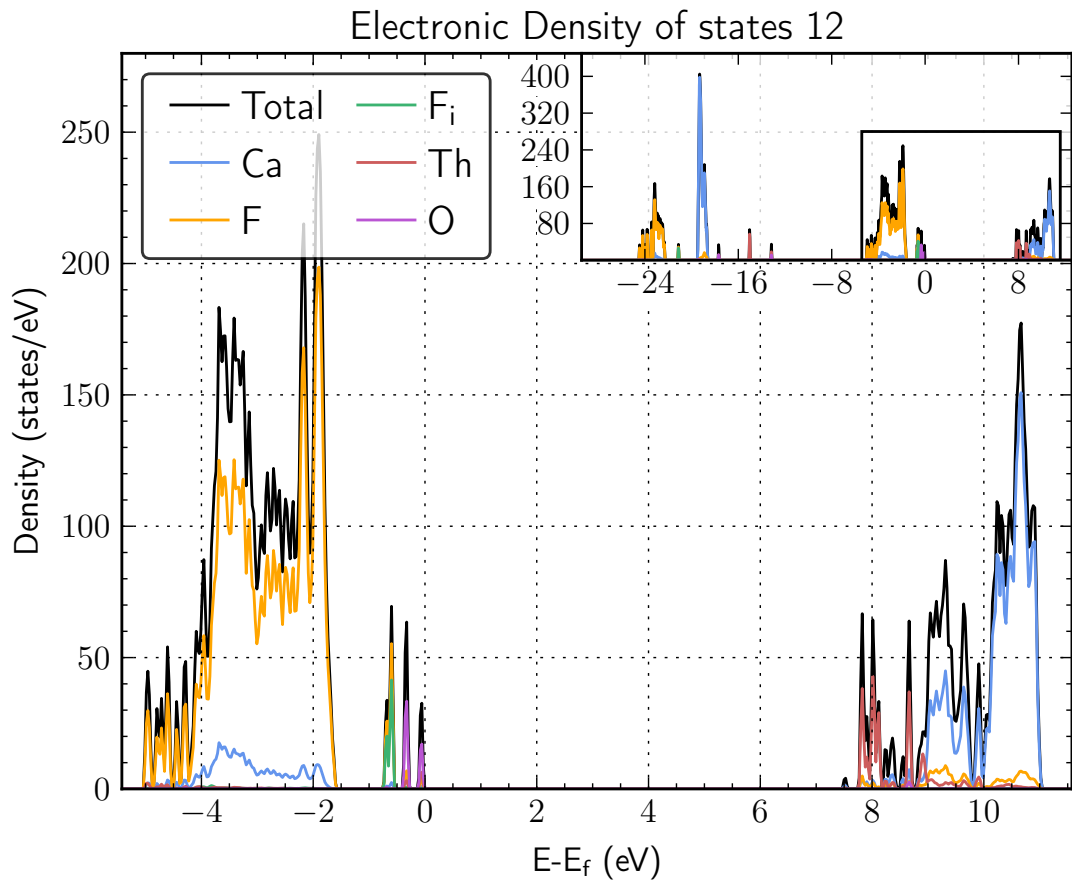

The structure of CaF_2 doped with Th_{sub}^{4+} and O_{sub}^{2-} $\left\{\frac{1}{2}\ \frac{1}{2}\ \frac{1}{2}\right\}$ and F_{int}^{-} $\{$-1-1-1$\}$ at 180°.

12. Th^{4+}_{sub} & O^{2-}_{sub} $\left\{\frac{1}{2}\ \frac{1}{2}\ \frac{1}{2}\right\}$ & F^-_{int} $\left\{\text{-1 1-1}\right\}$ at 109.5°
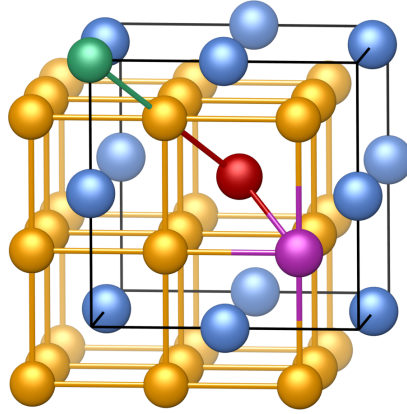
The structure of CaF_2 doped with Th^{4+}_{sub} and O^{2-}_{sub} $\left\{\frac{1}{2}\ \frac{1}{2}\ \frac{1}{2}\right\}$ and F^-_{int} $\left\{\text{-1 1-1}\right\}$ at 109.5°.
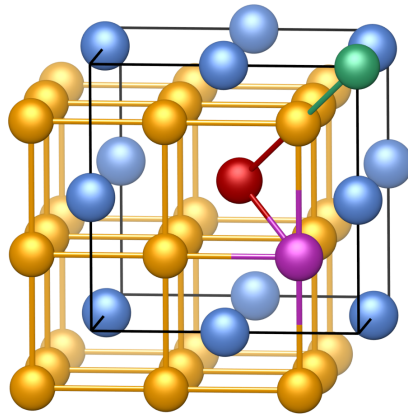
13. $\text{Th}^{4+}_{\text{sub}}$ & $\text{O}^{2-}_{\text{sub}}$ $\left\{\frac{1}{2}\ \frac{1}{2}\ \frac{1}{2}\right\}$ & F^-_{int} $\{1\ 1\text{-}1\}$ at 70.5°
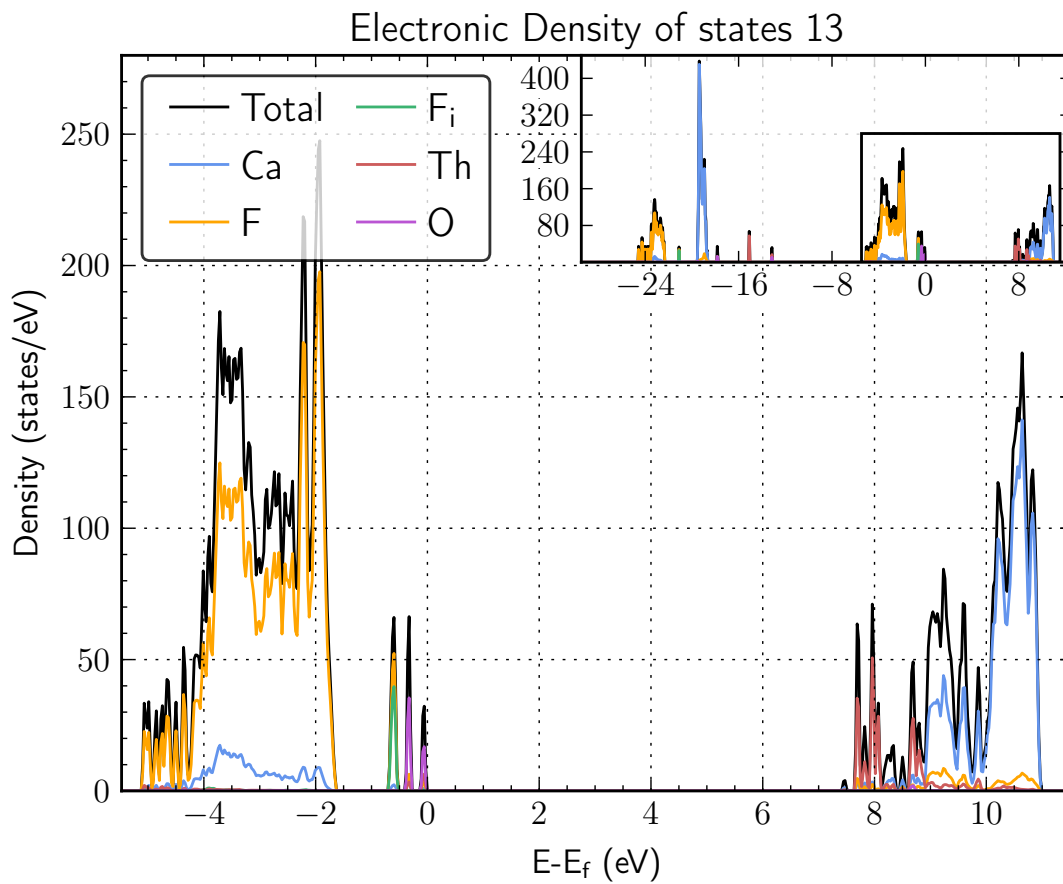

The structure of CaF_2 doped with $\text{Th}^{4+}_{\text{sub}}$ and $\text{O}^{2-}_{\text{sub}}$ $\left\{\frac{1}{2}\ \frac{1}{2}\ \frac{1}{2}\right\}$ and F^-_{int} $\{1\ 1\text{-}1\}$ at 70.5°.
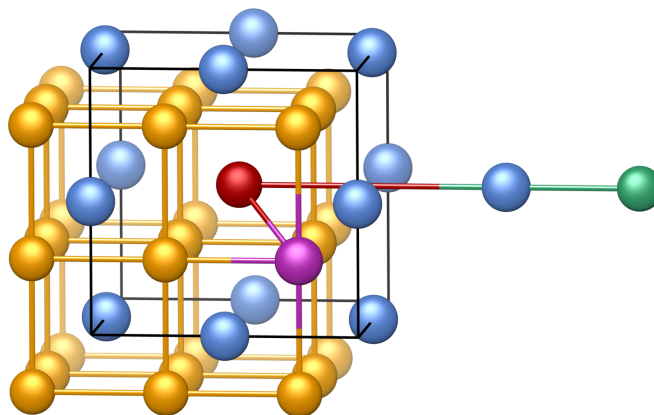
14. $\text{Th}^{4+}_{\text{sub}}$ & $\text{O}^{2-}_{\text{sub}}$ $\left\{\frac{1}{2} \; \frac{1}{2} \; \frac{1}{2}\right\}$ & $\text{F}^{-}_{\text{int}}$ $\left\{0 \; 0 \; 3\right\}$

The structure of CaF_2 doped with $\text{Th}^{4+}_{\text{sub}}$ and $\text{O}^{2-}_{\text{sub}}$ $\left\{\frac{1}{2} \; \frac{1}{2} \; \frac{1}{2}\right\}$ and $\text{F}^{-}_{\text{int}}$ $\left\{0 \; 0 \; 3\right\}$.
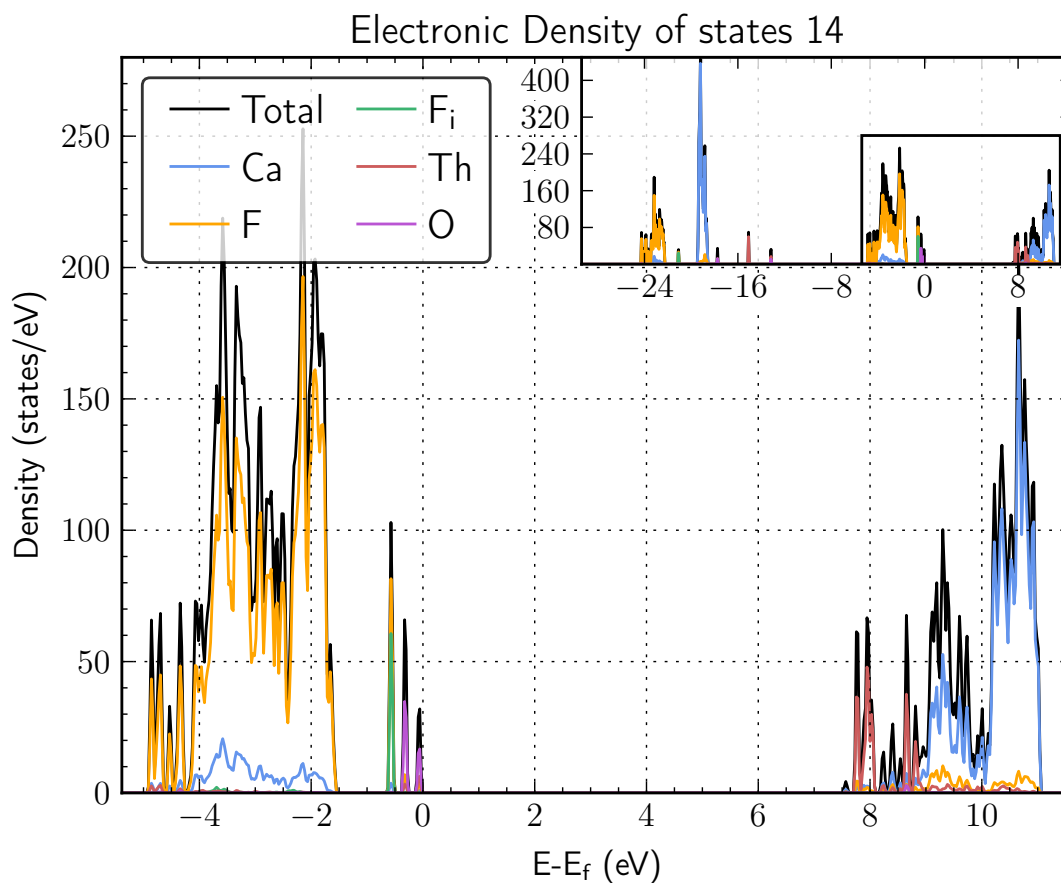
15. Th_{sub}^{4+} & O_{int}^{2-} $\{1\,0\,0\}$
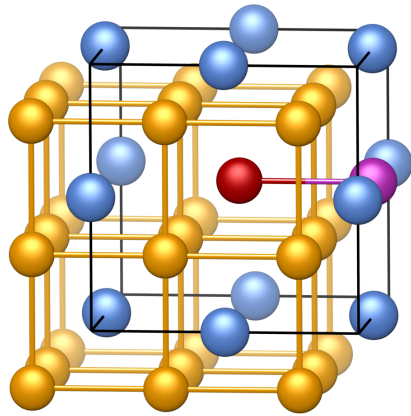
The structure of CaF_2 doped with Th_{sub}^{4+} and O_{int}^{2-} $\{1\,0\,0\}$.
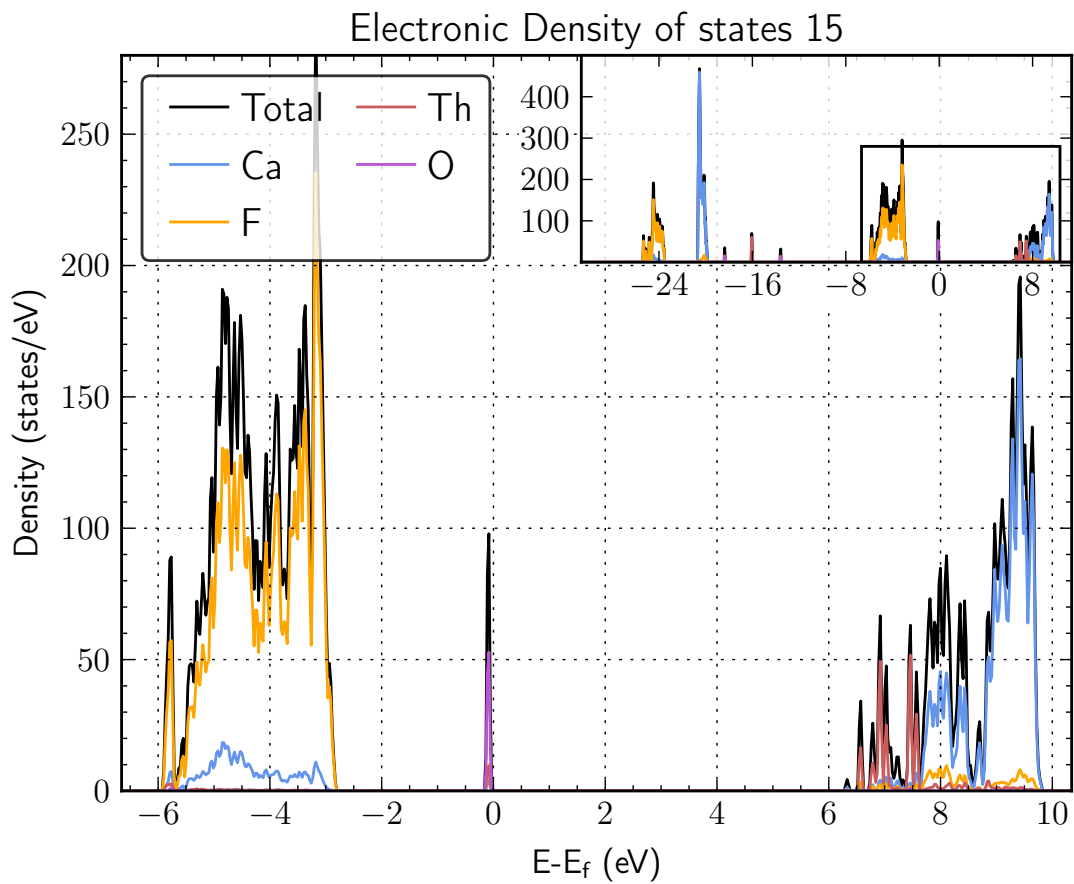
16. Th$_{sub}^{4+}$ & F$_{int}^{-}$ {1 0 0} & hole (e^{+})
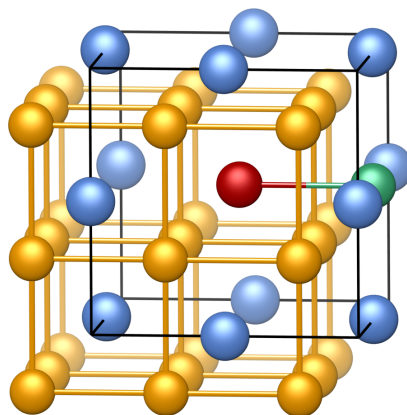
The structure of CaF$_2$ doped with Th$_{sub}^{4+}$ and F$_{int}^{-}$ {1 0 0} and hole (e^{+}).
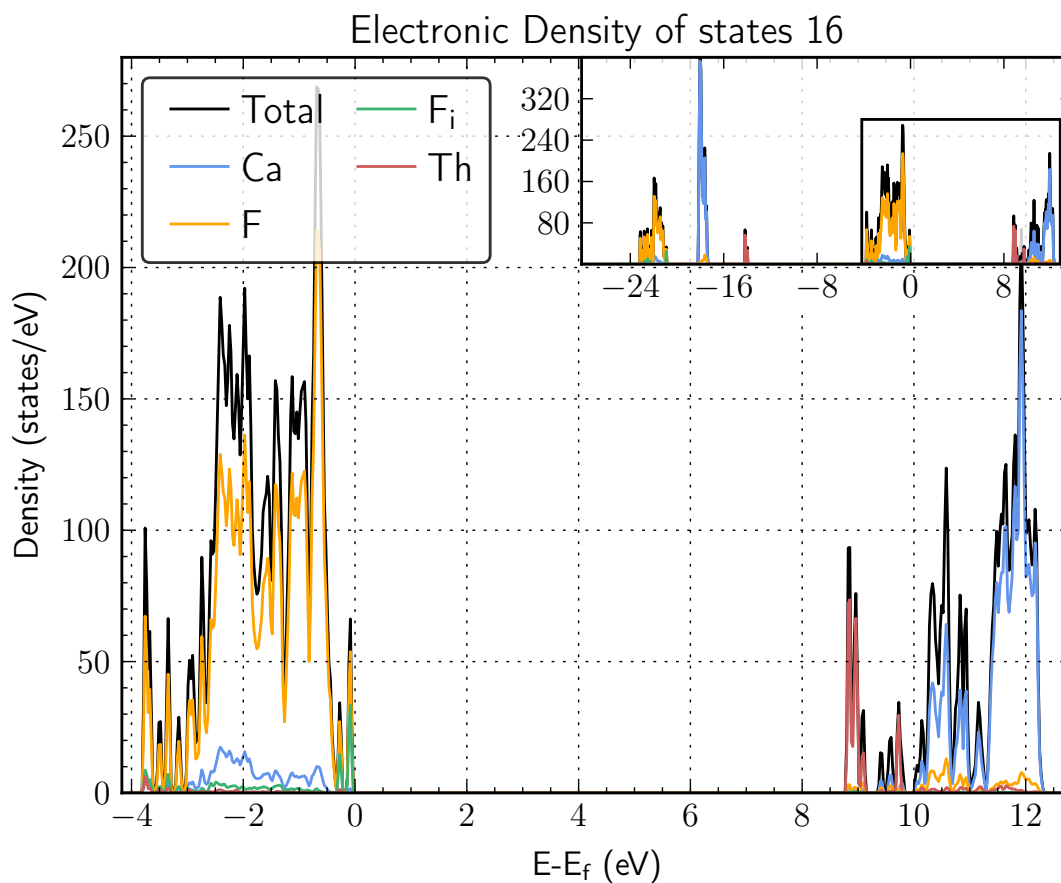
17. $\text{Th}_{\text{sub}}^{4+}$ & $\text{F}_{\text{int}}^{-}$ $\{1\ 1\ 1\}$ & hole (e^+)
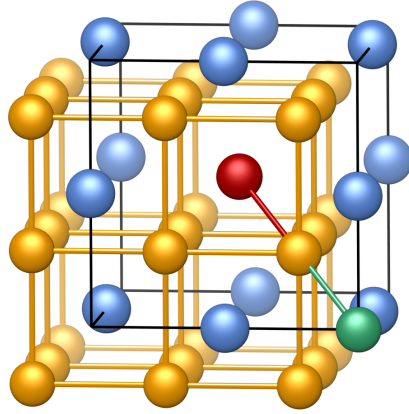
The structure of CaF_2 doped with $\text{Th}_{\text{sub}}^{4+}$ and $\text{F}_{\text{int}}^{-}$ $\{1\ 1\ 1\}$ and hole (e^+).
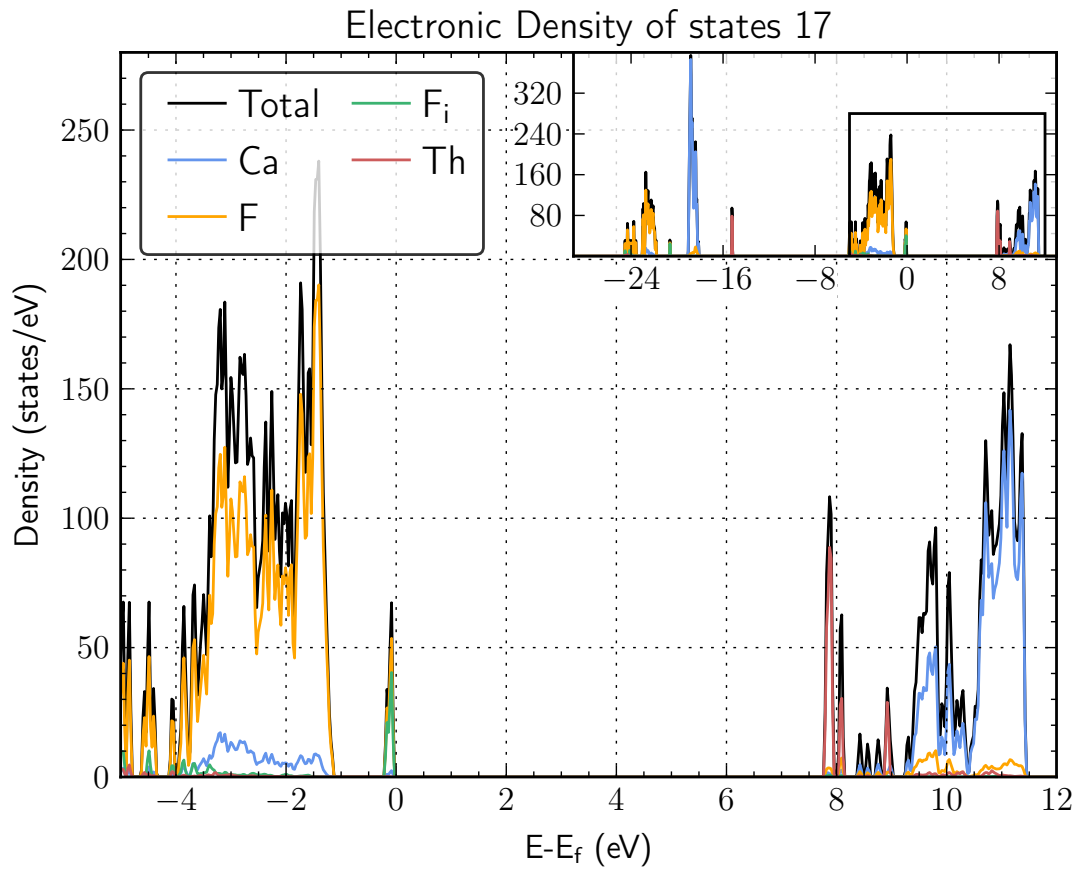
18. Th^{4+}_{sub} & F^-_{int} $\{0\ 0\ 3\}$ & hole (e^+)

The structure of CaF_2 doped with Th^{4+}_{sub} and F^-_{int} $\{0\ 0\ 3\}$ and hole (e^+).
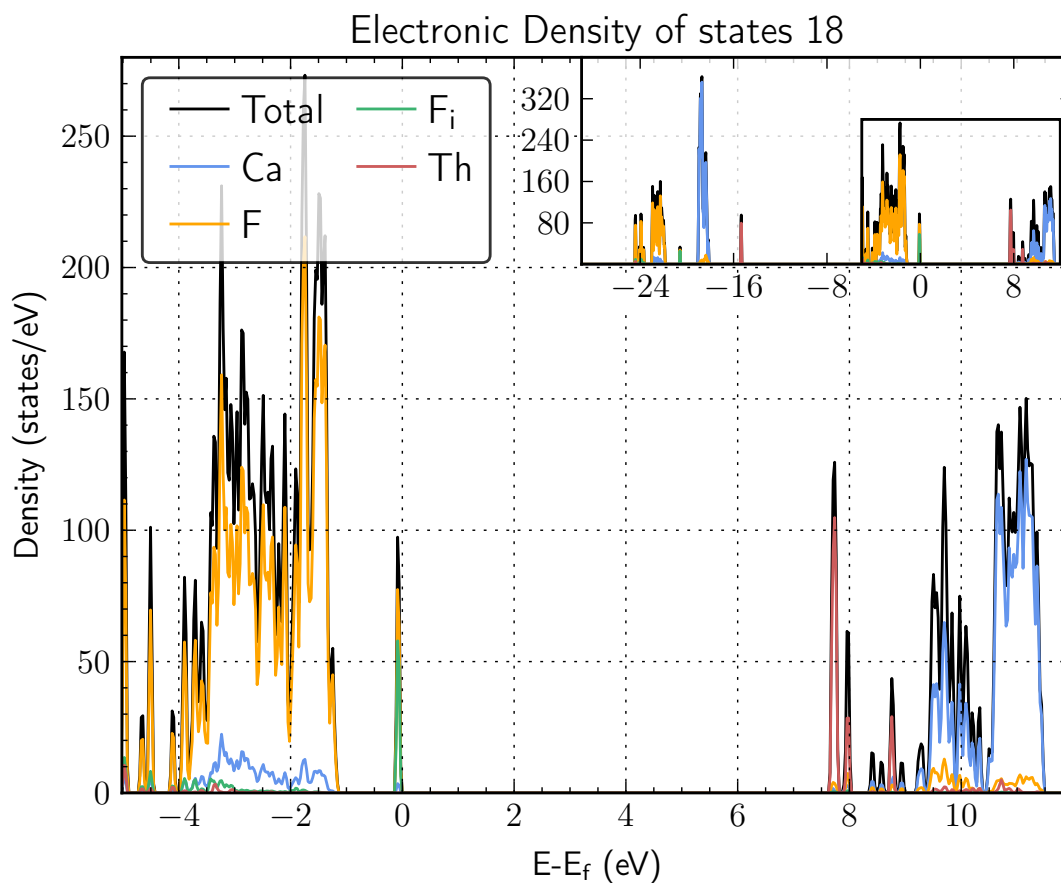
19. Th_{sub}^{4+} & F_{int}^{-} $\{1\,0\,0\}$ & 1x no charge compensation
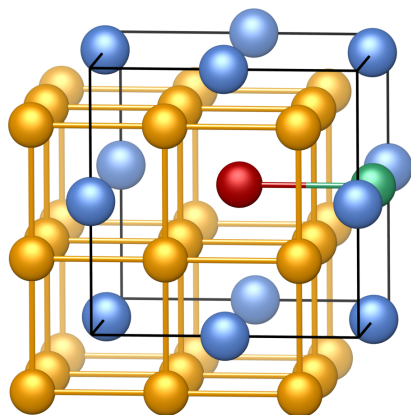
The structure of CaF_2 doped with Th_{sub}^{4+} and F_{int}^{-} $\{1\,0\,0\}$ and 1x no charge compensation.
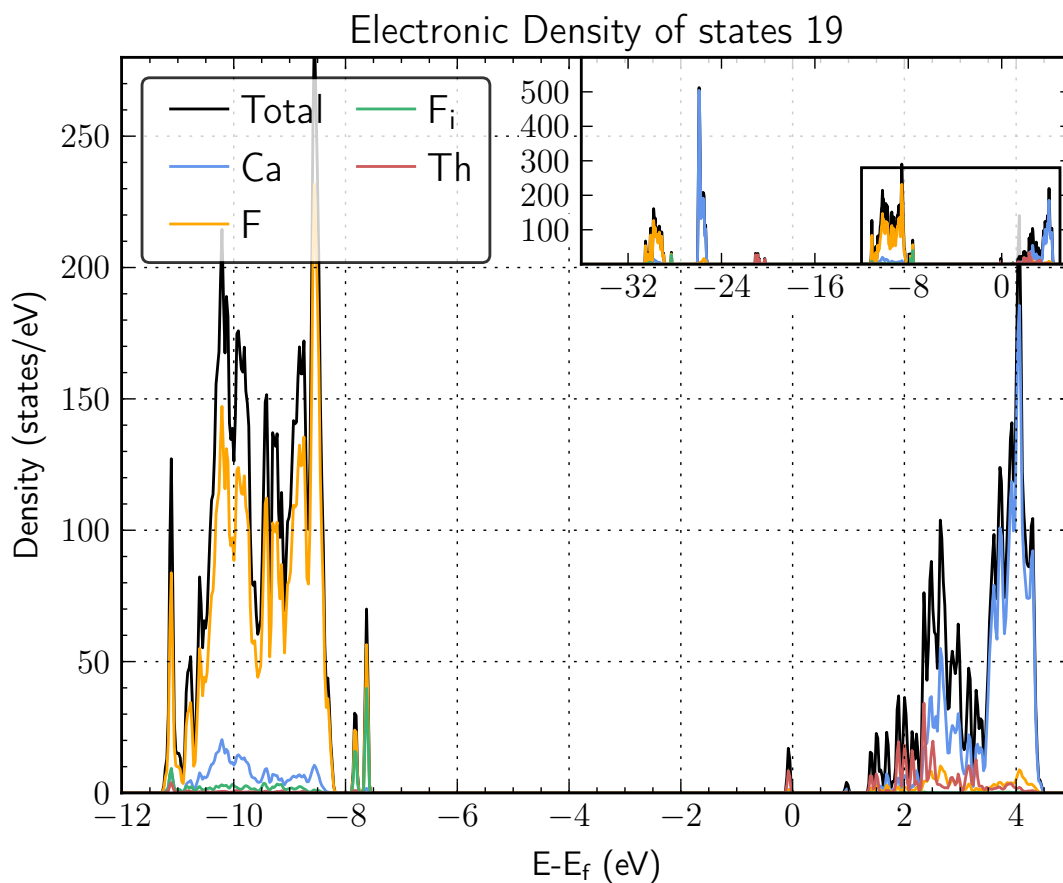
20. Th_{sub}^{4+} & F_{int}^{-} $\{1\,1\,1\}$ & 1x no charge compensation
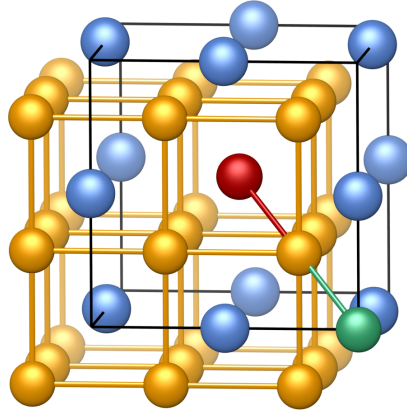
The structure of CaF_2 doped with Th_{sub}^{4+} and F_{int}^{-} $\{1\,1\,1\}$ and 1x no charge compensation.
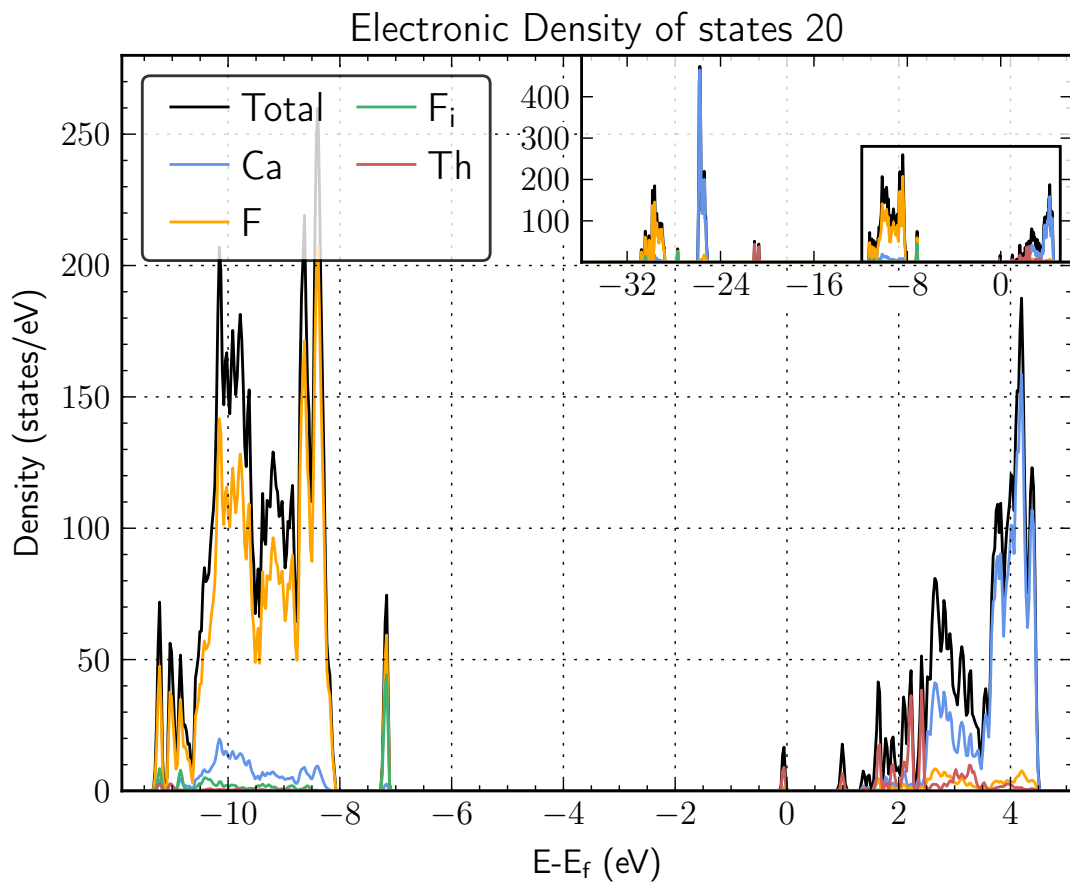
21. $\text{Th}_{\text{sub}}^{4+}$ & $\text{F}_{\text{int}}^{-}$ $\{0\ 0\ 3\}$ & 1x no charge compensation
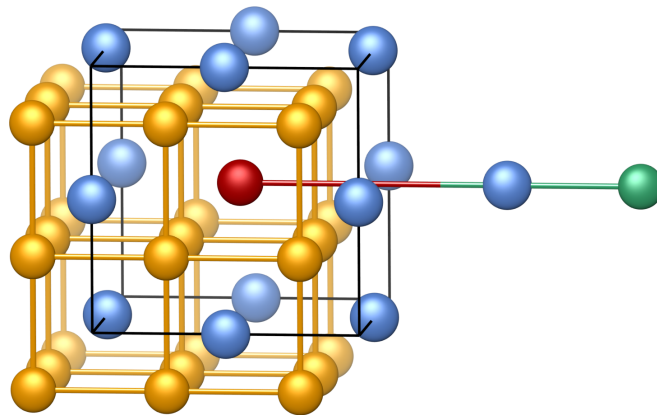
The structure of CaF_2 doped with $\text{Th}_{\text{sub}}^{4+}$ and $\text{F}_{\text{int}}^{-}$ $\{0\ 0\ 3\}$ and 1x no charge compensation.
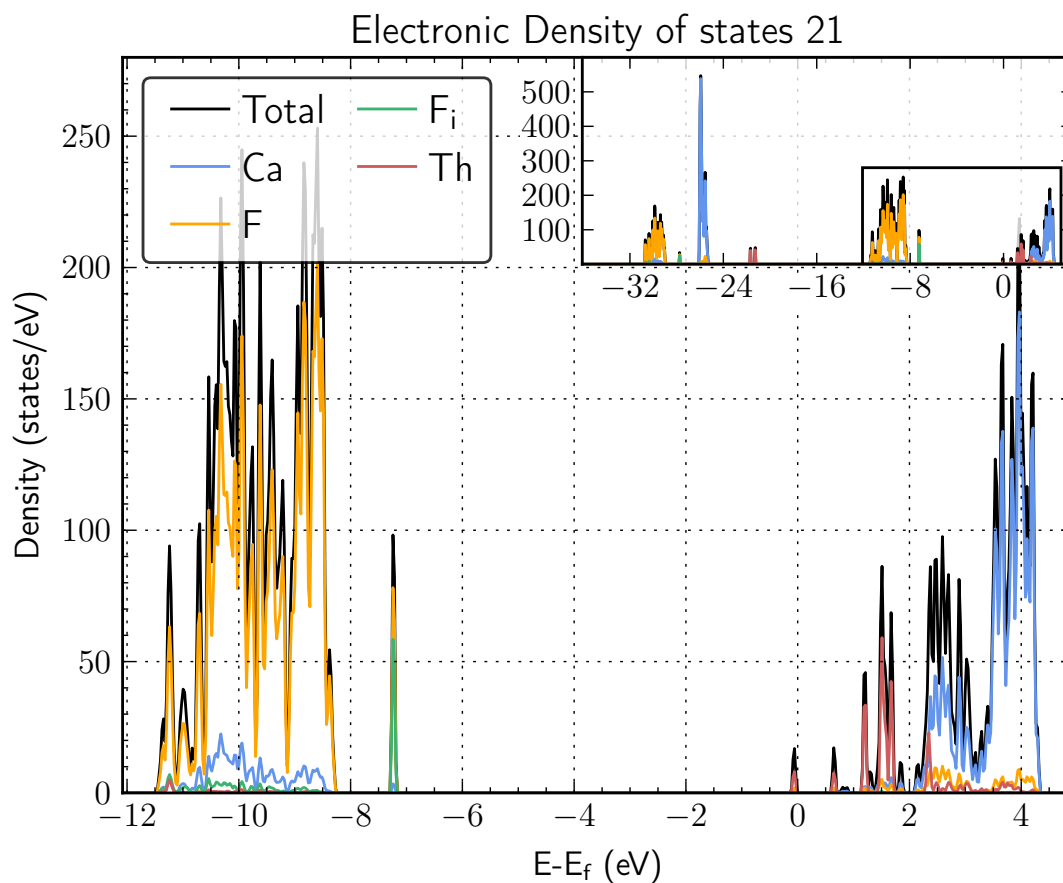
22. Th^{4+}_{sub} & F^-_{int} $\{1\ 0\ 0\}$ & F^-_{int} $\{\text{-}1\ 0\ 0\}$ at 180°
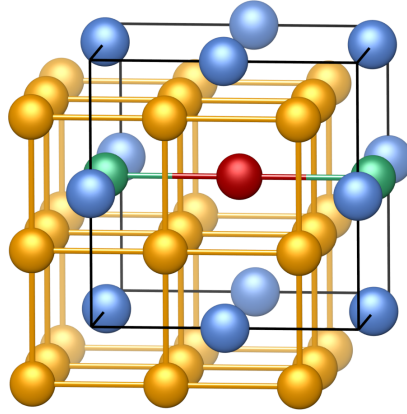
The structure of CaF_2 doped with Th^{4+}_{sub} and F^-_{int} $\{1\ 0\ 0\}$ and F^-_{int} $\{\text{-}1\ 0\ 0\}$ at 180°.
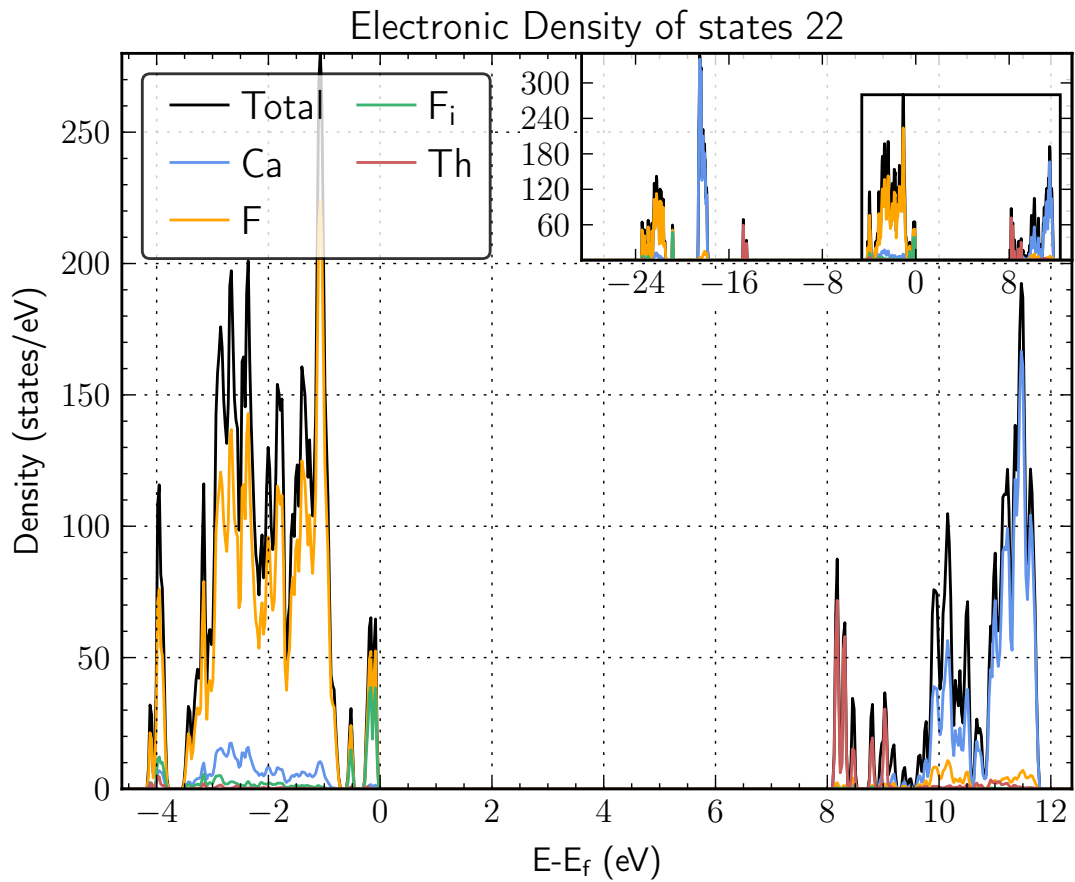
23. $\mathbf{Th^{4+}_{sub}}$ & $\mathbf{F^-_{int}}$ $\{1\ 0\ 0\}$ & $\mathbf{F^-_{int}}$ $\{0\ 1\ 0\}$ at 90°
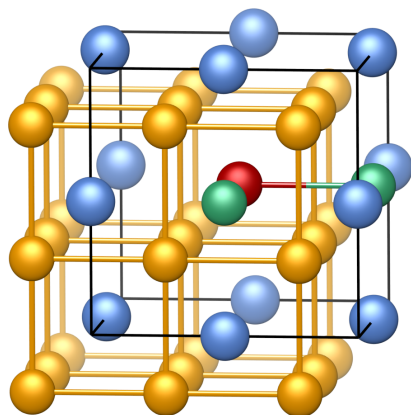
The structure of CaF_2 doped with Th^{4+}_{sub} and F^-_{int} $\{1\ 0\ 0\}$ and F^-_{int} $\{0\ 1\ 0\}$ at 90°.
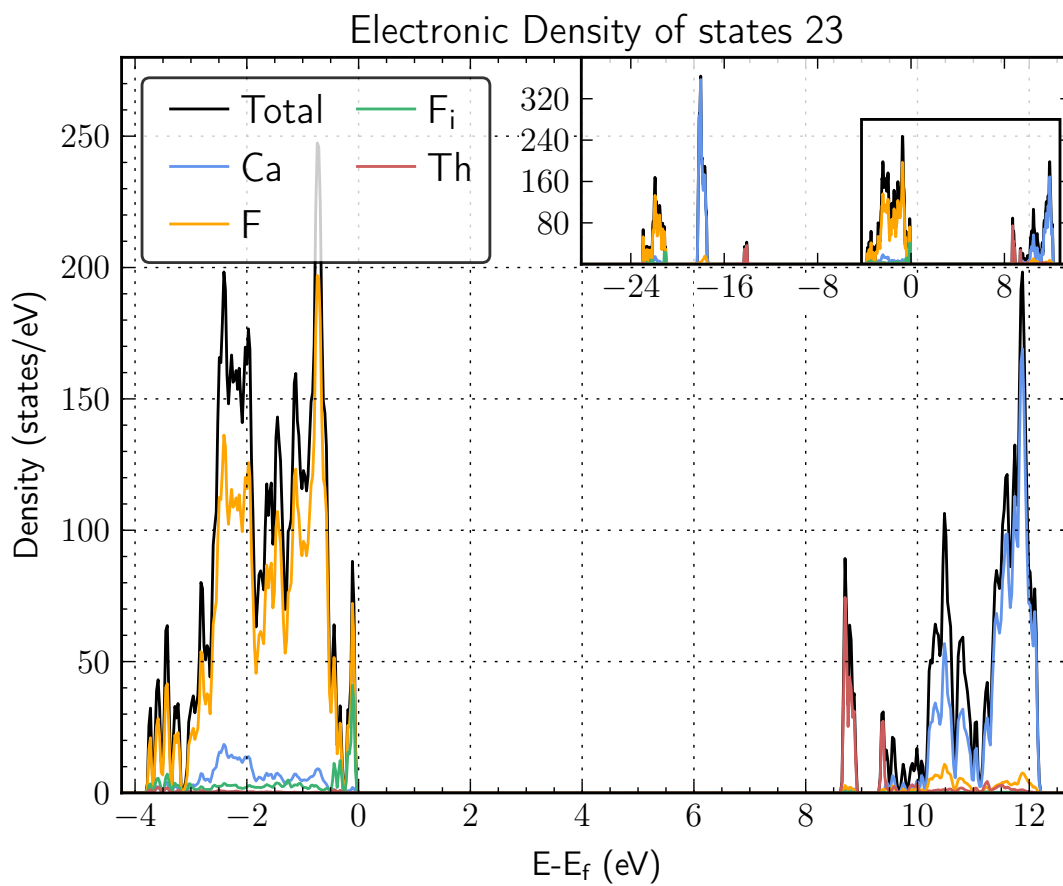
24. Th_{sub}^{4+} & F_{int}^- $\{1\,0\,0\}$ & F_{int}^- $\{1\,1\,1\}$ at 55°
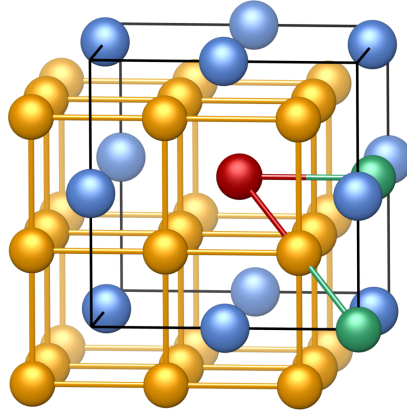
The structure of CaF_2 doped with Th_{sub}^{4+} and F_{int}^- $\{1\,0\,0\}$ and F_{int}^- $\{1\,1\,1\}$ at 55°.
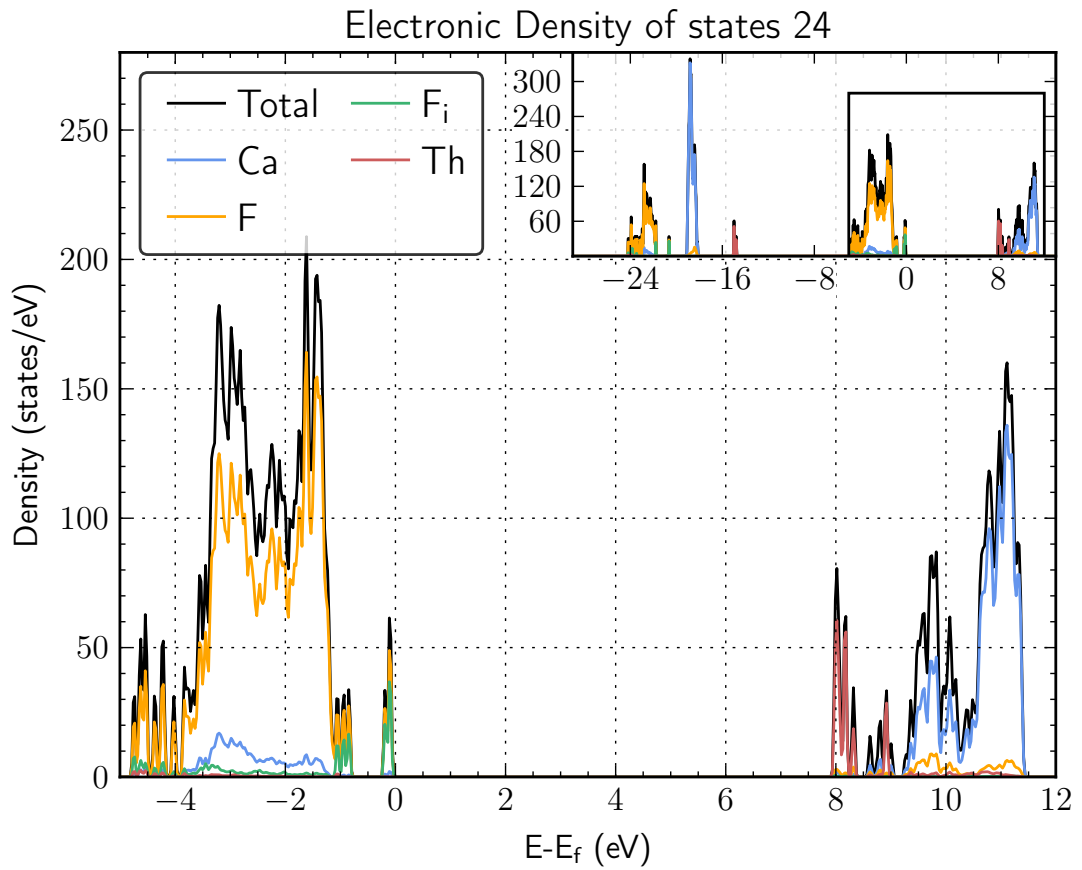
25. Th^{4+}_{sub} & F^-_{int} $\{1\ 0\ 0\}$ & F^-_{int} $\{$-1-1-1$\}$ at 125°
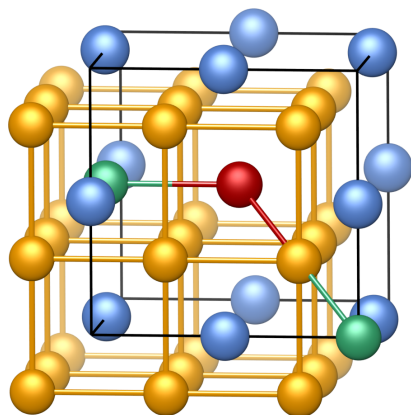
The structure of CaF_2 doped with Th^{4+}_{sub} and F^-_{int} $\{1\ 0\ 0\}$ and F^-_{int} $\{$-1-1-1$\}$ at 125°.
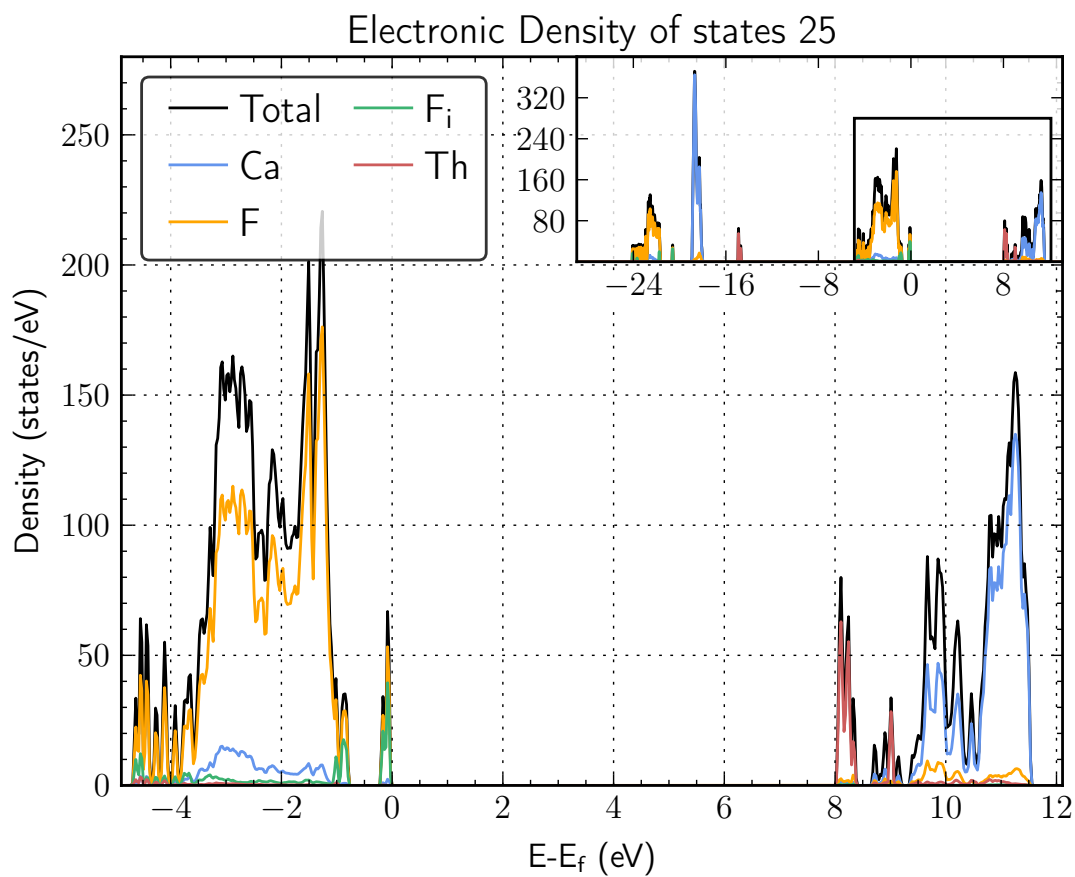
26. Th_{sub}^{4+} & F_{int}^- $\{1\,0\,0\}$ & F_{int}^- $\{0\,0\,3\}$
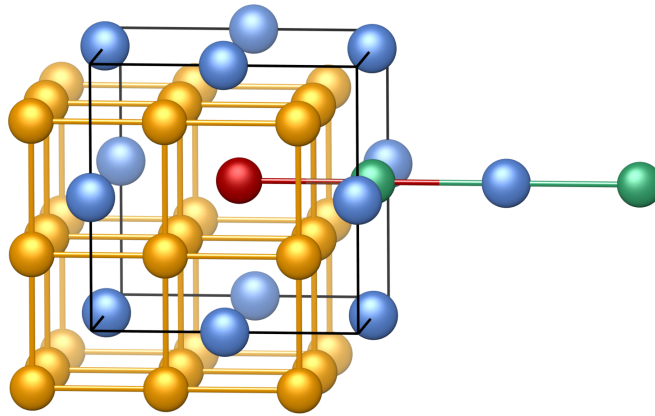
The structure of CaF_2 doped with Th_{sub}^{4+} and F_{int}^- $\{1\,0\,0\}$ and F_{int}^- $\{0\,0\,3\}$.
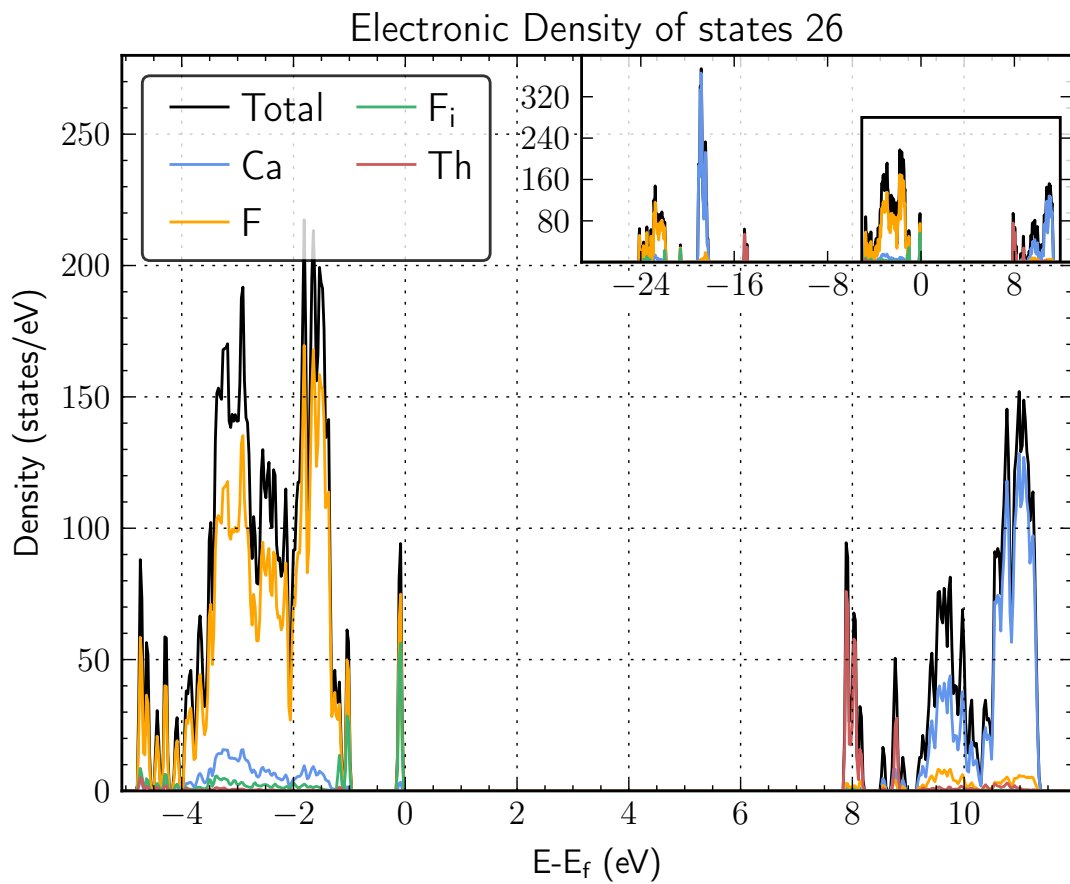
27. $\text{Th}_{\text{sub}}^{4+}$ & $\text{F}_{\text{int}}^{-}$ $\{1\ 1\ 1\}$ & $\text{F}_{\text{int}}^{-}$ $\{\text{-1-1-1}\}$ at 180°
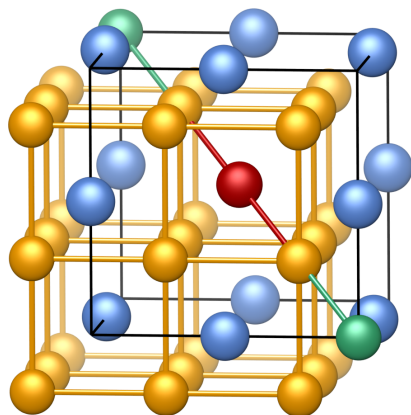
The structure of CaF_2 doped with $\text{Th}_{\text{sub}}^{4+}$ and $\text{F}_{\text{int}}^{-}$ $\{1\ 1\ 1\}$ and $\text{F}_{\text{int}}^{-}$ $\{\text{-1-1-1}\}$ at 180°.
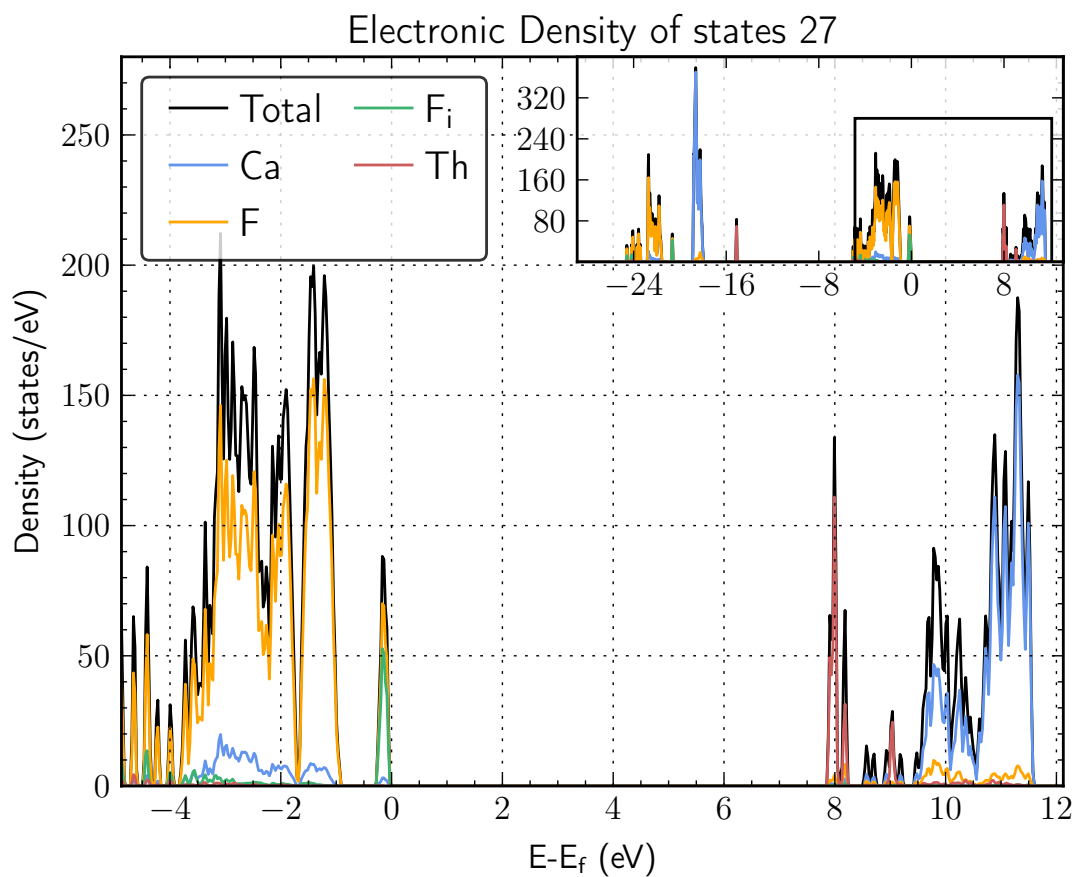
28. Th_{sub}^{4+} & F_{int}^- $\{1\ 1\ 1\}$ & F_{int}^- $\{-1\ 1\text{-}1\}$ at 109.5°
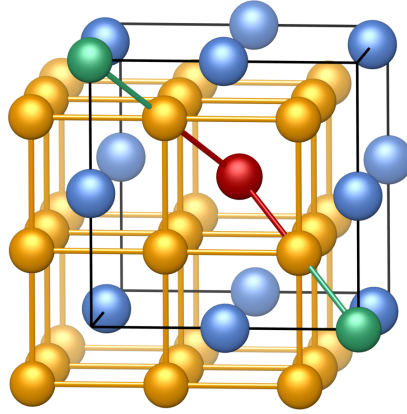
The structure of CaF_2 doped with Th_{sub}^{4+} and F_{int}^- $\{1\ 1\ 1\}$ and F_{int}^- $\{-1\ 1\text{-}1\}$ at 109.5°.
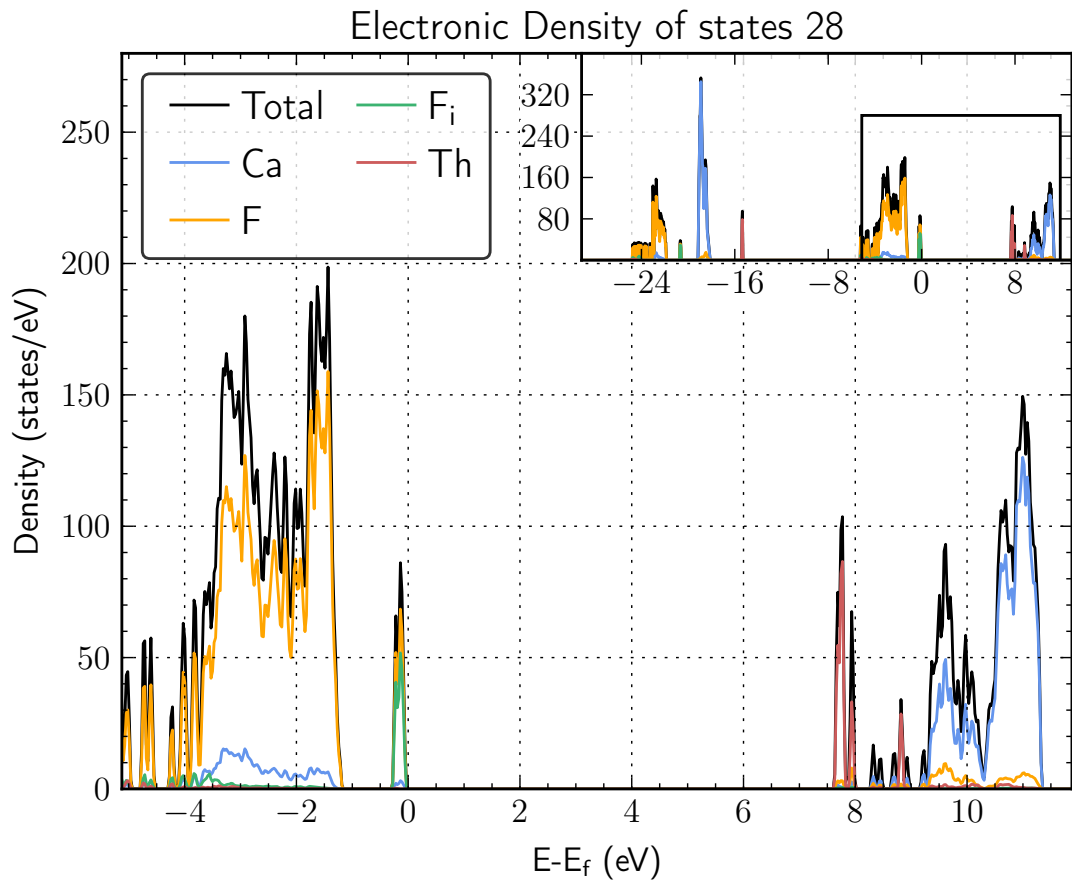
29. Th_{sub}^{4+} & F_{int}^- $\{1\ 1\ 1\}$ & F_{int}^- $\{1\ 1\text{-}1\}$ at 70.5°
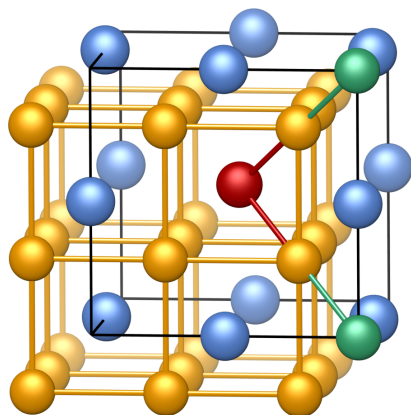
The structure of CaF_2 doped with Th_{sub}^{4+} and F_{int}^- $\{1\ 1\ 1\}$ and F_{int}^- $\{1\ 1\text{-}1\}$ at 70.5°.
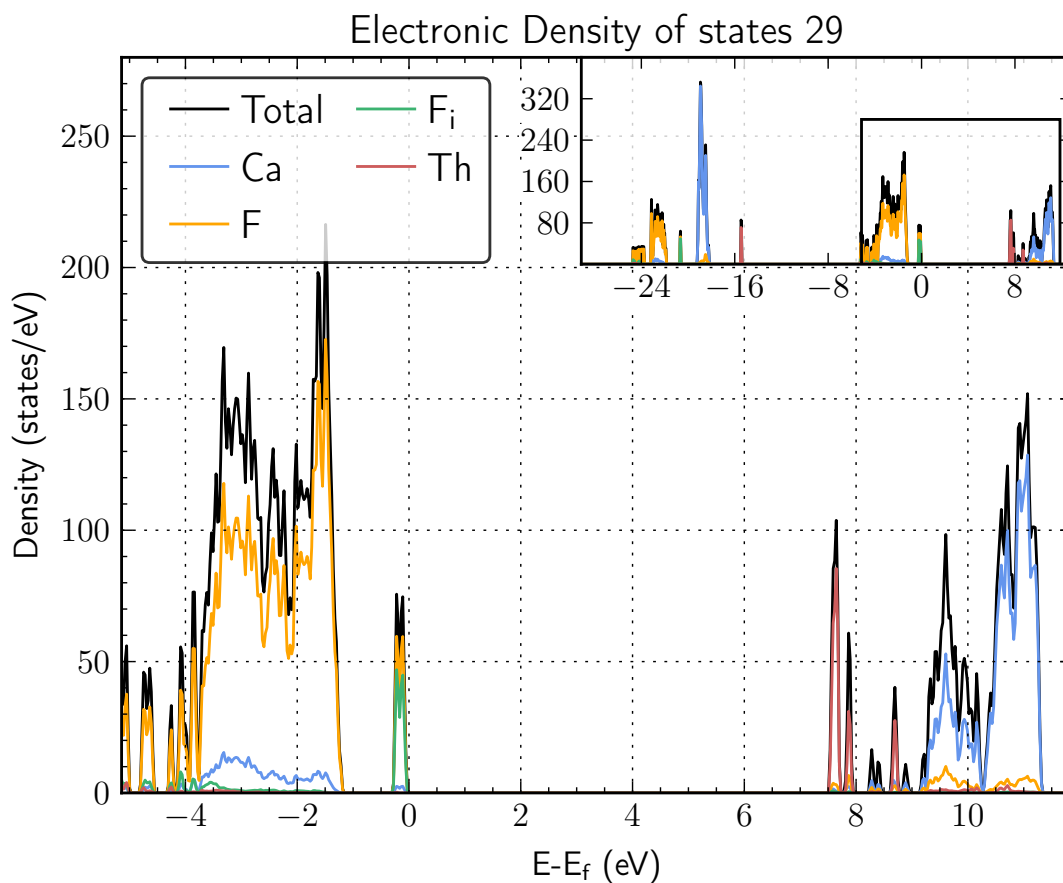
30. $\mathrm{Th}_{\mathbf{sub}}^{4+}$ & $\mathrm{F}_{\mathbf{int}}^{-}$ $\{1\,1\,1\}$ & $\mathrm{F}_{\mathbf{int}}^{-}$ $\{0\,0\,3\}$
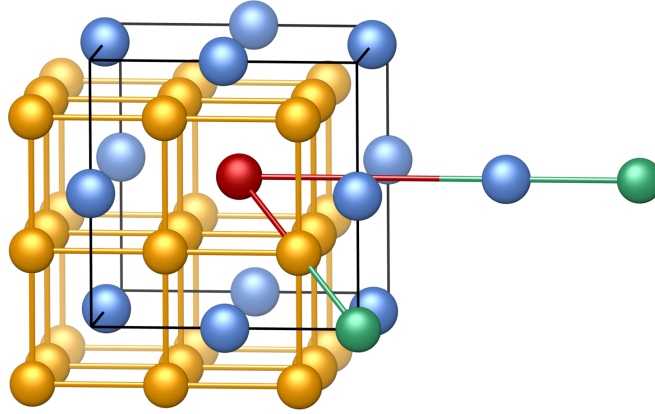
The structure of CaF_2 doped with Th_{sub}^{4+} and F_{int}^{-} $\{1\,1\,1\}$ and F_{int}^{-} $\{0\,0\,3\}$.
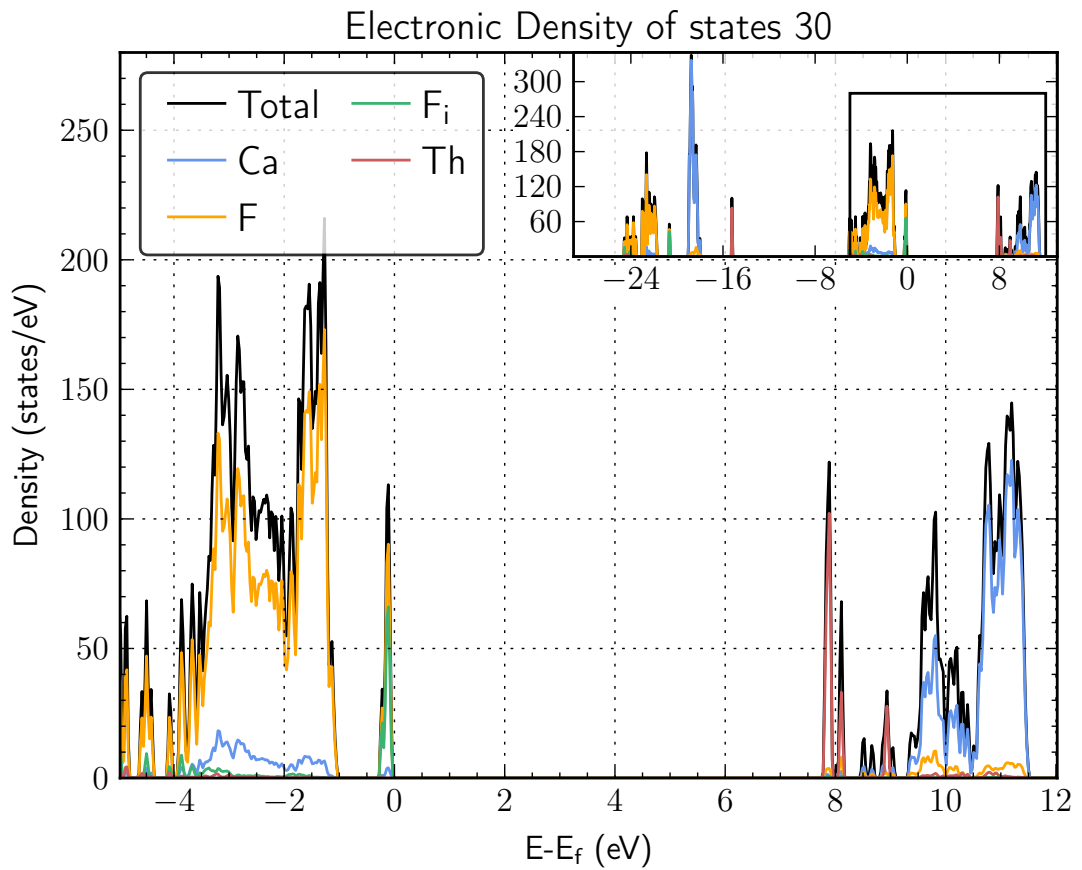
31. Th_{sub}^{4+} & Ca_{vac}^{2+} $\{1\,1\,0\}$
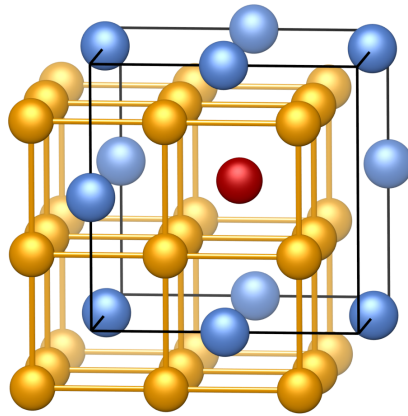
The structure of CaF_2 doped with Th_{sub}^{4+} and Ca_{vac}^{2+} $\{1\,1\,0\}$.
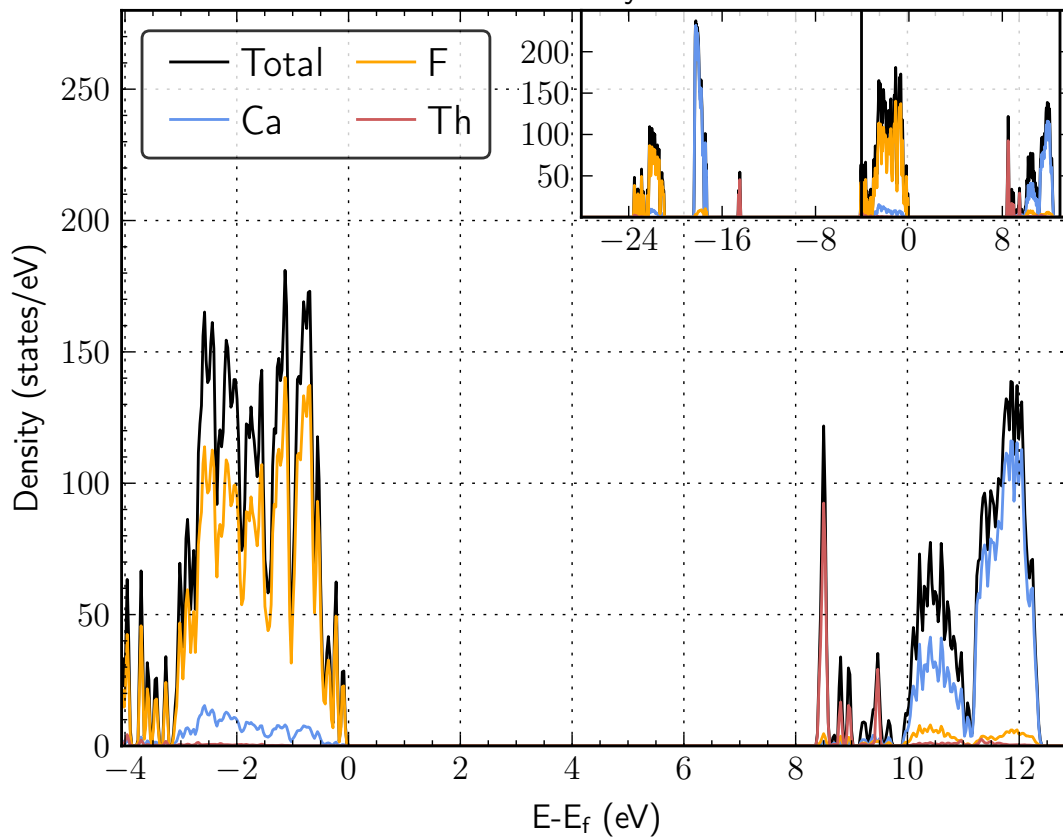
32. Th_{sub}^{4+} & Na_{sub}^{+} $\{1\ 1\ 0\}$ & Na_{sub}^{+} $\{0\text{-}1\text{-}1\}$ at 120°
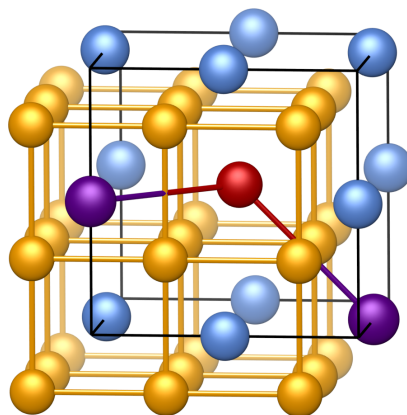
The structure of CaF_2 doped with Th_{sub}^{4+} and Na_{sub}^{+} $\{1\ 1\ 0\}$ and Na_{sub}^{+} $\{0\text{-}1\text{-}1\}$ at 120°.
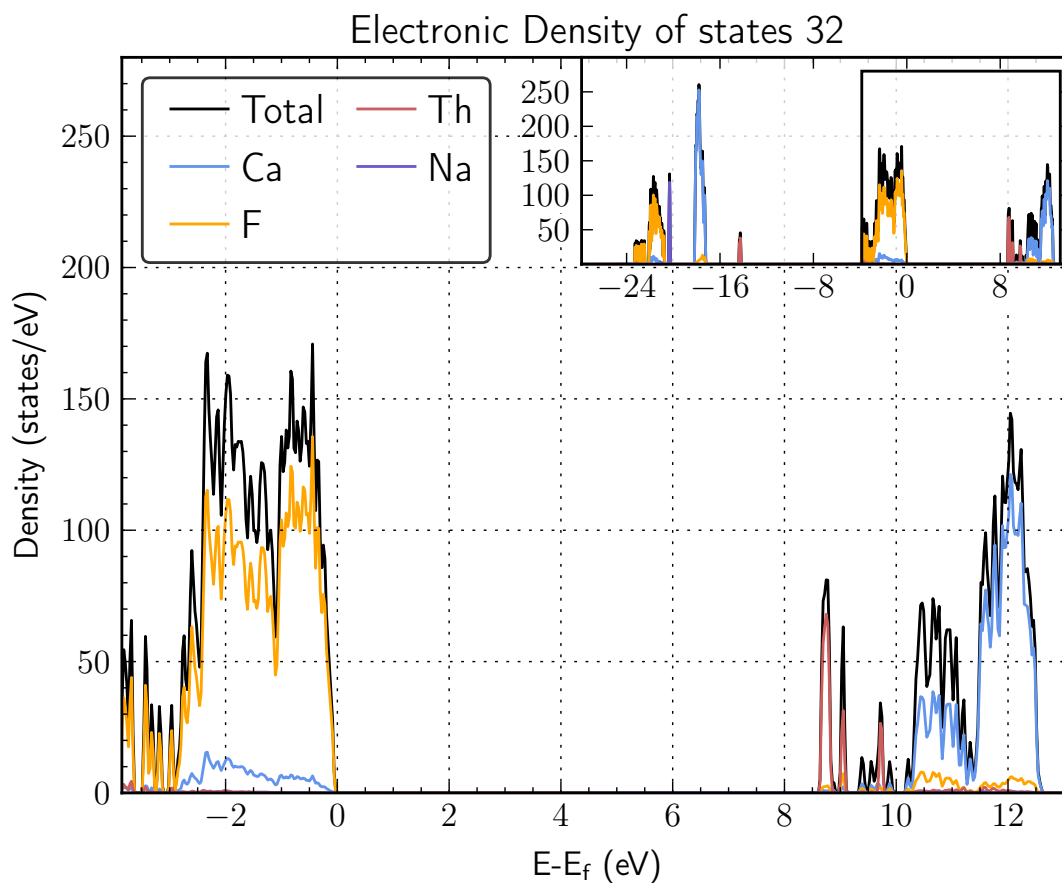
33. Th$_{sub}^{4+}$ & Na$_{sub}^+$ $\{1\,1\,0\}$ & Na$_{sub}^+$ $\{1\,0\,1\}$ at 60°
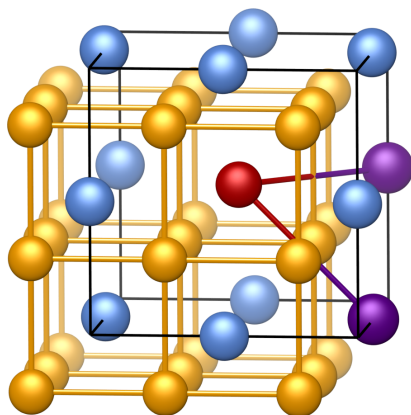
The structure of CaF_2 doped with Th$_{sub}^{4+}$ and Na$_{sub}^+$ $\{1\;1\;0\}$ and Na$_{sub}^+$ $\{1\;0\;1\}$ at 60°.
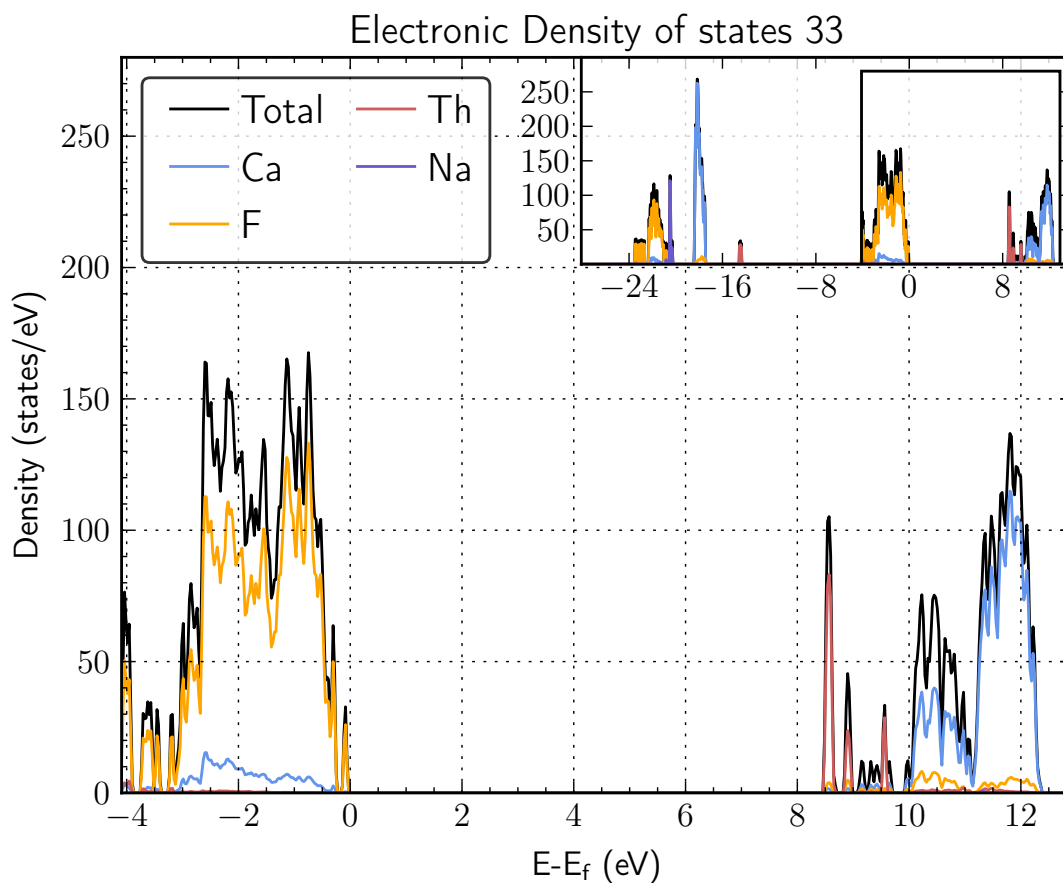
34. Th$^{4+}_{sub}$ & Na$^+_{sub}$ $\{1\,1\,0\}$ & Na$^+_{sub}$ $\{1\text{-}1\,0\}$ at 90°
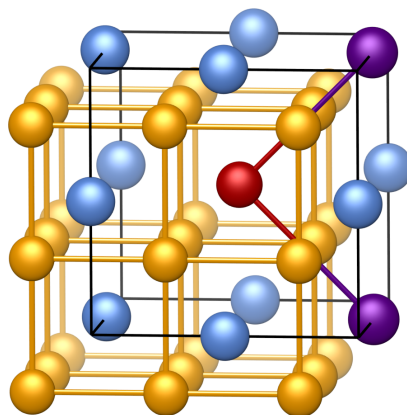
The structure of CaF$_2$ doped with Th$^{4+}_{sub}$ and Na$^+_{sub}$ $\{1\,1\,0\}$ and Na$^+_{sub}$ $\{1\text{-}1\,0\}$ at 90°.
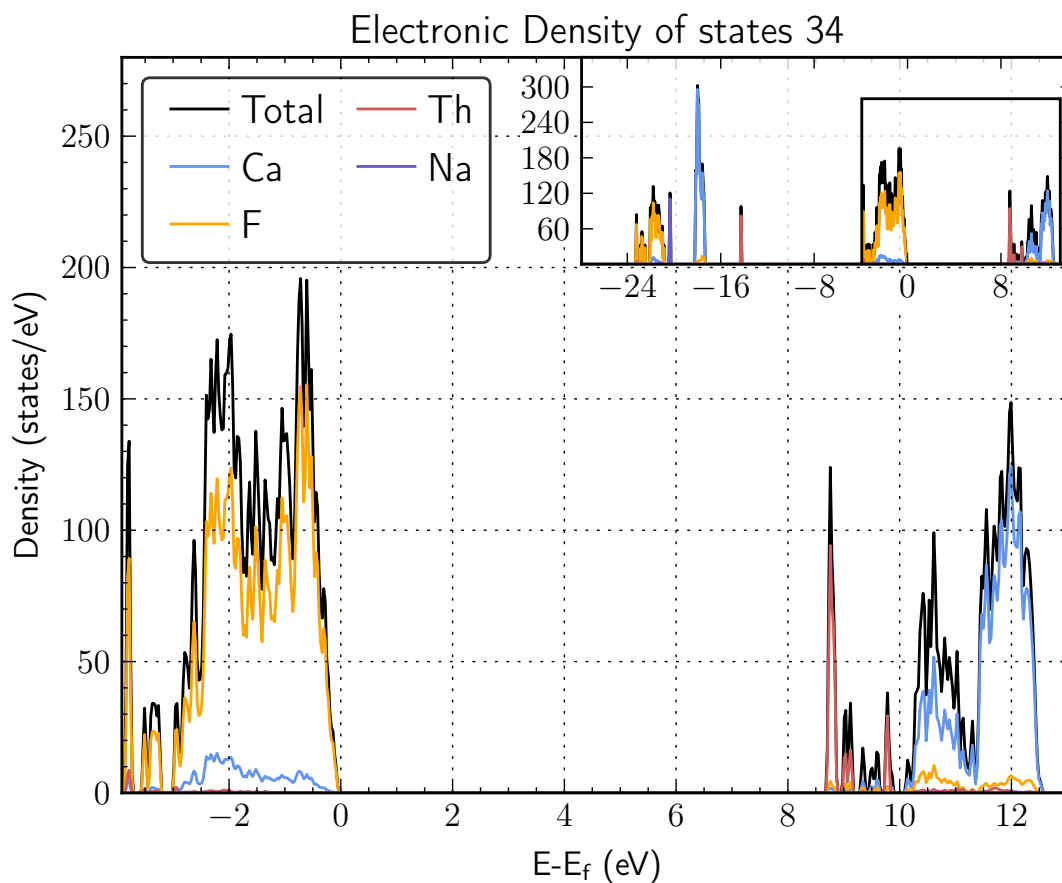
A.2. Configurations

No.	Charge Compensation		angle	#ions						#e⁻	
				Th	Ca	F	O	Na	Σ	Δ	Σ
00	undoped CaF$_2$			0	27	54	0	0	81	0	594
01	e^+	e^+		1	26	54	0	0	81	-2	596
02	none	none		1	26	54	0	0	81	0	598
03	O^{2-}_{sub} { 1 1 1}	e^+		1	26	53	1	0	81	-1	596
04	O^{2-}_{sub} { 1 1 1}	none		1	26	53	1	0	81	0	597
05	O^{2-}_{sub} { $\frac{1}{2}$ $\frac{1}{2}$ $\frac{1}{2}$}	O^{2-}_{sub} {-$\frac{1}{2}$-$\frac{1}{2}$-$\frac{1}{2}$}	180°	1	26	52	2	0	81	0	596
06	O^{2-}_{sub} { $\frac{1}{2}$ $\frac{1}{2}$ $\frac{1}{2}$}	O^{2-}_{sub} {-$\frac{1}{2}$ $\frac{1}{2}$-$\frac{1}{2}$}	109.5°	1	26	52	2	0	81	0	596
07	O^{2-}_{sub} { $\frac{1}{2}$ $\frac{1}{2}$ $\frac{1}{2}$}	O^{2-}_{sub} { $\frac{1}{2}$ $\frac{1}{2}$-$\frac{1}{2}$}	70.5°	1	26	52	2	0	81	0	596
08	O^{2-}_{sub} { $\frac{1}{2}$ $\frac{1}{2}$ $\frac{1}{2}$}	F^-_{int} {-1 0 0}	125.3°	1	26	54	1	0	82	0	604
09	O^{2-}_{sub} { $\frac{1}{2}$ $\frac{1}{2}$ $\frac{1}{2}$}	F^-_{int} { 1 0 0}	54.7°	1	26	54	1	0	82	0	604
10	O^{2-}_{sub} { $\frac{1}{2}$ $\frac{1}{2}$ $\frac{1}{2}$}	F^-_{int} { 1 1 1}	0°	1	26	54	1	0	82	0	604
11	O^{2-}_{sub} { $\frac{1}{2}$ $\frac{1}{2}$ $\frac{1}{2}$}	F^-_{int} {-1-1-1}	180°	1	26	54	1	0	82	0	604
12	O^{2-}_{sub} { $\frac{1}{2}$ $\frac{1}{2}$ $\frac{1}{2}$}	F^-_{int} {-1 1-1}	109.5°	1	26	54	1	0	82	0	604
13	O^{2-}_{sub} { $\frac{1}{2}$ $\frac{1}{2}$ $\frac{1}{2}$}	F^-_{int} { 1 1-1}	70.5°	1	26	54	1	0	82	0	604
14	O^{2-}_{sub} { $\frac{1}{2}$ $\frac{1}{2}$ $\frac{1}{2}$}	F^-_{int} {0 0 3}	-	1	26	54	1	0	82	0	604
15	O^{2-}_{int} { 1 0 0}			1	26	54	1	0	82	0	604
16	F^-_{int} { 1 0 0}	e^+		1	26	55	0	0	82	-1	604
17	F^-_{int} { 1 1 1}	e^+		1	26	55	0	0	82	-1	604
18	F^-_{int} { 0 0 3}	e^+		1	26	55	0	0	82	-1	604
19	F^-_{int} { 1 0 0}	none		1	26	55	0	0	82	0	605
20	F^-_{int} { 1 1 1}	none		1	26	55	0	0	82	0	605
21	F^-_{int} { 0 0 3}	none		1	26	55	0	0	82	0	605
22	F^-_{int} { 1 0 0}	F^-_{int} {-1 0 0}	180°	1	26	56	0	0	83	0	612
23	F^-_{int} { 1 0 0}	F^-_{int} { 0 1 0}	90°	1	26	56	0	0	83	0	612
24	F^-_{int} { 1 0 0}	F^-_{int} { 1 1 1}	54.7°	1	26	56	0	0	83	0	612
25	F^-_{int} { 1 0 0}	F^-_{int} {-1-1-1}	125.3°	1	26	56	0	0	83	0	612
26	F^-_{int} { 1 0 0}	F^-_{int} { 0 0 3}	-	1	26	56	0	0	83	0	612
27	F^-_{int} { 1 1 1}	F^-_{int} {-1-1-1}	180°	1	26	56	0	0	83	0	612
28	F^-_{int} { 1 1 1}	F^-_{int} {-1 1-1}	109.5	1	26	56	0	0	83	0	612
29	F^-_{int} { 1 1 1}	F^-_{int} { 1 1-1}	70.5	1	26	56	0	0	83	0	612
30	F^-_{int} { 1 1 1}	F^-_{int} { 0 0 3}	-	1	26	56	0	0	83	0	612
31	Ca^{2+}_{vac} { 1 1 0}			1	25	54	0	0	80	0	590
32	Na^+_{sub} { 1 1 0}	Na^+_{sub} { 0-1-1}	120°	1	24	54	0	2	81	0	596
34	Na^+_{sub} { 1 1 0}	Na^+_{sub} { 1-1 0}	90°	1	24	54	0	2	81	0	596
33	Na^+_{sub} { 1 1 0}	Na^+_{sub} { 1 0 1}	60°	1	24	54	0	2	81	0	596
35	Na^+_{sub} { 1 1 0}	Na^+_{sub} {-1-1 0}	180°	1	24	54	0	2	81	0	596

Table A.1.: An overview of all the calculated configurations. The penultimate column gives the number of artificially added electrons in for the charged crystal calculations.

B. Source Code

B.1. Program Setup

Listing B.1: create_subf_spin.sh: Creation directories for all structures
(POSCAR-files) and subdirectories for the different VASP-runs. Run
"start.sh" for each structure.

```bash
#/usr/bin/bash

for POSCAR in `echo "POSCAR_*"`
do
  name=
  name=${POSCAR:7}
  name=${name%.vasp}
  dir=Th:CaF2_$name
  echo $dir
  mkdir $dir
  cp -r nstd_HSE/*  $dir/
  cp $POSCAR $dir/POSCAR

  NA=${dir:8:2} #Get configuration number

  #If Na interstitials cp correct POTCAR file in directory
  if [[ "$NA" == "32" || "$NA" == "33" || "$NA" == "34" || "$NA"
      == "35" ]]; then
    cp $dir/POTCAR_NA  $dir/POTCAR
  fi

  #copy POTCAR in all subdirectories
  for subdir in $dir/* ; do if [ -d $subdir ]; then cp $dir/POTCAR
      ${subdir}/; fi ; done

  sed -i "3s/ .*/          0.00            1.007            1.007/" $dir/
      POSCAR
  sed -i "4s/ .*/          1.007            0.00            1.007/" $dir/
      POSCAR
  sed -i "5s/ .*/          1.007            1.007            0.00/" $dir/
      POSCAR
  cd $dir/

```

```
29     ./start.sh #set parameters and start the jobs
30     cd ..
31 done
```

Listing B.2: start.sh: Sets the correct number of electrons if necessary and submits the jobs to the queuing system on the server.

```
1  #/usr/bin/sh
2  SetNelect(){
3      if [[ "$NA" == "01" ]]; then
4        NELECT=596
5        sed -i "s/#␣NELECT␣=␣.*/␣NELECT␣=␣$NELECT/" $dir/INCAR
6        #echo 596 $NA $NELECT
7      elif [[ "$NA" == "03" ]]; then
8        NELECT=596
9        sed -i "s/#␣NELECT␣=␣.*/␣NELECT␣=␣$NELECT/" $dir/INCAR
10       #echo 596 $NA $NELECT
11     elif [[ "$NA" == "16" ||"$NA" == "17" ||"$NA" == "18" ]]; then
12       NELECT=604
13       sed -i "s/#␣NELECT␣=␣.*/␣NELECT␣=␣$NELECT/" $dir/INCAR
14       #echo 604 $NA $NELECT
15     fi
16 }
17
18 dirname=${PWD##*/}
19 name=${dirname:7}
20 NA=${dirname:8:2}
21
22 #set fakedir
23 dir=.
24
25 cd relax
26 #change nelect according to #electrons
27 SetNelect
28 NAME_JOB_rel=r$name
29 sed -i "s/\(#$␣-N␣\).*\(.*\)/\1␣"$NAME_JOB_rel"␣\2/" $dir/job
30 sed -i "s/\(␣System␣=␣\).*\(.*\)/\1␣"$NAME_JOB_rel"␣\2/" $dir/
     INCAR
31
32 qsub job
33 cd ..
34
35 cd preHSE
36 #change nelect according to #electrons
37 SetNelect
38 NAME_JOB_preH=pH$name
39 sed -i "s/\(#$␣-N␣\).*\(.*\)/\1␣"$NAME_JOB_preH"␣\2/" $dir/job
40 sed -i "s/\(␣System␣=␣\).*\(.*\)/\1␣"$NAME_JOB_preH"␣\2/" $dir/
     INCAR
```

```
41  sed -i "s/\(#$␣-hold_jid␣\).*\(.*\)/\1␣"$NAME_JOB_rel"␣\2/" job #>
        job_m
42
43  qsub job
44  cd ..
45  ##
46
47  cd rDOS
48  ###change nelect according to #electrons
49  SetNelect
50  sed -i "s/\(#$␣-N␣\).*\(.*\)/\1␣"rd$name"␣\2/" $dir/job
51  sed -i "s/\(␣System␣=␣\).*\(.*\)/\1␣"rd$name"␣\2/" $dir/INCAR
52  sed -i "s/\(#$␣-hold_jid␣\).*\(.*\)/\1␣"$NAME_JOB_rel"␣\2/" job #>
        job_m
53  qsub job
54  cd ..
55
56  cd DOS_HSEg
57  #change nelect according to #electrons
58  SetNelect
59  sed -i "s/\(#$␣-N␣\).*\(.*\)/\1␣"Hgf$name"␣\2/" $dir/job
60  sed -i "s/\(␣SYSTEM␣=␣\).*\(.*\)/\1␣"Hgf$name"␣\2/" $dir/INCAR
61  sed -i "s/\(#$␣-hold_jid␣\).*\(.*\)/\1␣"$NAME_JOB_preH"␣\2/" job #
        > job_m
62
63  qsub job
64  cd ..
```

B.2. Analyse results

Listing B.3: analyse7ad_hf.sh: To analyse the results of the different calculations
           for all structures, important values are aggregated in an tab seperated
           value file (*.tsv).

```
1   #! /bin/bash
2
3   NAME_JOB=Th:CaF2
4   FOUT="SUMMARY_"$NAME_JOB"_runs_HF.tsv"
5   WORKDIR=$PWD
6
7   read_dom () {
8       local IFS=\>
9       read -d \< ENTITY CONTENT
10  }
11
12  read_XML(){
```

```
13  while read_dom; do
14      if [[ $ENTITY = $1 ]]; then
15      IFS=' '
16      read  -rd '' var1 var2 var3 <<< "$CONTENT"
17  #     echo $var1 "/"$var2 "/"$var3 "/"$CONTENT
18      if  [[ $2 = 2 ]]; then
19        echo $var2
20  #   elif  [[ $2 = 3 ]]; then
21  #      echo $var3
22      elif [ -z "$2" ]; then
23        echo $CONTENT
24      fi
25          exit
26      fi
27  done  < vasprun.xml
28  }
29
30  print_Header () {
31      printf "%s:\t%s\t%s\t%s\t%s\t%s⎵⎵⎵⎵⎵\t%s⎵⎵⎵⎵⎵\t%s\t⎵%s\t⎵%s\t%
            s\t%s\t%s\t%s\t⎵%s\t%s\t%s\t%s\t%s\t%s\t%s\t%s\t%s\t" "
            ${1-⎵}"  "NPROC" "ISMEAR" "Encut" "k" "NKDPTS" "NKDIM" "
            NElect" "NBands" "rtime" "Energy" "Bandgap" "Latticep" "
            V_zz" "asymmetry" "Vxx" "Vyy" "Vzz" "Vxy" "Vxz" "Vyz" "
            FC_A_tot" "tot_hcp_zz" "tot_hcp_as">> $WORKDIR/$FOUT
32  }
33
34  print_Data () {
35    NPROC=0;ISMEAR=0;EC=;K=0;NKPTS=0;NKDIM=0;NELECT=0;NBANDS=0;T=0;E
          =0;L=0;EC=0;BG=0;Vzz=0;Asym=0;Vxxf=0;Vyyf=0;Vzzf=0;Vxyf=0;
          Vxzf=0;Vyzf=0
36    if [ -d "./$1" ]; then
37      cd $1
38      NPROC=`awk '/-pe mpich/ {print $4}' job`
39      K=`awk 'NR==4 {print $1}' KPOINTS`
40
41      if [ -s OUTCAR ]; then
42        EC=`awk '/ENCUT  =/ {print $3}' OUTCAR`
43        ISMEAR=`awk '/   ISMEAR = / {print $3}' OUTCAR`
44        if [ "$ISMEAR" = "-5;" ]; then
45          ISMEAR=t
46        elif [ "$ISMEAR" = "0;" ]; then
47          ISMEAR=g
48        else
49          ISMEAR=X
50        fi
51        NKPTS=`awk '/   k-points           NKPTS =    / {print $4}'
              OUTCAR`
52        NKDIM=`awk '/   k-points           NKPTS =    / {print $10}'
              OUTCAR`
```

```bash
NBANDS=`awk '/   k-points              NKPTS =    / {print $15
     }' OUTCAR`
NELECT=`awk '/   NELECT =     / {print $3}' OUTCAR`
T=`awk '/Total CPU time/ {print $6 /60}' OUTCAR | bc -l`
EC=`awk '/ENCUT  =/ {print $3}' OUTCAR`
if [ -s CONTCAR ]; then
  E=`awk 'END {print $5}' OSZICAR`
  L=`~/opt/vtstscripts/dist.pl CONTCAR POSCAR`
  #L=`awk 'NR==3 {print $3}' CONTCAR`
  BG=`bandgap.py`
  Vzz=`awk '/ion        V_xx       V_yy       V_zz
     asymmetry/ {getline; getline; while($0
     !~/-------------.*/) { x=$4; getline };print x}' OUTCAR
     `
  Asym=`awk '/ion        V_xx       V_yy       V_zz
     asymmetry/ {getline; getline; while($0
     !~/-------------.*/) { x=$5; getline };print x}' OUTCAR
     `
  Vxxf=`awk '/ ion        V_xx       V_yy       V_zz       V_xy
        V_xz       V_yz/ {getline; getline; while($0
     !~/-------------.*/) { x=$2; getline };print x}' OUTCAR
     `
  Vyyf=`awk '/ ion        V_xx       V_yy       V_zz       V_xy
        V_xz       V_yz/ {getline; getline; while($0
     !~/-------------.*/) { x=$3; getline };print x}' OUTCAR
     `
  Vzzf=`awk '/ ion        V_xx       V_yy       V_zz       V_xy
        V_xz       V_yz/ {getline; getline; while($0
     !~/-------------.*/) { x=$4; getline };print x}' OUTCAR
     `
  Vxyf=`awk '/ ion        V_xx       V_yy       V_zz       V_xy
        V_xz       V_yz/ {getline; getline; while($0
     !~/-------------.*/) { x=$5; getline };print x}' OUTCAR
     `
  Vxzf=`awk '/ ion        V_xx       V_yy       V_zz       V_xy
        V_xz       V_yz/ {getline; getline; while($0
     !~/-------------.*/) { x=$6; getline };print x}' OUTCAR
     `
  Vyzf=`awk '/ ion        V_xx       V_yy       V_zz       V_xy
        V_xz       V_yz/ {getline; getline; while($0
     !~/-------------.*/) { x=$7; getline };print x}' OUTCAR
     `
  FC_A_tot=`awk '/ion        A_pw       A_1PS      A_1AE
     A_1c      A_tot/ {getline; getline; while($0
     !~/-------------.*/) { x=$6; getline };print x}' OUTCAR
     `
  tot_hcp_zz=`awk '/  ion        A_xx       A_yy       A_zz
     asymmetry/ {getline; getline; while($0
     !~/-------------.*/) { x=$4; getline };print x}' OUTCAR
```

```bash
               '
        tot_hcp_as=`awk '/  ion        A_xx        A_yy        A_zz
            asymmetry/ {getline; getline; while($0
            !~/-------------.*/) { x=$5; getline };print x}' OUTCAR
            `



     fi
   fi
   cd ..
 fi
 printf "%s:\t%.0f\t%s\t%.0f\t%.0f\t%.0f\t%.0f\t%.0f\t%.0f\t%.2f\
     t%.4f\t%.4f\t%.4f\t%.4f\t%.4f\t%.4f\t%.4f\t%.4f\t%.4f\t%.4f\t
     %.4f\t%.4f\t%.4f\t%.4f\t" "${2-␣}" "${NPROC-0}"    "${ISMEAR-X
     }"   "${EC-0}"    "${K-0}"    "${NKPTS-0}"   "${NKDIM-0}"   "${
     NELECT-0}"   "${NBANDS-0}"     "${T-0}"    "${E-0}"    "${BG-0}"   "
     ${L-0}" "${Vzz-0}" "${Asym-0}" "${Vxxf-0}" "${Vyyf-0}" "${
     Vzzf-0}" "${Vxyf-0}" "${Vxzf-0}" "${Vyzf-0}" "${FC_A_tot-0}"
     "${tot_hcp_zz-0}" "${tot_hcp_as-0}" >> $WORKDIR/$FOUT
}

rm $FOUT
#enable for loops over items with spaces in their name
IFS=$'\n'

#print Headers for all analysed subdirectories
printf "%s\t%s:\t" "NA" "ChargeComp">> $WORKDIR/$FOUT
print_Header rel
print_Header rDos
print_Header preHSE
print_Header DOS_HSEg
print_Header Dos_HSEg_f_hf
printf "\n" >> $WORKDIR/$FOUT

#print Data for all analysed subdirectories and structures
for dir in `echo "$NAME_JOB*"`
do
  if [ -d "./$dir" ]; then
     echo $dir
     cd $dir/
     NA=${dir:8}
     NA=${NA%%_*}
     CC=${dir#Th\:CaF2_*_}
     printf "%s\t%s:\t" ${NA-NA} ${CC-CC}>> $WORKDIR/$FOUT
       print_Data relax relax
       print_Data rDOS rDOS
       print_Data preHSE preH
       print_Data DOS_HSEg Hgf
     printf "\n" >> $WORKDIR/$FOUT
```

104

```
110      cd $WORKDIR/
111    #break
112    fi
113 done
114
115 #sort -k1n -o $FOUT $FOUT
116 awk 'NR==1; NR > 1 {print $0 | "sort -n -k 1,1"}' $FOUT >> "$FOUT"
       tmp
117 mv "$FOUT"tmp "$FOUT"
118
119 echo "$FOUT"
120
121 cat $FOUT
```

Bibliography

[1] Nathan Argaman and Guy Makov. 'Density functional theory: An introduction'. In: *American Journal of Physics* 68.1 (2000), pp. 69–79. DOI: 10.1119/1.19375. arXiv: physics/9806013 [physics.ed-ph] (cit. on p. 3).

[2] T. Auckenthaler et al. 'Parallel solution of partial symmetric eigenvalue problems from electronic structure calculations'. In: *Parallel Computing* 37.12 (2011). 6th International Workshop on Parallel Matrix Algorithms and Applications (PMAA'10), pp. 783–794. ISSN: 0167-8191. DOI: 10.1016/j.parco.2011.05.002 (cit. on p. 12).

[3] Giovanni B Bachelet and Niels E Christensen. 'Relativistic and core-relaxation effects on the energy bands of gallium arsenide and germanium'. In: *Physical Review B* 31.2 (Jan. 1985), pp. 879–887. DOI: 10.1103/PhysRevB.31.879 (cit. on p. 12).

[4] S. R. Bahn and K. W. Jacobsen. 'An object-oriented scripting interface to a legacy electronic structure code'. English. In: *Computing in Science & Engineering* 4.3 (May 2002), pp. 56–66. ISSN: 1521-9615. DOI: 10.1109/5992.998641 (cit. on p. 12).

[5] J H Beaumont, J V Gee and W Hayes. 'Absorption in the vacuum ultraviolet of alkaline earth fluorides containing hydrogen'. In: *Journal of Physics C: Solid State Physics* 3.8 (1970), p. L152. DOI: 10.1088/0022-3719/3/8/027 (cit. on pp. 21, 22).

[6] B. R. Beck et al. 'Energy Splitting of the Ground-State Doublet in the Nucleus ^{229}Th'. In: *Physical Review Letters* 98 (14 Apr. 2007), p. 142501. DOI: 10.1103/PhysRevLett.98.142501 (cit. on p. 27).

[7] B R Beck et al. *Improved Value for the Energy Splitting of the Ground-State Doublet in the Nucleus 229mTh*. Tech. rep. Lawrence Livermore National Laboratory (LLNL), Livermore, CA, 30th July 2009. URL: http://www.osti.gov/scitech/servlets/purl/964521 (visited on 2016-04-28) (cit. on pp. 1, 27).

[8] B. T. Bernstein and J. F. Smith. 'Coefficients of thermal expansion for face-centered cubic and body-centered cubic calcium'. In: *Acta Crystallographica* 12.5 (May 1959), pp. 419–420. DOI: `10.1107/S0365110X59001268` (cit. on p. 19).

[9] P. E. Blöchl. 'Projector augmented-wave method'. In: *Physical Review B* 50 (24 Dec. 1994). blochl, pp. 17953–17979. DOI: `10.1103/PhysRevB.50.17953` (cit. on pp. 11, 12).

[10] P. E. Blöchl. 'Theory and Practice of Density-Functional Theory'. In: *ArXiv e-prints* (Aug. 2011). arXiv: `1108.1104 [cond-mat.other]` (cit. on pp. 3, 6, 7, 11).

[11] Edward N. Brothers et al. 'Accurate solid-state band gaps via screened hybrid electronic structure calculations'. In: *The Journal of Chemical Physics* 129.1, 011102 (2008), p. 011102. DOI: `10.1063/1.2955460` (cit. on p. 2).

[12] Kieron Burke and friends. *The ABC of DFT*. Department of Chemistry, University of California, Irvine, CA 92697. 10th Apr. 2007. URL: `http://www.chem.uci.edu/~kieron/dftold2/literature.php` (visited on 2016-04-28) (cit. on p. 3).

[13] C. J. Campbell et al. 'Multiply Charged Thorium Crystals for Nuclear Laser Spectroscopy'. In: *Phys. Rev. Lett.* 102 (23 June 2009), p. 233004. DOI: `10.1103/PhysRevLett.102.233004` (cit. on p. 1).

[14] C. J. Campbell et al. 'Single-Ion Nuclear Clock for Metrology at the 19th Decimal Place'. In: *Physical Review Letters* 108 (12 Mar. 2012), p. 120802. DOI: `10.1103/PhysRevLett.108.120802` (cit. on p. 1).

[15] J.A. Campbell et al. 'The defect structure of $CaF_2:U^{3+}$'. In: *Journal of Alloys and Compounds* 323–324 (2001). Proceedings of the 4th International Conference on f-Elements, pp. 111–114. ISSN: 0925-8388. DOI: `10.1016/S0925-8388(01)00977-X` (cit. on pp. 23, 24, 26).

[16] R. Car and M. Parrinello. 'Unified Approach for Molecular Dynamics and Density-Functional Theory'. In: *Phys. Rev. Lett.* 55 (22 Nov. 1985), pp. 2471–2474. DOI: `10.1103/PhysRevLett.55.2471` (cit. on p. 11).

[17] M Catti, A Pavese and V R Saunders. 'Elastic constants and electronic structure of fluorite (CaF_2): an ab initio Hartree-Fock study'. In: *Journal of Physics: Condensed Matter* 3.23 (1991), p. 4151. DOI: `10.1088/0953-8984/3/23/004` (cit. on p. 8).

[18] VSC - Vienna Scientific Cluster. *VSC-2*. Ed. by Zentraler Informatikdienst High Performance Computing Vienna University of Technology. 2011. URL: `http://vsc.ac.at/systems/vsc-2/` (visited on 2016-04-28) (cit. on p. 12).

[19] Christopher J. Cramer and Donald G. Truhlar. 'Density functional theory for transition metals and transition metal chemistry'. In: *Physical Chemistry Chemical Physics* 11.46 (2009), pp. 10757–10816. DOI: 10.1039/B907148B (cit. on pp. 2, 7–9).

[20] P Dessovic et al. '229 Thorium-doped calcium fluoride for nuclear laser spectroscopy'. In: *Journal of Physics: Condensed Matter* 26.10 (2014), p. 105402. DOI: 10.1088/0953-8984/26/10/105402 (cit. on pp. C, D, 56, 59).

[21] Alessio Filippetti and Nicola A Hill. 'Coexistence of magnetism and ferroelectricity in perovskites'. In: *Physical Review B* 65.19 (May 2002), p. 195120. DOI: 10.1103/PhysRevB.65.195120 (cit. on p. 12).

[22] V. V. Flambaum. 'Enhanced Effect of Temporal Variation of the Fine Structure Constant and the Strong Interaction in ^{229}Th'. In: *Physical Review Letters* 97 (9 Aug. 2006), p. 092502. DOI: 10.1103/PhysRevLett.97.092502 (cit. on p. 1).

[23] John B. Gruber et al. 'Spectroscopic properties of CaF_2:U^{4+} as a saturable absorber'. In: *Journal of Applied Physics* 90.8 (Oct. 2001), pp. 3965–3972. ISSN: 0021-8979. DOI: 10.1063/1.1396833 (cit. on pp. 25, 26).

[24] W. A. Hargreaves. 'Energy Levels of Uranium Ions in Calcium Fluoride Crystals'. In: *Physical Review B* 2 (7 Oct. 1970), pp. 2273–2284. DOI: 10.1103/PhysRevB.2.2273 (cit. on p. 26).

[25] W. A. Hargreaves. 'Optical spectra of U^{2+}, U^{3+}, and U^{4+} ions in calcium fluoride crystals'. In: *Physical Review B* 44 (10 Sept. 1991), pp. 5293–5295. DOI: 10.1103/PhysRevB.44.5293 (cit. on p. 25).

[26] Markus P. Hehlen et al. 'Optical spectroscopy of an atomic nucleus: Progress toward direct observation of the ^{229}Th isomer transition'. In: *Journal of Luminescence* 133 (2013). 16th International Conference on Luminescence ICL'11, pp. 91–95. ISSN: 0022-2313. DOI: 10.1016/j.jlumin.2011.09.037 (cit. on pp. 1, 27).

[27] Roland H. Hertwig and Wolfram Koch. 'On the parameterization of the local correlation functional. What is Becke-3-LYP?' In: *Chemical Physics Letters* 268.5–6 (1997), pp. 345–351. ISSN: 0009-2614. DOI: 10.1016/S0009-2614(97)00207-8 (cit. on p. 9).

[28] Jochen Heyd and Gustavo E. Scuseria. 'Assessment and validation of a screened Coulomb hybrid density functional'. In: *The Journal of Chemical Physics* 120.16 (2004), pp. 7274–7280. DOI: 10.1063/1.1668634 (cit. on p. 8).

[29]   Jochen Heyd and Gustavo E. Scuseria. 'Efficient hybrid density functional calculations in solids: Assessment of the Heyd–Scuseria–Ernzerhof screened Coulomb hybrid functional'. In: *The Journal of Chemical Physics* 121.3 (2004), pp. 1187–1192. DOI: `10.1063/1.1760074` (cit. on p. 9).

[30]   Jochen Heyd, Gustavo E. Scuseria and Matthias Ernzerhof. 'Erratum: "Hybrid functionals based on a screened Coulomb potential" [J. Chem. Phys.118, 8207 (2003)]'. In: *The Journal of Chemical Physics* 124.21, 219906 (2006), p. 219906. DOI: `10.1063/1.2204597` (cit. on pp. 8, 12).

[31]   Jochen Heyd, Gustavo E. Scuseria and Matthias Ernzerhof. 'Hybrid functionals based on a screened Coulomb potential'. In: *The Journal of Chemical Physics* 118.18 (2003), pp. 8207–8215. DOI: `10.1063/1.1564060` (cit. on pp. 8, 12).

[32]   P. Hohenberg and W. Kohn. 'Inhomogeneous Electron Gas'. In: *Physical Review* 136 (3B Nov. 1964), B864–B871. DOI: `10.1103/PhysRev.136.B864` (cit. on p. 3).

[33]   Gary J. Hollingsworth and Donald S. McClure. 'Photoionization and photochemical production of color centers in Ce^{3+}- and Ce^{3+}:Na^+-doped CaF_2'. In: *Physical Review B* 48 (18 Nov. 1993), pp. 13280–13285. DOI: `10.1103/PhysRevB.48.13280` (cit. on pp. 24, 25).

[34]   M. Huisinga. 'Ultraviolet photoelectron spectroscopy and electron stimulated desorption from CaF_2'. PhD thesis. Freien Universität Berlin, 1998. URN: `urn:nbn:de:kobv:188-1999000249`. (Visited on 2016-04-28) (cit. on pp. 13, 19, 20).

[35]   John D. Hunter. 'Matplotlib: A 2D graphics environment'. In: *Computing In Science & Engineering* 9.3 (2007), pp. 90–95. DOI: `10.1109/MCSE.2007.55` (cit. on p. 12).

[36]   JabRef Development Team. *JabRef*. 2016. URL: `http://jabref.sf.net` (visited on 2016-04-28) (cit. on p. 12).

[37]   Robert A Jackson et al. 'Computer modelling of thorium doping in $LiCaAlF_6$ and $LiSrAlF_6$: application to the development of solid state optical frequency devices'. In: *Journal of Physics: Condensed Matter* 21.32 (2009), p. 325403. URL: `http://stacks.iop.org/0953-8984/21/i=32/a=325403` (cit. on p. 1).

[38]   PWM Jacobs and SH Ong. 'Point defect parameters for calcium fluoride from ionic conductivity measurements at low temperatures'. In: *Le Journal de Physique Colloques* 37.C7 (1976), pp. 7–7. DOI: `10.1051/jphyscol:1976777` (cit. on pp. 25, 54).

[39] G A Kazakov et al. 'Performance of a ^{229}Thorium solid-state nuclear clock'. In: *New Journal of Physics* 14.8 (2012), p. 083019. URL: http://stacks.iop.org/1367-2630/14/i=8/a=083019 (cit. on p. 1).

[40] *Isomers in Nuclear and Interdisciplinary Research: Proceedings of the International Conference. Atomic clock with nuclear transition: current status in TU Wien.* Peterhof, Russia, 2011, pp. 108–117. ISBN: 978-5-9530-0316-2. arXiv: 1110.0741 (cit. on p. 1).

[41] H. Kikunaga et al. 'Determination of the half-life of the ground state of ^{229}Th by using ^{232}U and ^{233}U decay series'. In: *Physical Review C: Nuclear Physics* 84 (1 July 2011), p. 014316. DOI: 10.1103/PhysRevC.84.014316 (cit. on p. 27).

[42] C. Kittel. *Introduction to solid state physics.* Wiley, 2005. ISBN: 9780471415268 (cit. on p. 20).

[43] W. Kohn and L. J. Sham. 'Self-Consistent Equations Including Exchange and Correlation Effects'. In: *Physical Review* 140 (4A Nov. 1965), A1133–A1138. DOI: 10.1103/PhysRev.140.A1133 (cit. on pp. 3, 6).

[44] H. Kojima, S. G. Whiteway and C. R. Masson. 'Melting points of inorganic fluorides'. In: *Canadian Journal of Chemistry* 46.18 (1968), pp. 2968–2971. DOI: 10.1139/v68-494 (cit. on p. 13).

[45] Robert E. Krebs. *The History and Use of Our Earth's Chemical Elements: A Reference Guide.* Greenwood Publishing Group, 30th July 2006, pp. 309–311. ISBN: 978-0-313-33438-2. URL: https://books.google.at/books?id=yb9xTj72vNAC&pg=PA310&redir_esc=y#v=onepage&q&f=false (visited on 2016-05-03) (cit. on p. 27).

[46] G. Kresse and J. Furthmüller. 'Efficient iterative schemes for *ab initio* total-energy calculations using a plane-wave basis set'. In: *Physical Review B* 54 (16 Oct. 1996). VASP, pp. 11169–11186. DOI: 10.1103/PhysRevB.54.11169 (cit. on p. 11).

[47] G. Kresse and D. Joubert. 'From ultrasoft pseudopotentials to the projector augmented-wave method'. In: *Physical Review B* 59 (3 Jan. 1999). kresse, pp. 1758–1775. DOI: 10.1103/PhysRevB.59.1758 (cit. on pp. 12, 34).

[48] Aliaksandr V. Krukau et al. 'Influence of the exchange screening parameter on the performance of screened hybrid functionals'. In: *The Journal of Chemical Physics* 125.22, 224106 (2006), p. 224106. DOI: 10.1063/1.2404663 (cit. on p. 8).

[49] Stephan Kümmel and Leeor Kronik. 'Orbital-dependent density functionals: Theory and applications'. In: *Reviews of Modern Physics* 80 (1 Jan. 2008), pp. 3–60. DOI: 10.1103/RevModPhys.80.3 (cit. on p. 12).

[50] M. Letz and L. Parthier. 'Charge centers in CaF_2: *Ab initio* calculation of elementary physical properties'. In: *Physical Review B* 74 (6 Aug. 2006), p. 064116. DOI: 10.1103/PhysRevB.74.064116 (cit. on pp. 19, 20).

[51] V Lupei, A Lupei and I Ursu. 'Pentavalent uranium in CaF_2'. In: *Journal of Physics C: Solid State Physics* 10.22 (1977), p. 4587. DOI: 10.1088/0022-3719/10/22/027 (cit. on p. 26).

[52] W. J. Manthey. 'Crystal Field and Site Symmetry of Trivalent Cerium Ions in CaF_2: The C_{4v} and C_{3v} Centers with Interstitial-Fluoride Charge Compensator'. In: *Physical Review B* 8 (9 Nov. 1973), pp. 4086–4098. DOI: 10.1103/PhysRevB.8.4086 (cit. on p. 24).

[53] A Marek et al. 'The ELPA library: scalable parallel eigenvalue solutions for electronic structure theory and computational science'. In: *Journal of Physics: Condensed Matter* 26.21 (2014), p. 213201. DOI: 10.1088/0953-8984/26/21/213201 (cit. on p. 12).

[54] S. D. McLaughlan. 'Paramagnetic Resonance of Pr_3^+ and U_4^+ Ions in CaF_2'. In: *Physical Review* 150 (1 Oct. 1966), pp. 118–120. DOI: 10.1103/PhysRev.150.118 (cit. on p. 26).

[55] Jens Mende. 'Festkörper-Spin-Quantencomputing nach dem S-Bus-Konzept in CaF_2:Ce'. ger. PhD thesis. Holzgartenstr. 16, 70174 Stuttgart: Universität Stuttgart, 2005. DOI: 10.18419/opus-4745. (Visited on 2016-04-28) (cit. on p. 24).

[56] SB Mirov et al. 'Investigation of Luminescence Properties of Ce:Sc:CaF_2 Crystals'. In: *Materials Science Forum*. Vol. 239. Trans Tech Publ. 1996, pp. 227–230. DOI: 10.4028/www.scientific.net/MSF.239-241.227 (cit. on p. 23).

[57] P. Mohn. 'Theoretical aspects of hyperfine interactions'. In: *Hyperfine Interactions* 128.1 (Nov. 2000), pp. 67–78. ISSN: 1572-9540. DOI: 10.1023/A:1012619212656 (cit. on p. 56).

[58] Koichi Momma and Fujio Izumi. '*V*ESTA3 for three-dimensional visualization of crystal, volumetric and morphology data'. In: *Journal of Applied Crystallography* 44.6 (Dec. 2011), pp. 1272–1276. DOI: 10.1107/S0021889811038970 (cit. on p. 12).

[59] Andrey S. Mysovsky et al. 'Structure and properties of oxygen centers in CaF_2 crystals from *ab initio* embedded cluster calculations'. In: *Physical Review B* 84 (6 Aug. 2011), p. 064133. DOI: 10.1103/PhysRevB.84.064133 (cit. on p. 21).

[60] Dee William Pack, William J. Manthey and Donald S. McClure. 'Ce^{3+}:Na$^+$ pairs in CaF$_2$ and SrF$_2$: Absorption and laser-excitation spectroscopy, and the observation of hole burning'. In: *Physical Review B* 40 (14 Nov. 1989), pp. 9930–9944. DOI: `10.1103/PhysRevB.40.9930` (cit. on pp. 23–25).

[61] Joachim Paier, Martijn Marsman and Georg Kresse. 'Why does the B3LYP hybrid functional fail for metals?' In: *The Journal of Chemical Physics* 127.2, 024103 (2007), p. 024103. DOI: `10.1063/1.2747249` (cit. on p. 9).

[62] J. Paier et al. 'Screened hybrid density functionals applied to solids'. In: *The Journal of Chemical Physics* 124.15, 154709 (2006), p. 154709. DOI: `10.1063/1.2187006` (cit. on pp. 8, 10).

[63] M. Paraschiva et al. 'Distribution of Pb^{2+} Ions in PbF$_2$-Doped CaF$_2$ Crystals'. In: *Acta Physica Polonica A* 117.3 (2010), pp. 466–470. DOI: `10.12693/APhysPolA.117.466` (cit. on p. 22).

[64] E. Peik and Chr. Tamm. 'Nuclear laser spectroscopy of the 3.5 eV transition in Th-229'. In: *EPL (Europhysics Letters)* 61.2 (2003), p. 181. DOI: `10.1209/epl/i2003-00210-x` (cit. on p. 1).

[65] John P. Perdew, Kieron Burke and Matthias Ernzerhof. 'Generalized Gradient Approximation Made Simple'. In: *Physical Review Letters* 77 (18 Oct. 1996). PBE, pp. 3865–3868. DOI: `10.1103/PhysRevLett.77.3865` (cit. on pp. 7, 12).

[66] John P. Perdew, Matthias Ernzerhof and Kieron Burke. 'Rationale for mixing exact exchange with density functional approximations'. In: *The Journal of Chemical Physics* 105.22 (1996), pp. 9982–9985. DOI: `10.1063/1.472933` (cit. on p. 8).

[67] John P. Perdew et al. 'Erratum: Restoring the Density-Gradient Expansion for Exchange in Solids and Surfaces [Phys. Rev. Lett. **100** , 136406 (2008)]'. In: *Phys. Rev. Lett.* 102 (3 Jan. 2009), p. 039902. DOI: `10.1103/PhysRevLett.102.039902` (cit. on p. 9).

[68] John P. Perdew et al. 'Restoring the Density-Gradient Expansion for Exchange in Solids and Surfaces'. In: *Phys. Rev. Lett.* 100 (13 Apr. 2008), p. 136406. DOI: `10.1103/PhysRevLett.100.136406` (cit. on p. 9).

[69] Helena M. Petrilli et al. 'Electric-field-gradient calculations using the projector augmented wave method'. In: *Physical Review B* 57 (23 June 1998), pp. 14690–14697. DOI: `10.1103/PhysRevB.57.14690` (cit. on p. 56).

[70] L. van Pieterson et al. '$4f^n \rightarrow 4f^{n-1}5d$ transitions of the light lanthanides: Experiment and theory'. In: *Physical Review B* 65 (4 Jan. 2002), p. 045113. DOI: `10.1103/PhysRevB.65.045113` (cit. on pp. 25, 54).

[71] L. van Pieterson et al. 'Site-selective laser spectroscopy of $4f^n$–$4f^{n-1}5d$ transitions in $CaF_2:Pr_3^+$ with F^-,D^-,H^-,Li^+, or Na^+ charge compensation'. In: *The Journal of Chemical Physics* 115.20 (2001), pp. 9393–9400. DOI: 10.1063/1.1414319 (cit. on pp. 25, 54).

[72] E. Radzhabov and P. Figura. 'Optical Properties of Oxygen-Vacancy Centers in Fluorite'. In: *physica status solidi (b)* 136.1 (1986), K55–K59. ISSN: 1521-3951. DOI: 10.1002/pssb.2221360156 (cit. on p. 21).

[73] E. Radzhabov and P. Figura. 'Optical Properties of Oxygen-Vacancy Defects in Alkaline-Earth Fluoride Crystals'. In: *physica status solidi (b)* 186.1 (1994), K37–K40. ISSN: 1521-3951. DOI: 10.1002/pssb.2221860136 (cit. on p. 21).

[74] M. Raukas et al. 'Optical spectra and photoconductivity of uranium-doped CaF_2 crystals'. In: *Journal of luminescence* 72 (1997). Luminescence and Optical Spectroscopy of Condensed Matter, pp. 250–252. ISSN: 0022-2313. DOI: 10.1016/S0022-2313(96)00366-3 (cit. on p. 26).

[75] M. Reichling et al. 'Nanosecond UV laser damage and ablation from fluoride crystals polished by different techniques'. In: *Applied Physics A: Materials Science & Processing* 69.7 (1999), pp. 743–747. ISSN: 1432-0630. DOI: 10.1007/s003390051520 (cit. on p. 18).

[76] Wade G. Rellergert et al. 'Constraining the Evolution of the Fundamental Constants with a Solid-State Optical Frequency Reference Based on the ^{229}Th Nucleus'. In: *Physical Review Letters* 104 (20 May 2010), p. 200802. DOI: 10.1103/PhysRevLett.104.200802 (cit. on p. 1).

[77] Wade G Rellergert et al. 'Progress towards fabrication of ^{229}Th-doped high energy band-gap crystals for use as a solid-state optical frequency reference'. In: *IOP Conference Series: Materials Science and Engineering* 15.1 (2010), p. 012005. URL: http://stacks.iop.org/1757-899X/15/i=1/a=012005 (cit. on p. 1).

[78] Stephan Rix. 'Radiation-induced defects in calcium fluoride and their influence on material properties under 193 nm laser irradiation'. eng. PhD thesis. Johannes Gutenberg-Universität, 2011. URL: https://publications.ub.uni-mainz.de/theses/volltexte/2011/2800/pdf/2800.pdf (visited on 2016-04-28) (cit. on pp. 13, 14, 18–21, 25).

[79] Jr. Roland W. Ure. 'Ionic Conductivity of Calcium Fluoride Crystals'. In: *The Journal of Chemical Physics* 26.6 (1957), pp. 1363–1373. DOI: 10.1063/1.1743547 (cit. on p. 20).

[80] G. W. Rubloff. 'Far-Ultraviolet Reflectance Spectra and the Electronic Structure of Ionic Crystals'. In: *Physical Review B* 5 (2 Jan. 1972), pp. 662–684. DOI: `10.1103/PhysRevB.5.662` (cit. on pp. 2, 13).

[81] Laurids Schimka, Judith Harl and Georg Kresse. 'Improved hybrid functional for solids: The HSEsol functional'. In: *The Journal of Chemical Physics* 134.2, 024116 (2011), p. 024116. DOI: `10.1063/1.3524336` (cit. on pp. 9, 10).

[82] Gustavo E. Scuseria and Viktor N. Staroverov. 'Chapter 24 - Progress in the development of exchange-correlation functionals'. In: *Theory and Applications of Computational Chemistry. The First Forty Years*. Ed. by Clifford E. Dykstra et al. Amsterdam: Elsevier, 2005, pp. 669–724. ISBN: 978-0-444-51719-7. DOI: `10.1016/B978-044451719-7/50067-6` (cit. on p. 9).

[83] N. Senguttuvan et al. 'Oriented growth of large size calcium fluoride single crystals for optical lithography'. In: *Journal of Crystal Growth* 280.3–4 (2005), pp. 462–466. ISSN: 0022-0248. DOI: `10.1016/j.jcrysgro.2005.03.085` (cit. on p. 13).

[84] R. D. Shannon. 'Revised effective ionic radii and systematic studies of interatomic distances in halides and chalcogenides'. In: *Acta Crystallographica Section A: Crystal Physics, Diffraction, Theoretical and General Crystallography* 32.5 (Sept. 1976), pp. 751–767. DOI: `10.1107/S0567739476001551` (cit. on p. 22).

[85] H. Shi, R. I. Eglitis and G. Borstel. '*Ab initio* calculations of the CaF_2 electronic structure and F centers'. In: *Physical Review B* 72 (4 July 2005), p. 045109. DOI: `10.1103/PhysRevB.72.045109` (cit. on pp. 8–10, 14, 18, 35).

[86] H Shi, R I Eglitis and G Borstel. 'Ab initio calculations of the hydrogen centres in CaF_2 and BaF_2'. In: *Journal of Physics: Condensed Matter* 19.5 (2007), p. 056007. DOI: `10.1088/0953-8984/19/5/056007` (cit. on pp. 9, 21).

[87] J. Sils. 'Defektenspektroskopie in hochreinem und dotierten CaF_2 für optische Anwendungen im DUV'. PhD thesis. Universität Osnabrück, Feb. 2008. URN: `urn:nbn:de:gbv:700-2009040812`. (Visited on 2016-04-28) (cit. on pp. 18, 21).

[88] Janis Sils, Evgeny Radzhabov and Michael Reichling. 'Characterisation of oxygen defects in calciumdifluoride'. In: *Journal of Physics and Chemistry of Solids* 68.3 (2007), pp. 420–425. ISSN: 0022-3697. DOI: `10.1016/j.jpcs.2006.12.003` (cit. on p. 21).

[89] J. Sils et al. 'Impurities in synthetic fluorite for deep ultraviolet optical applications'. In: *Journal of Applied Physics* 106.6, 063109 (2009), p. 063109. DOI: `10.1063/1.3224879` (cit. on p. 23).

[90] Alejandro Sonzogni, ed. *NuDat (Nuclear Structure and Decay Data)*. National Nuclear Data Center, Brookhaven National Laboratory. 28th Apr. 2016. URL: `http://www.nndc.bnl.gov/nudat2/` (visited on 2016-04-28) (cit. on p. 27).

[91] S. Speziale and T. S. Duffy. 'Single-crystal elastic constants of fluorite (CaF_2) to 9.3 GPa'. In: *Physics and Chemistry of Minerals* 29 (7 2002), pp. 465–472. ISSN: 0342-1791. DOI: `10.1007/s00269-002-0250-x` (cit. on p. 14).

[92] P. J. Stephens et al. 'Ab Initio Calculation of Vibrational Absorption and Circular Dichroism Spectra Using Density Functional Force Fields'. In: *The Journal of Physical Chemistry* 98.45 (1994), pp. 11623–11627. DOI: `10.1021/j100096a001` (cit. on p. 9).

[93] G. G. Stokes. 'On the Change of Refrangibility of Light'. In: *Philosophical Transactions of the Royal Society of London* 142 (1852), pp. 463–562. DOI: `10.1098/rstl.1852.0022` (cit. on p. 13).

[94] Liangbi Su et al. 'Optical absorption properties and valence states of uranium in CaF_2 crystals grown by TGT'. In: *Journal of Crystal Growth* 270.1–2 (2004), pp. 150–155. ISSN: 0022-0248. DOI: `10.1016/j.jcrysgro.2004.06.013` (cit. on p. 26).

[95] R. S. Title et al. 'Optical Spectra and Paramagnetic Resonance of U^{4+} Ions in Alkaline Earth Fluoride Lattices'. In: *Physical Review* 128 (1 Oct. 1962), pp. 62–66. DOI: `10.1103/PhysRev.128.62` (cit. on p. 26).

[96] Toru Tsujibayashi et al. 'Spectral profile of the two-photon absorption coefficients in CaF_2 and BaF_2'. In: *Applied Physics Letters* 80.16 (2002), pp. 2883–2885. DOI: `10.1063/1.1471939` (cit. on pp. 2, 13).

[97] Jean-Philippe Uzan. 'The fundamental constants and their variation: observational and theoretical status'. In: *Rev. Mod. Phys.* 75 (2 Apr. 2003), pp. 403–455. DOI: `10.1103/RevModPhys.75.403` (cit. on p. 1).

[98] Romanenko V.I. et al. 'Direct Two-Photon Excitation of Isomeric Transition in Thorium-229 Nucleus'. In: *Ukrainian Journal of Physics* 57.11 (2012), pp. 1119–1131. ISSN: 2071-0194. arXiv: `1211.5437 [physics.atom-ph]`. (Visited on 2016-05-03) (cit. on p. 1).

[99] B.M Voronin and S.V Volkov. 'Ionic conductivity of fluorite type crystals CaF_2 , SrF_2, BaF_2, and $SrCl_2$ at high temperatures'. In: *Journal of Physics and Chemistry of Solids* 62.7 (2001), pp. 1349–1358. ISSN: 0022-3697. DOI: `10.1016/S0022-3697(01)00036-1` (cit. on p. 13).

[100] Oleg A. Vydrov et al. 'Importance of short-range versus long-range Hartree-Fock exchange for the performance of hybrid density functionals'. In: *The Journal of Chemical Physics* 125.7, 074106 (2006), p. 074106. DOI: `10.1063/1.2244560` (cit. on p. 8).

[101] Roman Wahl, Doris Vogtenhuber and Georg Kresse. '$SrTiO_3$ and $BaTiO_3$ revisited using the projector augmented wave method: Performance of hybrid and semilocal functionals'. In: *Physical Review B* 78.10 (Sept. 2008), p. 104116. DOI: `10.1103/PhysRevB.78.104116` (cit. on p. 12).

[102] Ralph Walter Graystone Wyckoff. *Crystal structures*. 9th ed. Vol. 1. New York, NY: Interscience/John Wiley, 1963 (cit. on pp. 14, 35).

[103] IN Yakovkin and PA Dowben. 'The problem of the band gap in LDA calculations'. In: *Surface Review and Letters* 14.03 (2007), pp. 481–487. DOI: `10.1142/S0218625X07009499` (cit. on p. 7).

[104] Takayuki Yanagida et al. 'Measurement of light yield of Ce^{3+} perturbed emission of CaF_2 scintillator coupled with avalanche photodiode'. In: *Nuclear Science Symposium Conference Record, 2008. NSS '08. IEEE*. Oct. 2008, pp. 1162–1165. DOI: `10.1109/NSSMIC.2008.4774608` (cit. on p. 24).